

## Editorial corner – a personal view

### Nanocelluloses and their use in composite materials

*K. Oksman\**

Luleå University of Technology, Composite Centre Sweden, Division of Materials Science, SE - 97187 Luleå, Sweden

Cellulose nanofibres and crystals have gained a large interest, not only in the academic research society but also in industries, during the last few years. The number of published papers on this topic has increased from some few publications per year in 2005 to more than 500 in 2011. The research topics have been extraction methods of nanocelluloses, their properties, chemical modifications, self-assembling and their use in composites. It is obvious that the world's largest forest companies believe that nanocelluloses will lead to new uses of forest resources and open a new business area. The uses are expected to be new lightweight composite materials to be used in transport, electronic applications but nanocelluloses can also be used in food, cosmetics, medical, packaging and many other applications. The extracted nanofibres are usually around 20–30 nm in diameter and the length is estimated to be in  $\mu\text{m}$  range while the nanocrystals are much smaller, being about 3–5 nm in diameter and 200 nm in length. The properties of the cellulosic nanomaterials from natural resources (wood, bioresidues, annual plants) have shown to be very similar independent of the original source, meaning that the size distribution of nanofibres is an important factor and that it can be tailored for different applications. The main challenge, when producing cellulose-based nanocomposites, is to disperse the nanoreinforcements in the polymer matrix without degradation of the polymer or the reinforcing phase. Therefore the most common way to prepare cellulose nanocomposites has been the impregnation of 'cellulose nanopaper' by a polymer resin or use of solvents to disperse the nanocelluloses in a solved polymer. These methods show that composites with high mechani-

cal properties can be prepared but are restricted to thin sheets or films and also small scale process. To produce the nanocomposites in larger scale and with possibility to make different shapes, melt processing technologies need to be developed and that is a challenge because nanofibres and crystals are strongly hydrophilic and when dried it is very difficult to re-disperse them. We know that different chemical modifications, to make them re-dispersible, are usually affecting their thermal stability and crystallinity negatively and there by decreasing the composites properties.

Now after some years intensive research, we can see several initiatives, which are taken to produce nanocellulose in large scale, and we are also waiting for the first commercial applications based on these materials. My opinion is that that the first applications will not be composites but barrier coatings on board or paper for packaging applications, stronger paper, and transparent films for electronic applications, medical scaffolds and also nanoporous selective membranes. To be able to develop composites based on nanocellulose we have to solve the dispersion problem as well as to develop suitable processing technologies for large scale.



Prof. Dr. Kristiina Oksman  
Member of International Advisory Board

\*Corresponding author, e-mail: [kristiina.oksman@ltu.se](mailto:kristiina.oksman@ltu.se)  
© BME-PT

# Mechanical and optical effects of elastomer interaction in polypropylene modification: Ethylene-propylene rubber, poly-(ethylene-co-octene) and styrene-butadiene elastomers

C. Grein<sup>1,2</sup>, M. Gahleitner<sup>2\*</sup>, K. Bernreitner<sup>2</sup>

<sup>1</sup>SABIC Europe, P.O.Box: 5151, 6130 Sittard, The Netherlands

<sup>2</sup>Borealis Polyolefine GmbH, Innovation Headquarters, St. Peterstraße 25, 4021 Linz, Austria

Received 9 January 2012; accepted in revised form 12 March 2012

**Abstract.** The interaction between binary combinations of three different elastomer classes commonly applied in impact modification of isotactic polypropylene (iPP) was studied. Blends based on a homogeneous ethylene-propylene (EP) random copolymer (EP-RACO) and a heterophasic EP impact copolymer comprising ethylene-propylene rubber (EPR) with different external elastomer types, one homogeneous ethylene-1-octene copolymer (EOC), and two hydrogenated styrene-butadiene-styrene triblock copolymers (SEBS) with different styrene content, were prepared. The phase morphology, mobility as a function of temperature, mechanical and optical properties were studied. Special effects could be achieved for the combination of two different elastomer types. The results clearly demonstrate the possibility to achieve attractive property combinations in ternary systems consisting of a crystalline PP matrix and two different types of elastomer, EPR or EOC on the one hand and SEBS on the other hand. A combination of density matching and compatibilization effects allows reaching good low temperature impact strength together with a transparency close to matrix level when selecting a butadiene-rich SEBS type.

**Keywords:** mechanical properties, polypropylene, elastomer, morphology

## 1. Introduction

Heterophasic polypropylene (PP) copolymers or blends, consisting of a crystalline polypropylene (co)polymer matrix and a largely amorphous elastomeric component, are typically chosen for their high impact strength in numerous applications [1, 2]. When the relation between matrix stiffness and elastomer amount results in a ‘stiff’ final material (i.e. having a modulus above 800 MPa, often going up to more than 1500 MPa) the target applications mostly are in the injection moulding area, ranging from thin-wall packaging for foodstuff like ice-cream or dairy products to components for cars and electrical equipment. When matrix crystallinity is reduced by copolymerization and leads together

with a high elastomer amount to a ‘soft’ material (i.e. having typically a modulus below 700 MPa, often going down to less than 400 MPa) the target applications mostly are in the (cast or blown) film area, ranging from flexible lids and stand-up pouches for food packaging to highly specialized and very soft pillow pouches for the medical and pharmaceutical area [3]. A significant widening of the available property range in recent years has allowed PP to substitute other polymer materials both in the stiff area (like polystyrene or polyamide) and in the flexible area (like polyethylene or plasticised poly(vinyl chloride)).

Designing tailored polymer compositions can be challenging since many polymer properties are

\*Corresponding author, e-mail: [markus.gahleitner@borealisgroup.com](mailto:markus.gahleitner@borealisgroup.com)

directly or indirectly interrelated. It is, for example, difficult to combine low temperature impact strength and transparency. Because of the density difference between crystalline matrix ( $900\text{--}910\text{ kg/m}^3$ ) and rather amorphous elastomer particles ( $840\text{--}880\text{ kg/m}^3$ ), the latter will act as scattering centres for light if they are big enough. For transparent materials the particles should therefore be as small as possible [4] or closely matched in refractive index (i.e. in density when talking about PP and PE mix). The particle size is, however, directly related to compatibility and viscosity ratio, both in extruder blend systems [5–9] and in reactor-made multiphase copolymers [8–13]. Especially for materials with good flowability elastomer components of very low viscosity are required which necessarily only deliver a very limited contribution to the impact strength [10]. Because of that and due to high nonlinearities in the toughness evolution a combination of different mechanical requirements can be challenging with purely reactor-based solutions [8, 9]. One possible solution for combining low temperature impact strength and transparency is the additional application of external elastomer types. High impact strength levels, but normally only limited optical performance can be achieved with ethylene-co-octene or -butene elastomers and elastomers based on polymerisation with single-site catalysts in solution like ENGAGE™ from DOW or EXACT™ from ExxonMobil [14–18] when the densities typically range typically in between  $850$  and  $875\text{ kg/m}^3$ . The comonomer content [15] and the molecular weight [18] of these homogeneous copolymers can be varied in a wide range, allowing applicability in a wide range of stiffness and melt flow rate (MFR), the density difference and ‘sharp’ interface to the iPP matrix (i.e. without co-crystallization across the phase boundary) are clearly causing light scattering and limiting transparency.

Very good optical performance, but only limited low-temperature impact strength is reached with ethylene-propylene block copolymers of the Vista-maxx™ type by ExxonMobil due to the excellent compatibility to PP and its copolymers [19, 20], and a density close to  $900\text{ kg/m}^3$ . The main reason for the comparably poor impact performance is the relatively high glass transition temperature of these polymers at  $\sim 30^\circ\text{C}$ . Only limited experience exists so far for the use of olefin block copolymers pro-

duced with a chain-shuttling catalyst concept [18, 21, 22], but no particularly advantageous optical performance has been reported.

Finally, styrene-based elastomers of the di- or triblock type have found uses in special areas despite their comparatively higher price [23, 24]. Mostly hydrogenated styrene-butadiene triblock systems are used which can be designed in a wide range of compatibility and viscosity by varying the molecular weight and individual block lengths [25]. Otherwise inaccessible combinations of density and glass transition – e.g.  $910\text{ kg/m}^3$  and  $-62^\circ\text{C}$  for a styrene content of 30 wt% – and the good compatibility between the elastomer blocks and iPP allow unique blend properties, especially when targeting soft compositions [26].

In most of the papers cited so far single examples of external elastomer types have been studied in combination with a homogeneous iPP matrix or, in some cases, as compatibilizers between iPP and high density polyethylene (HDPE) [10, 27, 28]. When modifying reactor-based high-impact EP copolymers, the effect of interactions with the internal EPR and PE phases needs to be considered as well. For this purpose, the interaction between binary combinations of three different elastomer classes commonly applied in impact modification of isotactic polypropylene (iPP) was studied.

## 2. Experimental work

Blends based on a homogeneous ethylene-propylene (EP) random copolymer (EP-RACO) and a heterophasic EP impact copolymer comprising ethylene-propylene rubber (EPR) with different external elastomer types, one homogeneous ethylene-1-octene copolymer (EOC), and two hydrogenated styrene-butadiene-styrene triblock copolymers (SEBS) with different styrene contents, were prepared and investigated. The following two commercial iPP copolymer grades from Borealis (Austria) were selected as base and matrix materials:

- (a) the homogeneous random copolymer (PP-R) RJ370MO having an ethylene content of 3.9 wt%, a density of  $900\text{ kg/m}^3$  and a melt flow rate (MFR acc. ISO 1133,  $230^\circ\text{C}/2.16\text{ kg}$ ) of 45g/10 min, and
- (b) the heterophasic impact copolymer (PP-I) Borpact™ BC918CF having an ethylene content of 4.8 wt%, an EPR content determined as xylene

soluble fraction at +25°C of 14 wt.%, a density of 905 kg/m<sup>3</sup> and a MFR of 3,0 g/10 min.

The seemingly high difference in flowability resp. molecular weight between the two base polymers results from the wish to have a comparable matrix viscosity, as the PP-I matrix component (PP homopolymer) has a comparable viscosity to the PP-R [10, 11].

As external elastomers, three different types selected from two of the aforementioned classes were selected:

- (i) a homogeneous elastomeric ethylene-1-octene copolymer (EOC), Engage 8400 from DOW Chemical (USA) having an octene content of 40 wt%, a density of 870 kg/m<sup>3</sup> and an MFR (190°C / 2.16 kg) of 30 g/10 min,
- (ii) a conventional hydrogenated styrene-butadiene-styrene triblock copolymer (SEBS1), Kraton G 1652 from Kraton Inc. (USA) having a high styrene content of 30 wt%, a density of 910 kg/m<sup>3</sup> and an MFR (230°C/2.16 kg) of 5 g/10 min, and
- (iii) another type of SEBS (SEBS2), Kraton G 1657 from Kraton Inc. (USA) having a low styrene content of 13 wt%, a density of 900 kg/m<sup>3</sup> and an MFR (230°C/2.16 kg) of 22 g/10min.

All compositions investigated are summarized in Table 1. In addition to the pure base polymers, compositions with one or two types of elastomer at concentrations of 19–20 and 24–25 wt% (considering the inherent elastomer content of the PP-I base) were investigated. This means that both binary

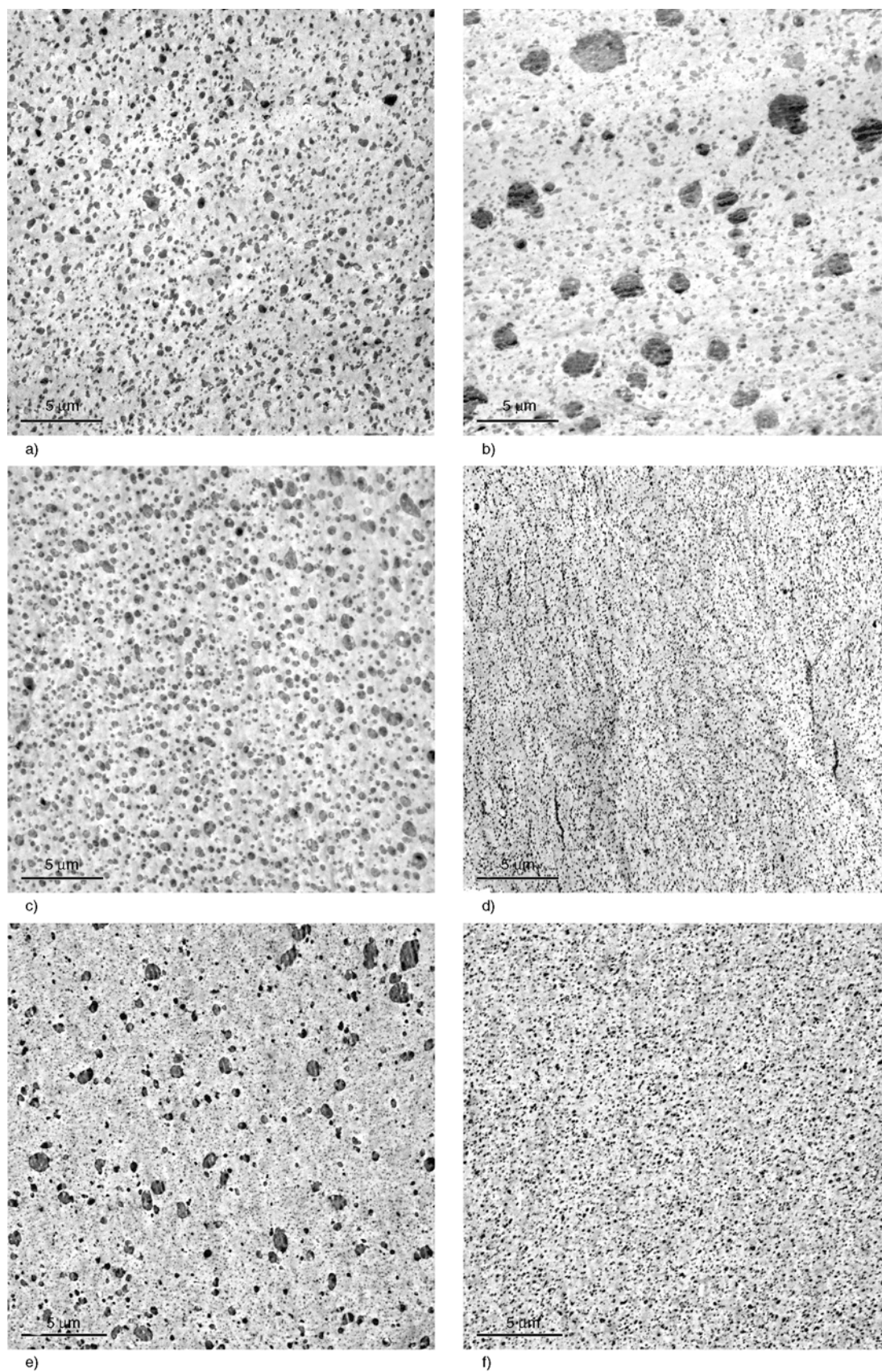
combinations of iPP matrix with each of the elastomers – EOC, SEBS1, SEBS2 and EPR – as well as ternary combinations including two of these were prepared and tested. All compositions were compounded on a co-rotating twin-screw extruder (Thermo-Prism TSE24, Thermo Fisher Scientific Inc., Germany) of 24 mm screw diameter and a length to diameter ratio of 48 with a high-intensity mixing screw and a temperature profile at 180–220°C with a throughput of 10 kg/h and a screw speed of 50 rpm.

For determining the thermo-mechanical performance of the compositions, dynamic-mechanical analysis (DMA) in torsion mode was performed in accordance with ISO 6721 with 50 × 10 × 1 mm<sup>3</sup> compression moulded samples, as a function of temperature at a test frequency of 1 Hz with a heating rate of 2 K·min<sup>-1</sup>. Measurements were carried out under forced oscillation in a torsion mode ( $\varepsilon = 0.04\%$ ) with an ARES rheometer (Rheometrics, USA). Temperature dependence of storage modulus  $G'$  and loss angle tangent  $\tan \delta$  were used for evaluation.

The final mechanical and optical properties of the compositions were investigated according to standard procedures on injection moulded specimens prepared in line with EN ISO 1873-2. Standard mechanical data were determined. The parts were not conditioned prior to testing, which was done at least 96 h after moulding. Charpy notched impact strengths (NIS) were measured on 80 × 10 × 4 mm<sup>3</sup> specimens at +23 and –20°C according to ISO 179/1 eA (test speed of about 3 m·s<sup>-1</sup>), tensile prop-

**Table 1.** Investigated compositions and melt flow rate

Material number	Base resin		Elastomer				MFR 230°C/2.16 kg [g/10 min]
	PP-R [wt%]	PP-I [wt%]	EOC [wt%]	SEBS1 [wt%]	SEBS2 [wt%]	total [wt%]	
M/1	100					0	40
M/2	80		20			20	39
M/3	80			20		20	16
M/4	80				20	20	22
M/5	80		15	5		20	33
M/6	80		15		5	20	34
M/7	75		15	10		25	29
M/8	75		15		10	25	29
M/9	75		25			25	32
M/10		100				14	3.0
M/11		95	5			19	3.1
M/12		95		5		19	3.2
M/13		95			5	19	3.3
M/14		90	10			24	3.1
M/15		90		10		24	3.4
M/16		90			10	24	4.0



**Figure 1.** TEM overview images of 6 of the investigated blends (scale bar size 5  $\mu\text{m}$ ); (a) M/2 PP-R + 20 wt% EOC EG8400, (b) M/5 PP-R + 15 wt% EOC EG8400 + 5 wt% SEBS G 1652 (high styrene content), (c) M/6 PP-R + 15 wt% EOC EG8400 + 5 wt% SEBS G 1657 (low styrene content), (d) M/10 base polymer PP-I, (e) M/12 PP-I + 5 wt% SEBS G 1652 (high styrene content), (f) M/13 PP-1 + 5 wt% SEBS G 1657 (low styrene content)

erties were recorded on universal ISO dog-bone specimens of 3 mm thickness at 23°C according to ISO 572-2 at a test speed of 1 mm·min<sup>-1</sup> for the modulus and 50 mm·min<sup>-1</sup> for yield stress and yield strain. The haze, a commonly applied measure for light scattering inverse to transparency, were determined on 60 × 60 × 1 mm<sup>3</sup> plaques according to ASTM D 1003.

For studying the phase morphology, the samples were also investigated by transmission electron microscopy (TEM) on ultra-microtomed specimens after contrasting with ruthenium tetroxide to allow differentiation between regions of high and low crystallinity [29]. TEM images were recorded on a Tecnai G<sup>2</sup> 12 from FEI (USA), equipped with a CCD camera (Gatan Bioscan, USA) at 100 kV acceleration voltage at the Center for Electron Microscopy Graz, Austria.

### 3. Results and discussion

An overview of all blend morphology types is presented in Figure 1. The first three images present both binary and ternary blend systems based on the homogeneous random copolymer matrix (PP-R) with a clear order of compatibility between the matrix polymer and the three different elastomer types expressed in the resulting particle size. While in all cases an equivalent particle diameter of 3 μm is not exceeded, the smallest particles are clearly achieved with the pure EOC elastomer (1a, composition M/2). The ternary compositions, M/5 and M/6 are quite different insofar as with the styrene-rich

SEBS type a clearly bimodal particle size distribution is achieved while with the butadiene-rich SEBS the morphology is very similar to the binary reference. A generally better dispersion is achieved in the reactor-based PP/EPR systems like the pure PP-I matrix M/10. But even here only the butadiene-rich SEBS allows retaining the largely monomodal particle size distribution (M/13), while a similar bimodality with significantly bigger practically pure SEBS particles results from the addition of the styrene-rich type in M/12.

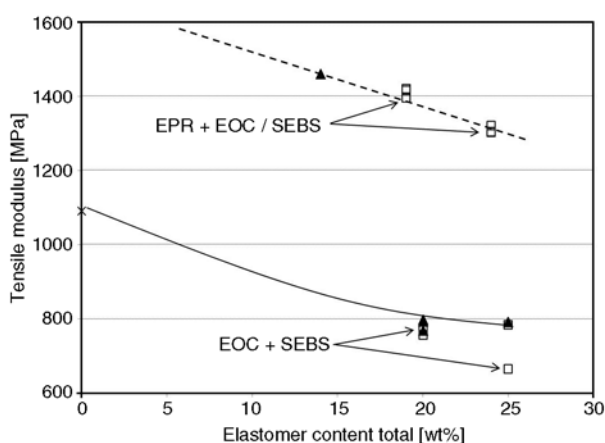
The mechanical and optical performance of all compositions is summarized in Table 2. As to be expected, the composition-induced differentiation is smallest for the tensile modulus (see Figure 2), where only for the PP-R based blends with higher total elastomer content a certain effect of the styrene content of the SEBS types used can be seen. This is well in line with earlier PP/elastomer blend series where a simple ‘mixing rule’ behaviour was found for the (tensile, flexural or dynamic) moduli [4, 6, 9].

Figure 3 demonstrates a significantly stronger differentiation for the impact strength at room temperature, while a look at Table 2 will confirm that quite similar trends are found for the low-temperature impact strength. In the case of the PP-R base, the toughness order for the binary compositions at 20 wt% elastomer is butadiene-rich SEBS (G1657) > EOC (EG 8400) > styrene-rich SEBS (G1652), but the differentiation is even enhanced for the ternary systems. A closer look at the blend morphology (see Figure 4) and the low temperature mobility

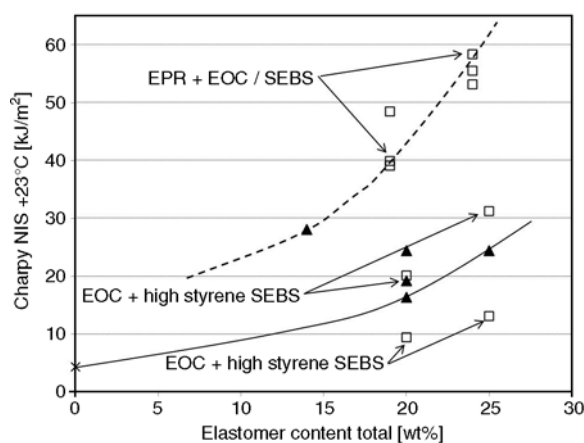
**Table 2.** Mechanical and optical properties (Tensile test – ISO 527-2, Charpy NIS – ISO 179 1eA, Haze – ASTM D 1003)

Material number	Elastomer total [wt%]	Tensile test			Charpy NIS		Haze 1 mm [%]
		Modulus [MPa]	σ <sub>yield</sub> [MPa]	ε <sub>break</sub> [%]	+ 23°C [kJ/m <sup>2</sup> ]	-20°C [kJ/m <sup>2</sup> ]	
M/1	0	1091	28.2	487	4.4	1.0	23.4
M/2	20	798	20.8	571	19.2	1.7	26.2
M/3	20	769	20.4	420	16.4	4.6	50.7
M/4	20	793	20.1	439	24.4	2.7	34.7
M/5	20	756	20.3	614	9.5	2.9	33.4
M/6	20	771	20.0	594	20.2	1.7	27.8
M/7	25	665	18.3	674	13.1	4.0	36.2
M/8	25	783	18.9	562	31.3	2.9	22.6
M/9	25	791	19.2	561	24.4	2.7	28.3
M/10	14	1460	31.3	528	28.1	1.3	32.3
M/11	19	1416	28.3	589	39.1	1.4	38.8
M/12	19	1396	28.5	565	48.5	1.6	32.0
M/13	19	1420	28.0	606	39.9	1.4	30.7
M/14	24	1322	25.8	582	55.5	2.3	26.6
M/15	24	1305	26.3	507	58.4	3.0	28.9
M/16	24	1303	25.2	497	53.2	2.5	27.2

(see Figure 5) of some of the compositions, especially the ternary ones, appears required here. The much stronger relaxation strength ( $\tan\delta$ ) of both SEBS elastomers is obvious in combination with the lower glass transition temperature of the butadiene-rich grade, Kraton G1657. This effect can even still be distinguished in the mixture with the EOC elastomer, as the summary in Table 3 shows. A further look at the DMA traces shows that the temperature dependent mobility of the PP matrix phase is obviously not influenced in any case.



**Figure 2.** Stiffness effect in binary (full triangles; M/2–M/4, M/9 based on PP-R & M/10 pure PP-I) and ternary (open squares; M/5–M/8 based on PP-R & M/11–M/16 based on PP-I) PP / elastomer compositions (M/1 pure PP-R – asterisk); trend-lines (continuous for PP-R-base & dashed for PP-I base) are only indicative



**Figure 3.** Room temperature impact strength effect in binary (full triangles; M/2–M/4, M/9 based on PP-R & M/10 pure PP-I) and ternary (open squares; M/5–M/8 based on PP-R & M/11–M/16 based on PP-I) PP / elastomer compositions (M/1 pure PP-R – asterisk); trend-lines (continuous for PP-R-base & dashed for PP-I base) are only indicative

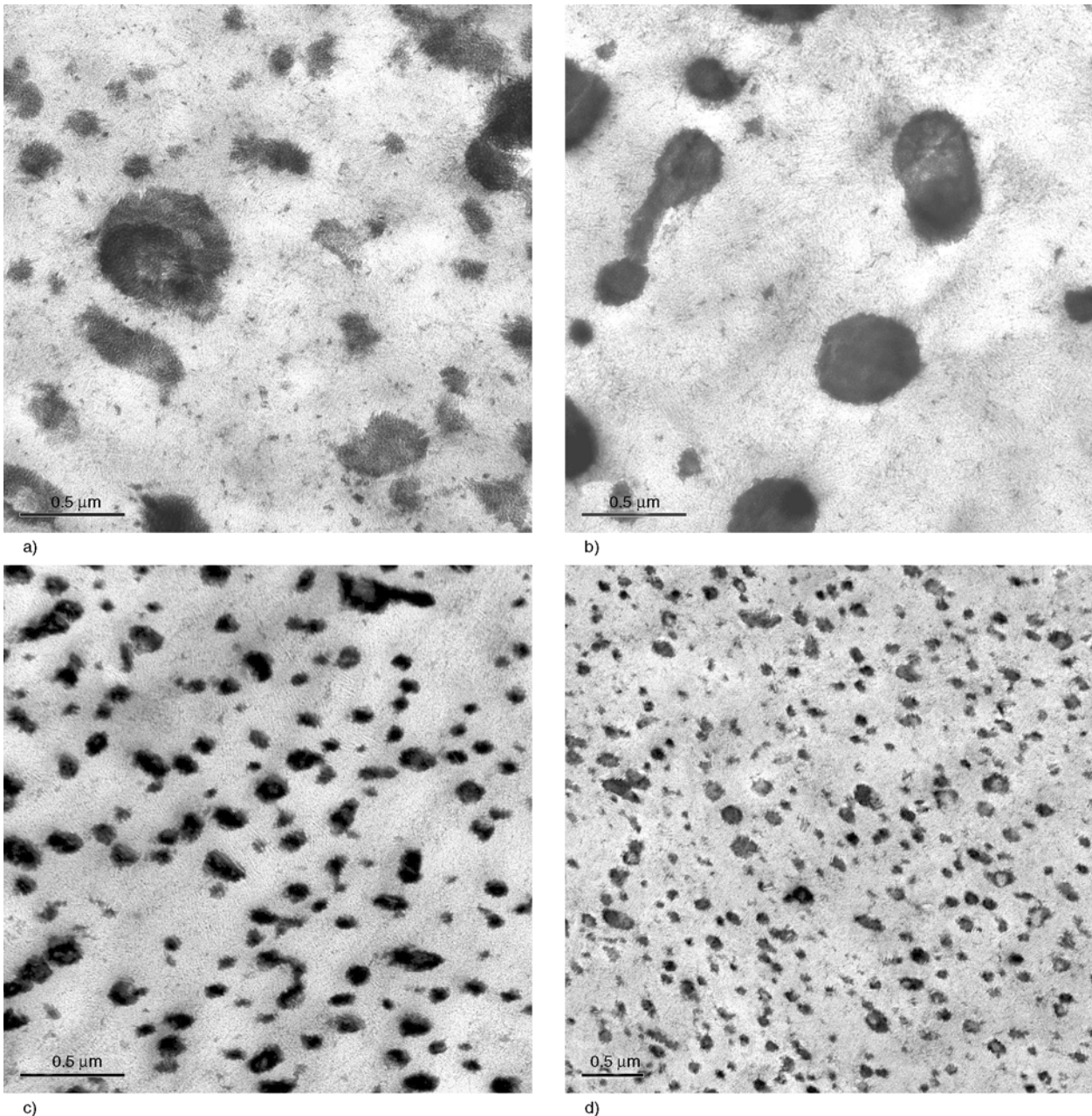
**Table 3.** DMA parameters; Glass transition peak temperatures of the elastomer phase ( $T_{g,e}$ ) and the PP matrix phase ( $T_{g,m}$ ), and storage modulus at +23°C ( $G'_{23}$ )

Material number [–]	Elastomer total [wt%]	DMTA parameters		
		$T_{g,e}$ [°C]	$T_{g,m}$ [°C]	$G'_{23}$ [MPa]
M/1	0	–	–4	573
M/2	20	–58	–4	465
M/3	20	–62	–2.8	443
M/4	20	–64	–2	461
M/5	20	–58	–4	423
M/6	20	–60	–1.9	413
M/10	14	–60	–4	580
M/11	19	–60	–4	515
M/12	19	–63	–4	508
M/13	19	–65	–4	497

In addition to this mobility difference, the morphology of the ternary systems shows a certain compatibilizing effect of the EOC elastomer (which itself clearly forms the smallest elastomer particles). A closer look at the particle structure in Figure 4 reveals the fact that the bigger particles for the ternary system M/4 (the upper part of the bimodal particle size distribution) are the ones rich in (or composed only of) the styrene-rich SEBS which can be identified by the globular styrene domains visible at higher magnifications. For the butadiene-rich SEBS, the compatibilization is more effective and domains of this elastomer can be found only inside an EOC elastomer cover.

This differentiation in terms of impact strength is significantly reduced for the PP-I based blends (see again Figure 2), while the overall toughness level is enhanced especially at room temperature. The high degree of phase compatibility for the selected polymer type results in a relatively high glass transition temperature of part of the reactor-made EPR phase (see Figure 5 and Table 3). This can however be compensated easily by an external elastomer using the compatibilizing effect of this component, as the ternary systems M/11 to M/16 show. Especially the butadiene-rich SEBS type applied for M/13 leaves the particle size of the PP-I base practically unchanged as a comparison between Figures 4c and 4d demonstrates.

While it is certainly an important factor for the impact properties of the respective systems, the optical performance is even more affected by the particle size (see Table 2 and Figure 6). If the positive



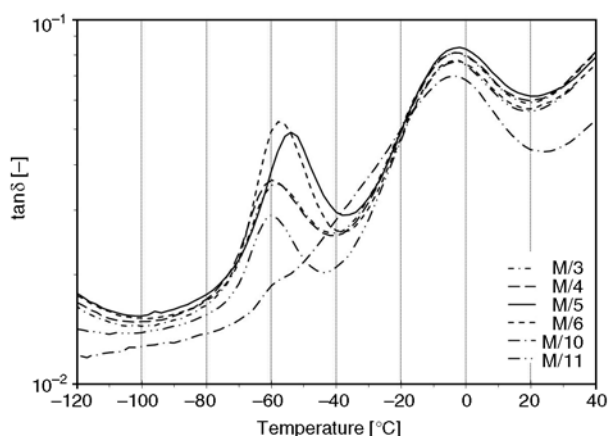
**Figure 4.** TEM detail images of 4 of the investigated blends (scale bar size 0,5 μm); (a) M/4 PP-R + 20 wt% SEBS G 1652 (high styrene content), (b) M/5 PP-R + 15 wt% EOC EG8400 + 5 wt% SEBS G 1652 (high styrene content), (c) M/10 base polymer PP-I, (d) M/13 PP-1 + 5 wt% SEBS G 1657 (low styrene content)

effect of combining the two elastomers in M/6 on impact strength is already interesting, the respective effect on transparency improvement (i.e. haze reduction) is outstanding, as the level of the base polymer is even exceeded here. As the particle size difference is not that big, one may assume that the refractive index of the elastomer mixture plays an important role, as already postulated before [24, 25]. A look at the detail morphology in Figure 4 further shows the change in interfacial structure between the binary

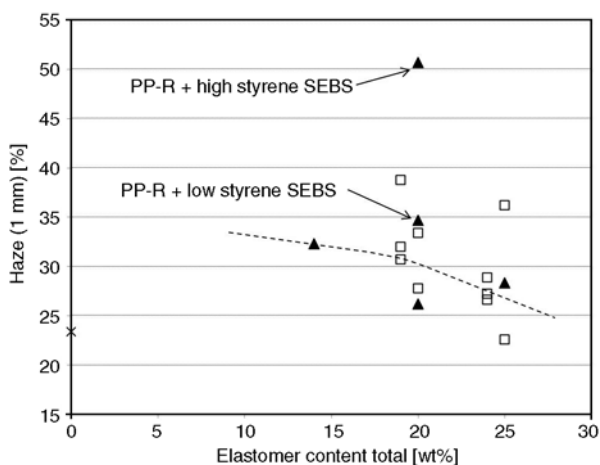
(M/4) and ternary (M/5) which also may contribute to less light scattering.

The fact that this adjustment in terms of density resp. refractive index can even be used for improving the optical performance of a reactor-based PP/EPR system is even more interesting for practical applications. Again, the differentiation is reduced by the compatibilizing effect of the reactor-made EPR phase, but the butadiene-rich SEBS type still delivers a slightly better performance.





**Figure 5.** Loss tangent curves in the elastomer and matrix glass transition region ( $T_{g,e}$  and  $T_{g,m}$ ) for 6 of the investigated blends (M/3 to M/6 based on PP-R; M/10 pure PP-I; M/11 PP-I + EOC)



**Figure 6.** Haze effect in binary (full triangles; M/2–M/4, M/9 based on PP-R & M/10 pure PP-I) and ternary (open squares; M/5–M/8 based on PP-R & M/11–M/16 based on PP-I) PP / elastomer compositions (M/1 pure PP-R – asterisk); trend-lines (continuous for PP-R-base & dashed for PP-I base) are only indicative

#### 4. Conclusions

The investigated model blend series clearly demonstrates the possibility to achieve attractive property combinations in ternary systems consisting of a crystalline PP matrix and two different types of elastomer, EOC and SEBS or (reactor-made) EPR and SEBS. A combination of density matching and compatibilization effects allows combining good low temperature impact strength and a transparency close to matrix level. When selecting a butadiene-rich SEBS type, the lower glass transition temperature of this elastomer possibly plays an additional role.

In any case, modifications based on a multi-phase impact copolymer deliver a better balance of mechanical and optical properties.

These results give a clear guidance for the development of advanced impact copolymer compositions based on multiphase reactor grades. A combination of density matching and compatibilization effects allows combining good low temperature impact strength and a transparency close to matrix level when selecting a butadiene-rich SEBS type.

#### References

- [1] Karger-Kocsis J.: Polypropylene: Structure, blends and composites; Vol. 2 – Copolymers and blends. Chapman and Hall, London (1995).
- [2] Pasquini N.: Polypropylene handbook. Hanser, Munich (2005).
- [3] Schwager H.: PP Reactor blends. in 'Polypropylene '92 World Congress, Zürich, Switzerland' II/4.1–II/4.18 (1992).
- [4] Coppola F., Greco R., Martuscelli E., Kammer H. W., Kummerlowe C.: Mechanical properties and morphology of isotactic polypropylene/ethylene-propylene copolymer blends. *Polymer*, **28**, 47–56 (1987). DOI: [10.1016/0032-3861\(87\)90317-X](https://doi.org/10.1016/0032-3861(87)90317-X)
- [5] Li L., Chen L., Bruin P., Winnik M. A.: Morphology evolution and location of ethylene-propylene copolymer in annealed polyethylene/polypropylene blends. *Journal of Polymer Science Part B: Polymer Physics*, **35**, 979–991 (1997). DOI: [10.1002/\(SICI\)1099-0488\(19970430\)35:6<979::AID-POLB12>3.0.CO;2-C](https://doi.org/10.1002/(SICI)1099-0488(19970430)35:6<979::AID-POLB12>3.0.CO;2-C)
- [6] Gahleitner M., Hauer A., Bernreitner K., Ingolic E.: PP-based model compounds as tools for the development of high-impactethylene-propylene copolymers. *International Polymer Processing*, **17**, 318–324 (2002).
- [7] Kontopoulou M., Wang W., Gopakumar T. G., Cheung C.: Effect of composition and comonomer type on the rheology, morphology and properties of ethylene- $\alpha$ -olefin copolymer/polypropylene blends. *Polymer*, **44**, 7495–7504 (2003). DOI: [10.1016/j.polymer.2003.08.043](https://doi.org/10.1016/j.polymer.2003.08.043)
- [8] Hayashi K., Morioka T., Toki S.: Microdeformation mechanisms in propylene-ethylene block copolymer. *Journal of Applied Polymer Science*, **48**, 411–418 (1993). DOI: [10.1002/app.1993.070480305](https://doi.org/10.1002/app.1993.070480305)
- [9] Grellmann W., Seidler S., Jung K., Kotter I.: Crack-resistance behavior of polypropylene copolymers. *Journal of Applied Polymer Science*, **79**, 2317–2325 (2001). DOI: [10.1002/1097-4628\(20010328\)79:13<2317::AID-APP1039>3.0.CO;2-N](https://doi.org/10.1002/1097-4628(20010328)79:13<2317::AID-APP1039>3.0.CO;2-N)

- [10] Grein C., Bernreitner K., Hauer A., Gahleitner M., Neißl W.: Impact modified isotactic polypropylene with controlled rubber intrinsic viscosities: Some new aspects about morphology and fracture. *Journal of Applied Polymer Science*, **87**, 1702–1712 (2003).  
DOI: [10.1002/app.11696](https://doi.org/10.1002/app.11696)
- [11] Grein C., Gahleitner M., Knogler B., Nestelberger S.: Melt viscosity effects in ethylene–propylene copolymers. *Rheologica Acta*, **46**, 1083–1089 (2007).  
DOI: [10.1007/s00397-007-0200-0](https://doi.org/10.1007/s00397-007-0200-0)
- [12] De La Torre V., Rodríguez Fris J. A., Failla M. D., Quinzani L. M.: Effect of melt annealing on the phase structure and rheological behavior of propylene–ethylene copolymers. *Polymer Engineering and Science*, **47**, 912–921 (2007).  
DOI: [10.1002/pen.20775](https://doi.org/10.1002/pen.20775)
- [13] Zhang C., Shangguan Y., Chen R., Wu Y., Chen F., Zheng Q., Hu G.: Morphology, microstructure and compatibility of impact polypropylene copolymer. *Polymer*, **51**, 4969–4977 (2010).  
DOI: [10.1016/j.polymer.2010.08.021](https://doi.org/10.1016/j.polymer.2010.08.021)
- [14] Yu T. C.: Metalloocene plastomer modification of polypropylenes. *Polymer Engineering and Science*, **41**, 656–671 (2001).  
DOI: [10.1002/pen.10761](https://doi.org/10.1002/pen.10761)
- [15] Lee H-Y., Kim D. H., Son Y.: Effect of octene content in poly(ethylene-co-1-octene) on the properties of poly(propylene)/poly(ethylene-co-1-octene) blends. *Journal of Applied Polymer Science*, **103**, 1133–1139 (2007).  
DOI: [10.1002/app.24644](https://doi.org/10.1002/app.24644)
- [16] Tortorella N., Beatty C. L.: Morphology and crystalline properties of impact-modified polypropylene blends. *Polymer Engineering and Science*, **48**, 1476–1486 (2008).  
DOI: [10.1002/pen.21102](https://doi.org/10.1002/pen.21102)
- [17] Svoboda P., Theravalappil R., Svobodova D., Mokrejs P., Kolomaznik K., Mori K., Ougizawa T., Inoue T.: Elastic properties of polypropylene/ethylene–octene copolymer blends. *Polymer Testing*, **29**, 742–748 (2010).  
DOI: [10.1016/j.polymertesting.2010.05.014](https://doi.org/10.1016/j.polymertesting.2010.05.014)
- [18] Liu G., Zhang X., Liu C., Chen H., Walton K., Wang D.: Morphology and mechanical properties of binary blends of polypropylene with statistical and block ethylene-octene copolymers. *Journal of Applied Polymer Science*, **119**, 3591–3597 (2011).  
DOI: [10.1002/app.33035](https://doi.org/10.1002/app.33035)
- [19] Tsou A. H., Lyon M. K., Chapman B. R., Datta S.: Elastic properties of cast films from propylene elastomers. *Journal of Applied Polymer Science*, **107**, 1362–1372 (2008).  
DOI: [10.1002/app.27184](https://doi.org/10.1002/app.27184)
- [20] Chen X-H., Ma G-Q., Li J-Q., Jiang S-C., Yuan X-B., Sheng J.: Study on morphology evolution and fractal character of the miscible blend between isotactic polypropylene and copolymer of ethylene and propylene. *Polymer*, **50**, 3347–3360 (2009).  
DOI: [10.1016/j.polymer.2009.04.069](https://doi.org/10.1016/j.polymer.2009.04.069)
- [21] Arriola D. J., Carnahan E. M., Hustad P. D., Kuhlman R. L., Wenzel T. T.: Catalytic production of olefin block copolymers via chain shuttling polymerization. *Science*, **312**, 714–719 (2006).  
DOI: [10.1126/science.1125268](https://doi.org/10.1126/science.1125268)
- [22] Jin J., Zhao C., Du J., Han C. C.: The possible scalability of mesophase separation on macrophase separation and crystallization of iPP/OBC blends. *Macromolecules*, **44**, 4326–4334 (2011).  
DOI: [10.1021/ma200194c](https://doi.org/10.1021/ma200194c)
- [23] Setz S., Stricker F., Kressler J., Duschek T., Mühlhaupt R.: Morphology and mechanical properties of blends of isotactic or syndiotactic polypropylene with SEBS block copolymers. *Journal of Applied Polymer Science*, **59**, 1117–1128 (1996).  
DOI: [10.1002/\(SICI\)1097-4628\(19960214\)59:7<1117::AID-APP8>3.0.CO;2-H](https://doi.org/10.1002/(SICI)1097-4628(19960214)59:7<1117::AID-APP8>3.0.CO;2-H)
- [24] Yang H., Hansen D., Sothwick J.: Low temperature impact modifier for clear polypropylene applications. in ‘Proceedings of SPE ANTEC 2006, Charlotte, USA’ 1766–1770 (2006).
- [25] Nobuyuki T., Kazuhisa K., Yukiko N., Masashi S., Motokazu T., Iwakazu H.: Miscibility and properties in the blends of polypropylene with hydrogenated polystyrene-block-polybutadiene-block-polystyrene (SEBS) (in Japanese). *Journal of the Society of Rubber Industry, Japan*, **75**, 530–534 (2002).
- [26] Matsuda Y., Hara M., Mano T., Okamoto K., Ishikawa M.: The effect of the volume fraction of dispersed phase on toughness of injection molded polypropylene blended with SEBS, SEPS, and SEP. *Polymer Engineering and Science*, **95**, 1630–1638 (2005).  
DOI: [10.1002/pen.20298](https://doi.org/10.1002/pen.20298)
- [27] Lin Y., Yakovleva V., Chen H., Hiltner A., Baer E.: Comparison of olefin copolymers as compatibilizers for polypropylene and high-density polyethylene. *Journal of Applied Polymer Science*, **113**, 1945–1952 (2009).  
DOI: [10.1002/app.30190](https://doi.org/10.1002/app.30190)
- [28] Lin Y., Marchand G. R., Hiltner A., Baer E.: Adhesion of olefin block copolymers to polypropylene and high density polyethylene and their effectiveness as compatibilizers in blends. *Polymer*, **52**, 1635–1644 (2011).  
DOI: [10.1016/j.polymer.2011.02.012](https://doi.org/10.1016/j.polymer.2011.02.012)
- [29] Poelt P., Ingolic E., Gahleitner M., Bernreitner K., Geymayer W.: Characterization of modified polypropylene by scanning electron microscopy. *Journal of Applied Polymer Science*, **78**, 1152–1161 (2000).  
DOI: [10.1002/1097-4628\(20001031\)78:5<1152::AID-APP250>3.0.CO;2-7](https://doi.org/10.1002/1097-4628(20001031)78:5<1152::AID-APP250>3.0.CO;2-7)

# Synthesis and characterization of polypyrrole doped with anionic spherical polyelectrolyte brushes

N. Su<sup>1</sup>, H. B. Li<sup>1\*</sup>, S. J. Yuan<sup>2</sup>, S. P. Yi<sup>3</sup>, E. Q. Yin<sup>1</sup>

<sup>1</sup>School of Printing and Packaging, Wuhan University, 430079 Wuhan, China

<sup>2</sup>School of Chemical and Environmental Engineering, Hubei University of Technology, 430068 Wuhan, China

<sup>3</sup>College of Chemistry and Molecular Sciences, Wuhan University, 430072 Wuhan, China

Received 28 December 2011; accepted in revised form 16 March 2012

**Abstract.** The procedures for the synthesis of polypyrrole (PPy) doped with anionic spherical polyelectrolyte brushes (ASPB) (PPy/ASPB nanocomposite) by means of *in situ* chemical oxidative polymerization were presented. Fourier transform infrared spectroscopy (FTIR) and Raman spectroscopic analysis suggested the bonding structure of PPy/ASPB nanocomposite. Scanning electron microscopy (SEM) was used to confirm the morphologies of samples. The crystallographic structure, chemical nature and thermal stability of conducting polymers were analyzed by X-ray diffraction (XRD), X-ray photoelectron spectroscopy (XPS) and Thermo-gravimetric analysis (TGA) respectively. Investigation of the electrical conductivity at room temperature showed that the electrical conductivity of PPy/ASPB nanocomposite was 20 S/cm, which was higher than that of PPy (3.6 S/cm).

**Keywords:** nanocomposites, conducting polymers, anionic spherical polyelectrolyte brushes, doping, electrical conductivity

## 1. Introduction

Since the first paper of Shirakawa *et al.* [1] in 1977, conducting polymers have attracted considerable interest because of their excellent physical and chemical properties originating from their unique  $\pi$ -conjugated system [2]. Polypyrrole (PPy) is one of the most extensively studied materials due to its easy synthesis and good environmental stability [3, 4]. However, pristine PPy is insoluble and infusible because of the rigidity of its molecular chains of  $\pi$ -conjugated structure. This poor conductivity and processibility not only impede further investigation of its structure, but also limit its application in technology. So efforts to overcome these drawbacks have led to numerous studies on the synthesis of PPy by both electrochemical and chemical routes. It is well-known that using various dopants has contributed to the development of soluble PPy [5]. Cur-

rently, aromatic acid derivatives and organic sulfonates are widely used, such as dodecylbenzene sulfonic acid (DBSA), p-toluenesulfonic acid (TsOH) [6], etc. Lee *et al.* [7] developed DBSA with surface-active properties as anionic additive to realize pyrrole (Py) solvation. Further studies pointed out that adding other large dopants could reduce the interchain links, resulting in the increase of the conductivity and solubility [8–11]. In view of this, anionic spherical polyelectrolyte brushes (ASPB), consisting of anion polyelectrolyte chains affixing to the surface of spheres, may be novel conducting polymer dopant by introducing the brush polymer with certain functional groups.

The investigations on the structure and properties of PPy have been performed by many techniques. X-ray photoelectron spectroscopy (XPS) proved to be particularly useful in the surface characterization of

\*Corresponding author, e-mail: [lhb@whu.edu.cn](mailto:lhb@whu.edu.cn)

© BME-PT

PPy [12–14] because it has a typical sampling depth of 2–10 nm. Fourier transform infrared spectroscopy (FTIR) is a convenient technique to monitor changes in the structure of conducting polymer chains [15, 16]. Both experimental methods [17] and theoretical model [18] have been developed to describe the dependence of conductivity on conjugation length for PPy from FTIR measurements. In addition, Raman spectra [6], X-ray diffraction (XRD) [19], and Thermo-gravimetric analysis (TGA) [20] are also used to study the structure and properties of PPy.

In this paper, we presented a facile method for the synthesis of PPy doped with ASPB (PPy/ASPB nanocomposite) by *in situ* chemical oxidative polymerization [21, 22]. For comparison, PPy was synthesized first. The morphology of the resulting PPy/ASPB nanocomposite was characterized by scanning electron microscopy (SEM). Information about its structure was obtained from FTIR, Raman spectra, XRD techniques, and its surface chemical composition by XPS measurements. The room temperature electrical conductivities and thermal stability of PPy and PPy/ASPB nanocomposite were investigated by a four-point probe apparatus and TGA respectively.

## 2. Experimental

### 2.1. Materials

Pyrrole (Sinopharm of Chemical Reagents Co., Ltd, Shanghai, China) was distilled under reduced pressure before use. Iron (III) chloride hexahydrate ( $\text{FeCl}_3 \cdot 6\text{H}_2\text{O}$ ) and ethanol were purchased from Sinopharm of Chemical Reagents Co., Ltd, Shanghai, China. They were analytical reagents and were used without further purification. The ASPB ( $D_z \approx 100$  nm,  $M_w = 1800$  g/mol,  $M_w/M_n = 1.6$ ) consisting of modified  $\text{SiO}_2$  cores and poly(Sodium-p-Styrenesulfonate) (PSS) brushes were prepared by surface-initiated polymerization.

### 2.2. Synthesis of PPy/ASPB nanocomposite

The synthesis of PPy/ASPB nanocomposite mainly involved: 0.22 g of ASPB was firstly added into 45 mL mixture of water and ethanol (v/v, 2/1) with ultrasonic dispersion for 20 min followed by addition of 1.34 g of distilled Py (0.2 mol). After the mixture was cooled to 5°C and degassed under  $\text{N}_2$

flow for 15 min, 2.7 g (0.1 mol) of  $\text{FeCl}_3 \cdot 6\text{H}_2\text{O}$  in 15 mL water aqueous solution was added, and the reaction was allowed to continue for 6 h. The resulting products were then collected via filtration, and were subjected to three sequential washings with ethanol and distilled water before finally being dried in vacuum at 60°C for 12 h.

## 2.3. Characterization methods

### 2.3.1. Morphological and structural analysis

Morphological studies were carried out using a Quanta 200 (FEI Company, Netherlands) scanning electron microscope (SEM) operated at 30 kV. FTIR spectra for PPy and PPy/ASPB nanocomposite were obtained using a Nicolet AVATAR 360FT spectrometer (Thermo Nicolet Corporation, USA). Raman spectra were obtained with a RW-1000 system (Renishaw Company, London, United Kingdom) using a  $\text{Ar}^+$  laser operating at 514.5 nm with a CCD detector. X-Ray diffraction (XRD) measurements were carried out on a Shimadzu 'XRD-6000' instrument (Kyoto, Japan) operating at a voltage of 40 kV and a current of 40 mA with  $\text{CuK}_\alpha$  radiation ( $\lambda = 1.54060$  Å). The samples were measured in a continuous scan mode at 10–60° ( $2\theta$ ) with a scanning rate of 5°/min. XPS spectra were recorded using a VGESCALAB MK II system (United Kingdom) operated in the constant analyzer energy mode.

### 2.3.2. Electrical conductivity and thermal analysis

TGA was performed on a SETSYS-1750 instrument at a heating rate of 10°C/min in  $\text{N}_2$  atmosphere. The electrical conductivities of the samples were measured in a four-point probe (RTS-4, China) apparatus at room temperature. After the samples were pressed into the circular tablet with  $D = 13$  mm at 20 MPa, the thickness  $W$  of each tablet was measured. Then  $F(W/S)$  and  $F(D/S)$  ( $S = 1$ ) were looked up from a table to calculate the source current  $I$  according to formula (1).  $F(W/S)$  denoted the width correction coefficient, and  $F(D/S)$  the diameter correction coefficient. Since conductivity ( $\sigma$ ; S/cm) =  $1/\rho$ , the electrical conductivities of resulting products could be calculated by Equation (1):

$$I = F(W/S) \cdot F(D/S) \cdot W \cdot 0.1 \quad (1)$$

### 3. Results and discussion

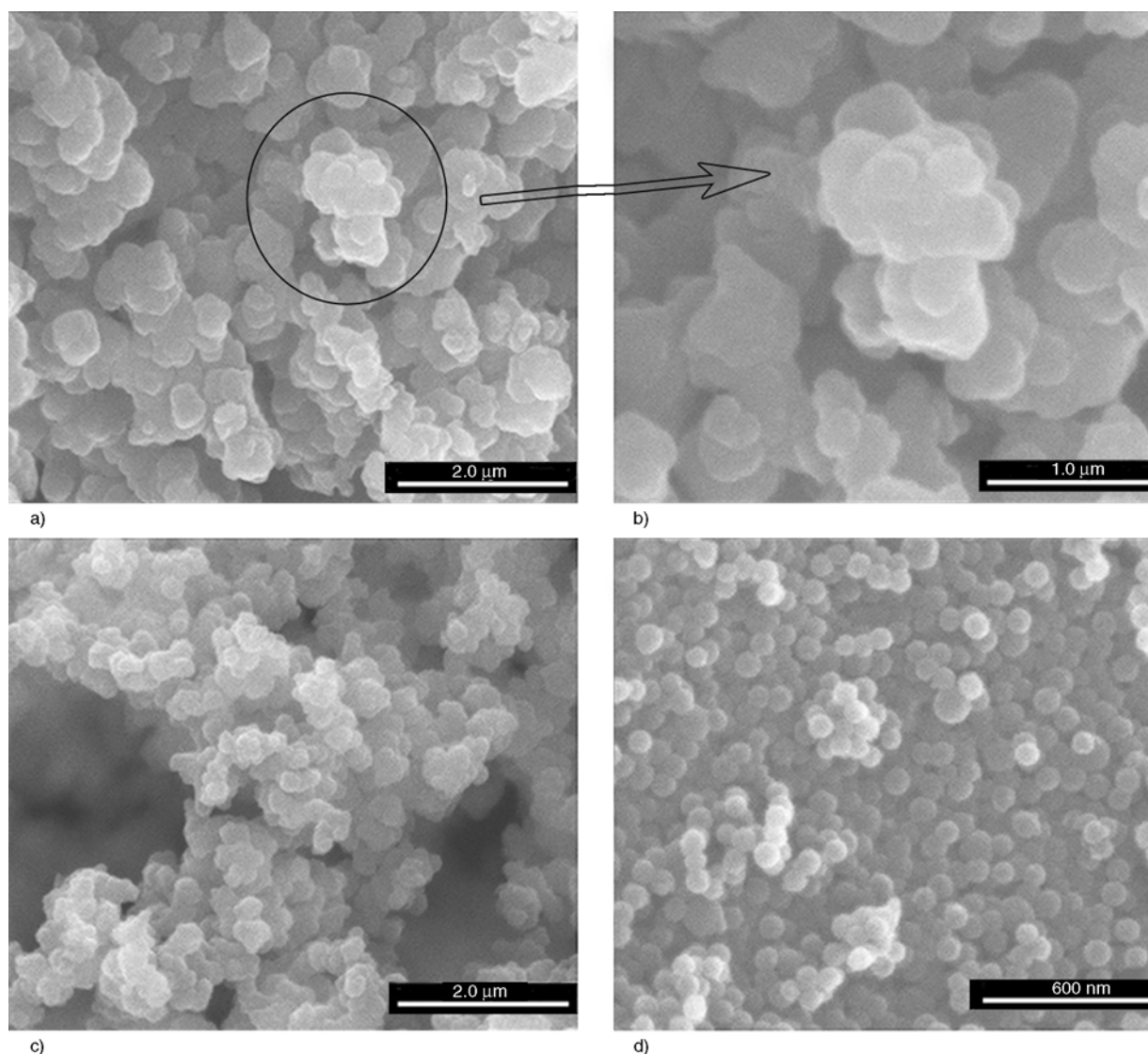
#### 3.1. Morphologies

Figure 1 displays the morphologies of samples, and the schematic representations of formation mechanisms are shown in Figure 2. As shown by the SEM images, PPy displays a typically cauliflower-like or tumor-like structure (Figure 1a, b). The performance of three-dimensional (3D) polymer growth can be considered as quasi network systems through the 2, 3 coupling modes as shown in Figure 2a, supported by the 3D VRH (Variable range hopping) for  $\sigma_{dc}(T)$  [23]. The interchain links or side chains through the 2, 3 coupling modes can lead to the poor solubility of PPy in organic solvents [24]. The addition of ASPB with uniform spherical structure (Figure 1d) provides the space factors for Py orderly growth (Figure 2b), resulting in special morphology of PPy. As shown in Figure 1c, PPy/ASPB nanocom-

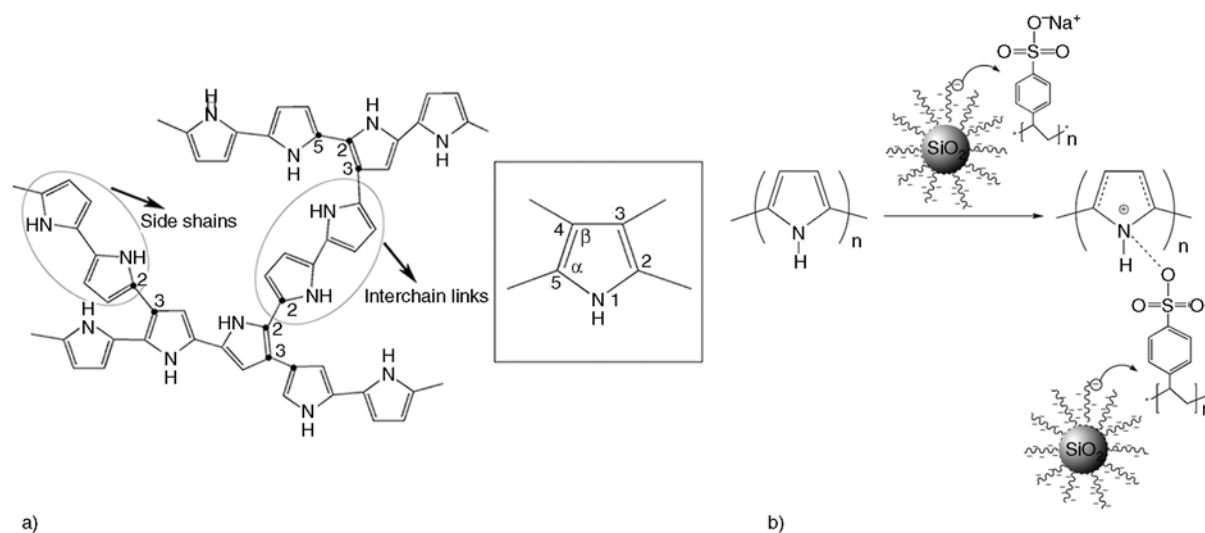
posite shows sphere-like structure and the particle size is much less than that of PPy (Figure 1a). Therefore, the SEM results elucidate that the reactions are remarkably effective for the PPy functionalization.

#### 3.2. FTIR and Raman spectra studies

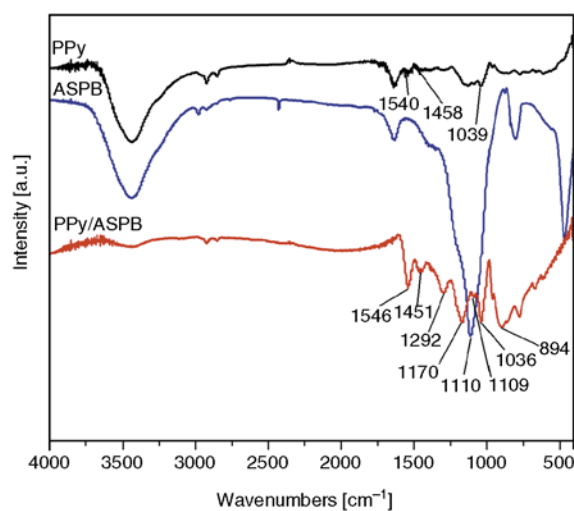
FTIR spectra of samples are represented in Figure 3. The FTIR spectrum of PPy shows the characteristic bands attributable to the C–H in-plane deformation vibration at  $1039\text{ cm}^{-1}$ , C–C asymmetric stretching vibration at  $1458\text{ cm}^{-1}$ , ring-stretching mode of Py ring at  $1540\text{ cm}^{-1}$  [25]. These characteristic peaks from PPy are clearly shown in the FTIR spectrum of PPy/ASPB nanocomposite ( $1036$ ,  $1451$  and  $1546\text{ cm}^{-1}$ ). In addition, PPy/ASPB nanocomposite shows some new bands: the broad band at  $1292\text{ cm}^{-1}$  is attributed to C–H and C–N in-plane deformation



**Figure 1.** SEM images of PPy (a, b), PPy/ASPB nanocomposite (c) and ASPB (d)



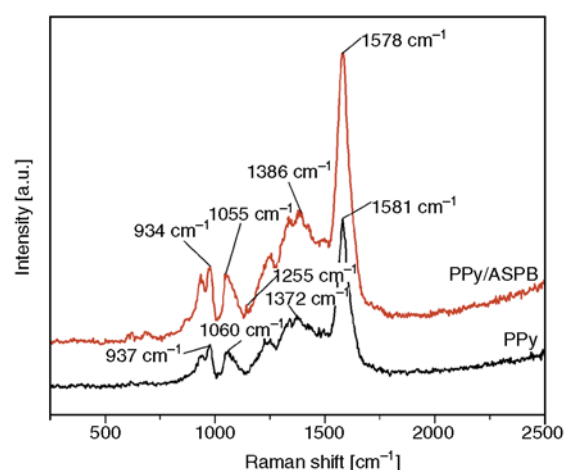
**Figure 2.** Schematic representations of formation mechanisms of PPy (a) and PPy/ASPB nanocomposite (b)



**Figure 3.** FTIR spectra of PPy, ASPB, and PPy/ASPB nanocomposite

vibrations; the strong bands at 1170 and 894  $\text{cm}^{-1}$  are characteristic of doped PPy chains [11]. The peak at 1109  $\text{cm}^{-1}$  may be attributed to Si–O–Si stretching vibrations, which appears at 1110  $\text{cm}^{-1}$  in the spectrum of ASPB, suggesting that ASPB have already been doped in PPy system. In addition, the ratio of the integrated absorption areas of the 1451 and 1546  $\text{cm}^{-1}$  ( $A_{1451}/A_{1546}$ ) bands for the PPy/ASPB nanocomposite is 0.38, which is higher than that of PPy ( $A_{1458}/A_{1540} = 0.27$ ). This suggests the conjugation length increases [17].

Figure 4 shows the Raman spectra of PPy and PPy/ASPB nanocomposite. The prominent bands that emerged in the spectrum of PPy can also be observed in the spectrum of PPy/ASPB nanocomposite. The appearance of peak at 1055  $\text{cm}^{-1}$  (1060  $\text{cm}^{-1}$  for

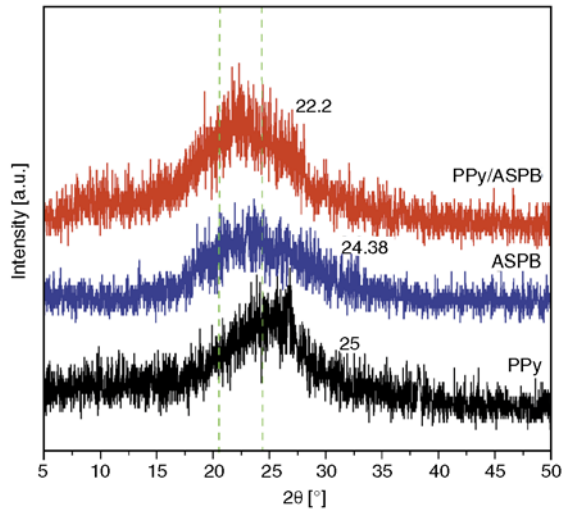


**Figure 4.** Raman spectra of PPy and PPy/ASPB nanocomposite

PPy) has been associated with the quinonoid polaron structure and those at 934  $\text{cm}^{-1}$  (937  $\text{cm}^{-1}$  for PPy) and 1255  $\text{cm}^{-1}$  (no presence in PPy spectrum) have been associated with the quinonoid bipolaron structure, revealing the presence of doped PPy structures [6, 26]. The peak at 1578  $\text{cm}^{-1}$  (1581  $\text{cm}^{-1}$  for PPy) attributable to C=C stretching is considered to be an overlap of two oxidized structures. Therefore, compared with the PPy, PPy/ASPB nanocomposite has an increased portion of bipolarons (1255  $\text{cm}^{-1}$ ) relative to polarons in the Raman spectrum, leading to the high conductivity [27].

### 3.3. Crystallographic structure

The crystallographic structures of samples are characterized using XRD measurements. As shown in Figure 5, PPy only exhibits a broad characteristic



**Figure 5.** XRD patterns of PPy, ASPB and PPy/ASPB nanocomposite

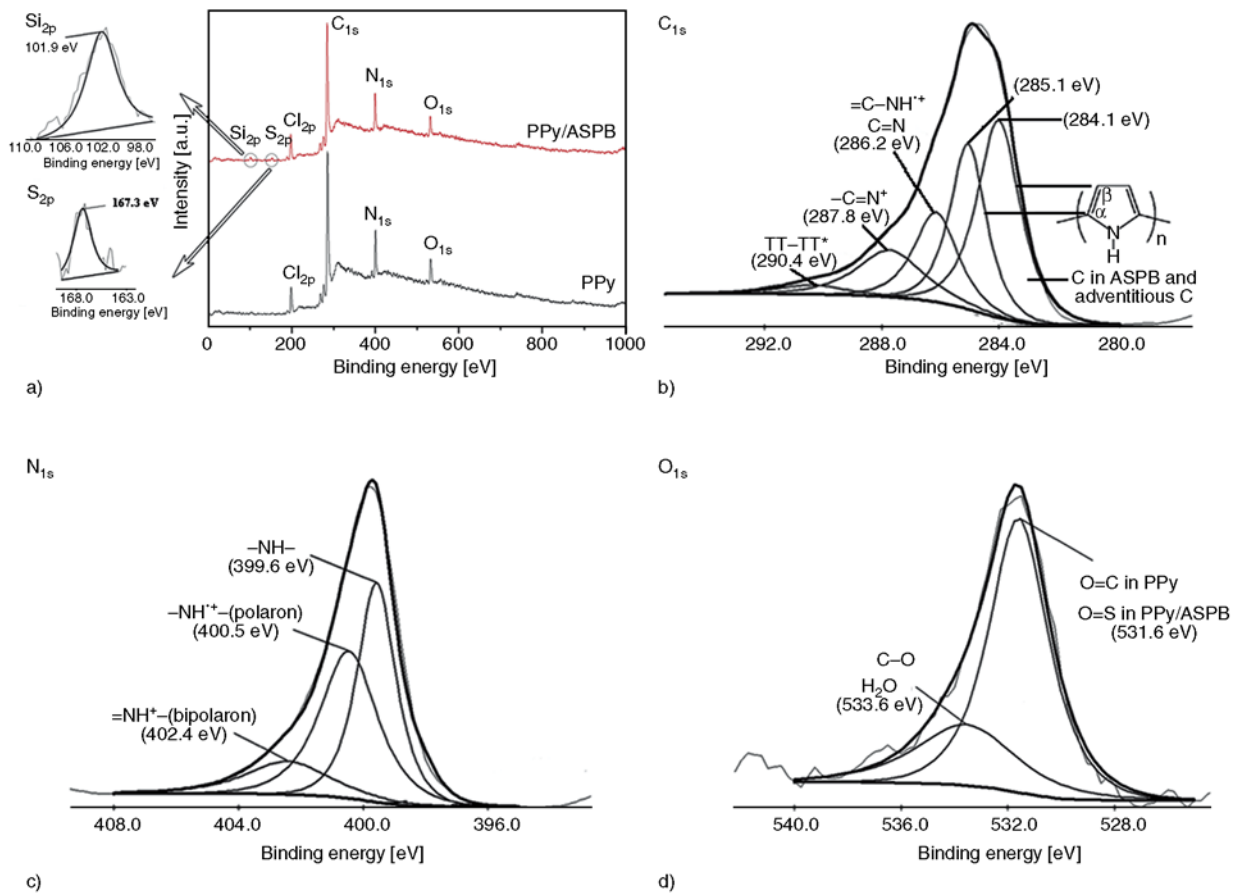
peak at  $2\theta = 25^\circ$ , implying an amorphous structure [28]. For the XRD pattern of ASPB, the characteristic peak at  $2\theta = 24.38^\circ$  appears, corresponding to  $\text{SiO}_2$  reflection peak. For the PPy/ASPB nanocomposite, the broad characteristic peak has shifted to  $22.2^\circ$ . The changes may be due to the doping of

ASPB ( $\text{SiO}_2$  cores) into conducting polymer matrix. In addition, full width at half maximum (FWHM) of PPy/ASPB nanocomposite ( $10.1^\circ$ ) is higher than that of PPy ( $7.6^\circ$ ), which confirms that the crystallinity of PPy/ASPB nanocomposite is decreased, which helps to the increase of solubility.

### 3.4. XPS study

Wide region spectroscopy of PPy and PPy/ASPB nanocomposite are shown in Figure 6a. The narrow range spectra of  $\text{C}_{1s}$ ,  $\text{O}_{1s}$  and  $\text{N}_{1s}$  of PPy/ASPB nanocomposite are also depicted (Figure 6b–d). Compared with the wide region spectroscopy of PPy, the peaks at 101.9 and 167.3 eV for PPy/ASPB nanocomposite spectrum have been observed, suggesting the existence of Silicon and Sulfur signals respectively (from ASPB).

For the chemically synthesized PPy/ASPB nanocomposite, the  $\text{C}_{1s}$  main peak is decomposed into five lines (Figure 6b). The lowest binding energy centered peak (main C peak) at 284.1 eV corresponds to the  $\beta$ -carbons of Py ring and covalent bonded carbon in the ASPB dopant, while the binding energy cen-



**Figure 6.** XPS spectra of (a) wide region spectroscopy, (b)  $\text{C}_{1s}$ , (c)  $\text{N}_{1s}$ , (d)  $\text{O}_{1s}$  of PPy/ASPB nanocomposite

tered peak at 285.1 eV corresponds to  $\alpha$ - carbons. Three other peaks are identified by the deconvolution of the signal at 286.2, 287.8 and 290.4 eV, respectively belonging to the defects in doped PPy. According to the literature by Ruangchuay *et al.* [29], the peak at 286.2 eV is contributed by the imine-like (C=N), polaron (=C–NH<sup>+</sup>), hydroxylated defects (C–OH) and C–S from the dopant. The peak positioned at 287.8 eV is associated to the bipolarons (–C=N<sup>+</sup>) and carbonylic defects (C=O). The highest binding energy peak at 290.4 eV can be assigned to  $\pi$ - $\pi^*$  satellite commonly found in aromatic PPy, 6.3 eV higher than that of the main C peak.

As shown in Figure 6c, the deconvolution of N<sub>1s</sub> signals in the XPS spectrum gives three Gaussian components. The main N peak at 399.6 eV is attributed to the neutral N in the Py ring (–NH–). The imine-like nitrogen (=N–) is disappeared while two new peaks at high binding energy are present [30]. The high binding energy peak can be attributed to oxidized/protonated N. Comparing to the position of the main peak, the 0.9 eV higher binding energy (400.5 eV) peak is indicative of –NH<sup>+</sup>– in the polaron charge carrier species, while the 2.8 eV higher binding energy (402.4 eV) peak can be assigned to =NH<sup>+</sup>–, a bipolaron charge carrier species [31]. Upon consideration of the literature, the nitrogen signal of dedoped PPy only has three peaks at about 397.8, 399.7, and 400.5 eV. The present set of peaks is shifted to higher binding energy compared to that of PPy.

The oxygen signal (O<sub>1s</sub>) in the XPS spectrum is shown in Figure 6d. Two peaks at 531.6 and 533.6 eV are found from the deconvolution of the signal. The peak at 531.6 eV can be attributed to the O=S of the dopant present in the PPy/ASPB nanocomposite [32], while the peak located at 533.6 eV may be related to the oxygen contribution of bound water and polymer-oxidized moieties.

XPS studies indicate that doping of ASPB into PPy matrix is achieved, as expected, which is consistent with both FTIR studies.

### 3.5. Measurements of electrical conductivity

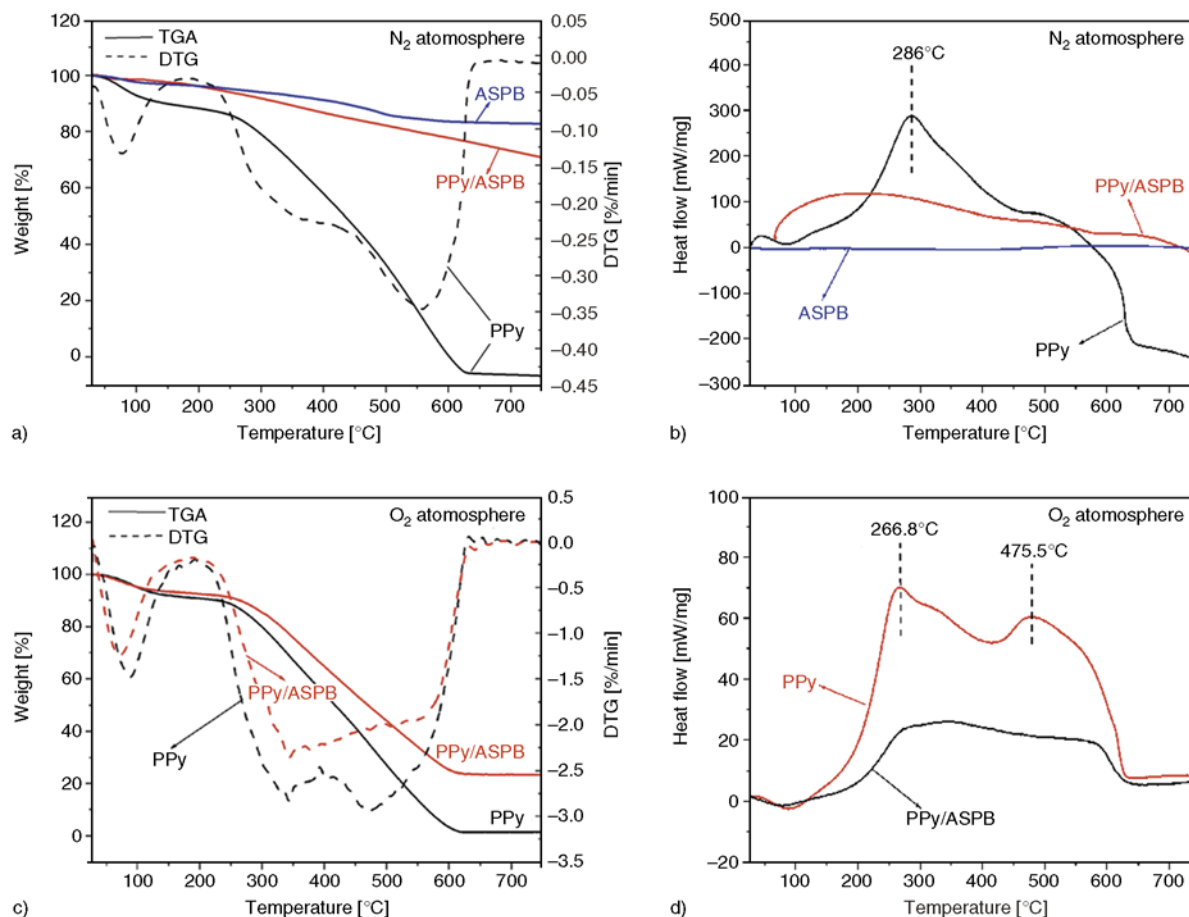
The electrical conductivities of PPy and PPy/ASPB nanocomposite are determined using a RTS-4 four point probe resistivity measurement system. Results

indicate that the room temperature electrical conductivity of PPy is 3.6 S/cm, however, PPy/ASPB nanocomposite shows a high value of conductivity (20 S/cm). Also, it is higher than those reported by literatures, including PPy-grafted multiwalled carbon nanotube (MWCNT) [25], polypropylene (PP)/montmorillonite (MMT)/PPy nanocomposites [33], PPy/SiO<sub>2</sub> nanocomposite [34] and PPy/PSS core-shell nanoparticles [35]. Increase in magnitude of conductivity is consistent with the FTIR and Raman spectra results.

### 3.6. Thermal gravimetric analysis

Figure 7 displays the thermal gravimetric analysis of PPy, ASPB and PPy/ASPB nanocomposite under N<sub>2</sub> and O<sub>2</sub> atmospheres at 60% RH. As observed from the Figure 7a, it demonstrates that the thermal stability of ASPB is much higher than that of PPy in the temperature range of 35–750°C. As PPy is hygroscopic, nearly 7.9 wt% weight loss has occurred at 100°C, due to the evaporation of residual water while only 2 wt% weight loss for PPy/ASPB nanocomposite. As the temperature increases, the main mass loss of PPy and PPy/ASPB nanocomposite starts at about 250°C corresponding to PPy degradation [36]. In case of PPy, the weight reduces largely with only one endothermic peak at 286°C observed in Figure 7b. However, a considerable enhancement in thermal stability has been seen for PPy/ASPB nanocomposite. Finally at 600°C, weight loss for PPy is almost 100%, much more than that for PPy/ASPB nanocomposite (25%). The increase of PPy/ASPB nanocomposite residual content can also be displayed in Figure 7c. Compared with the DSC curve of PPy at N<sub>2</sub> atmosphere (Figure 7b), the curve of PPy under O<sub>2</sub> atmosphere (Figure 7d) shows the end of a sharp exothermic peak at 475.5°C because of additional oxygen involving in the reaction [37]. For the DSC curve of PPy/ASPB nanocomposite, the exothermic peaks are not obvious and move to the high temperature. All the results show that introducing ASPB into the PPy system can enhance the thermal stability of PPy. The improvement in the thermal stability can also be attributed to the increase in orderliness of PPy chains, supported by analysis of XRD, SEM and conductivity measurements.





**Figure 7.** Thermal gravimetric analysis of PPy, ASPB and PPy/ASPB nanocomposite under N<sub>2</sub> atmosphere (a, b) and under O<sub>2</sub> atmosphere (c, d)

#### 4. Conclusions

In summary, novel PPy/ASPB nanocomposite by means of *in situ* chemical oxidation polymerization method has been described. Different characterization and analytical methods confirm that ASPB is an excellent dopant for PPy. Compared with PPy, PPy/ASPB nanocomposite possesses the appearance of sphere-like morphology, enhanced thermal stability and higher room temperature electrical conductivity. Therefore, for the doped PPy system, more work is certainly necessary to validate the above treatment for other intrinsically conducting polymers.

#### Acknowledgements

This research was supported by Scientific Research Program of Wuhan University (217274815) and National Natural Science Foundational of China (31170558).

#### References

- [1] Shirakawa H., Louis E. J., MacDiarmid A. G., Chiang C. K., Heeger A. J.: Synthesis of electrically conducting organic polymers: Halogen derivatives of polyacetylene, (CH)<sub>x</sub>. *Journal of the Chemical Society, Chemical Communications*, **16**, 578–580 (1977). DOI: [10.1039/C39770000578](https://doi.org/10.1039/C39770000578)
- [2] Jang J., Nam Y., Yoon H.: Fabrication of polypyrrole-poly(N-vinylcarbazole) core-shell nanoparticles with excellent electrical and optical properties. *Advanced Materials*, **17**, 1382–1386 (2005). DOI: [10.1002/adma.200401841](https://doi.org/10.1002/adma.200401841)
- [3] Wu T-M., Lin S-H.: Synthesis, characterization, and electrical properties of polypyrrole/multiwalled carbon nanotube composites. *Journal of Polymer Science Part A: Polymer Chemistry*, **44**, 6449–6457 (2006). DOI: [10.1002/pola.21724](https://doi.org/10.1002/pola.21724)
- [4] Carrasco P. M., Grande H. J., Cortazar M., Alberdi J. M., Areizaga J., Pomposo J. A.: Structure-conductivity relationships in chemical polypyrroles of low, medium and high conductivity. *Synthetic Metals*, **156**, 420–425 (2006). DOI: [10.1016/j.synthmet.2006.01.005](https://doi.org/10.1016/j.synthmet.2006.01.005)

- [5] DeArmitt C., Armes S. P.: Colloidal dispersions of surfactant-stabilized polypyrrole particles. *Langmuir*, **9**, 652–654 (1993).  
DOI: [10.1021/la00027a007](https://doi.org/10.1021/la00027a007)
- [6] Yuan X., Zeng X., Zhang H.-J., Ma Z.-F., Wang C.-Y.: Improved performance of proton exchange membrane fuel cells with *p*-toluenesulfonic acid-doped Co-PPy/C as cathode electrocatalyst. *Journal of the American Chemical Society*, **132**, 1754–1755 (2010).  
DOI: [10.1021/ja909537g](https://doi.org/10.1021/ja909537g)
- [7] Lee J. Y., Kim D. Y., Kim C. Y.: Synthesis of soluble polypyrrole of the doped state in organic solvents. *Synthetic Metals*, **74**, 103–106 (1995).  
DOI: [10.1016/0379-6779\(95\)03359-9](https://doi.org/10.1016/0379-6779(95)03359-9)
- [8] Lee J. Y., Song K. T., Kim S. Y., Kim Y. C., Kim D. Y., Kim C. Y.: Synthesis and characterization of soluble polypyrrole. *Synthetic Metals*, **84**, 137–140 (1997).  
DOI: [10.1016/S0379-6779\(97\)80683-2](https://doi.org/10.1016/S0379-6779(97)80683-2)
- [9] Oh E. J., Jang K. S., Suh J. S., Kim H., Kim K. H., Yo C. H., Joo J.: UV-Vis./NIR and transport studies of chemically synthesized soluble polypyrrole. *Synthetic Metals*, **84**, 147–148 (1997).  
DOI: [10.1016/S0379-6779\(97\)80686-8](https://doi.org/10.1016/S0379-6779(97)80686-8)
- [10] Shen Y., Wan M.: In situ doping polymerization of pyrrole with sulfonic acid as a dopant. *Synthetic Metals*, **96**, 127–132 (1998).  
DOI: [10.1016/S0379-6779\(98\)00076-9](https://doi.org/10.1016/S0379-6779(98)00076-9)
- [11] Wu T.-M., Chang H.-L., Lin Y.-W.: Synthesis and characterization of conductive polypyrrole with improved conductivity and processability. *Polymer International*, **58**, 1065–1070 (2009).  
DOI: [10.1002/pi.2634](https://doi.org/10.1002/pi.2634)
- [12] Cairns D. B., Armes S. P., Chehimi M. M., Perruchot C., Delamar M.: X-ray photoelectron spectroscopy characterization of submicrometer-sized polypyrrole–polystyrene composites. *Langmuir*, **15**, 8059–8066 (1999).  
DOI: [10.1021/la990443k](https://doi.org/10.1021/la990443k)
- [13] Jaramillo A., Spurlock L. D., Young V., Brajter-Toth A.: XPS characterization of nanosized overoxidized polypyrrole films on graphite electrodes. *Analyst*, **124**, 1215–1221 (1999).  
DOI: [10.1039/A902578B](https://doi.org/10.1039/A902578B)
- [14] Ruangchuay L., Schwank J., Sirivat A.: Surface degradation of  $\alpha$ -naphthalene sulfonate-doped polypyrrole during XPS characterization. *Applied Surface Science*, **199**, 128–137 (2002).  
DOI: [10.1016/S0169-4332\(02\)00564-0](https://doi.org/10.1016/S0169-4332(02)00564-0)
- [15] Nicho M. E., Hu H.: Fourier transform infrared spectroscopy studies of polypyrrole composite coatings. *Solar Energy Materials and Solar Cells*, **63**, 423–435 (2000).  
DOI: [10.1016/S0927-0248\(00\)00061-1](https://doi.org/10.1016/S0927-0248(00)00061-1)
- [16] Ekramul Mahmud H. N. M., Kassim A., Zainal Z., Yunus W. M. M.: Fourier transform infrared study of polypyrrole–poly(vinyl alcohol) conducting polymer composite films: Evidence of film formation and characterization. *Journal of Applied Polymer Science*, **100**, 4107–4113 (2006).  
DOI: [10.1002/app.23327](https://doi.org/10.1002/app.23327)
- [17] Menon V. P., Lei J., Martin C. R.: Investigation of molecular and supermolecular structure in template-synthesized polypyrrole tubules and fibrils. *Chemistry of Materials*, **8**, 2382–3290 (1996).  
DOI: [10.1021/cm960203f](https://doi.org/10.1021/cm960203f)
- [18] Baughman R. H., Shacklette L. W.: Conductivity as a function of conjugation length: Theory and experiment for conducting polymer complexes. *Physical Review B*, **39**, 5872–5886 (1989).  
DOI: [10.1103/PhysRevB.39.5872](https://doi.org/10.1103/PhysRevB.39.5872)
- [19] Pruneanu S., Graupner W., Oniciu L., Brie M., Turcu R.: Electrochemical and X-ray diffraction studies on polypyrrole films. *Materials Chemistry and Physics*, **46**, 55–60 (1996).  
DOI: [10.1016/0254-0584\(96\)80130-1](https://doi.org/10.1016/0254-0584(96)80130-1)
- [20] Ormond-Prout J., Dupin D., Armes S. P., Foster N. J., Burchell M. J.: Synthesis and characterization of polypyrrole-coated poly(methyl methacrylate) latex particles. *Journal of Materials Chemistry*, **19**, 1433–1442 (2009).  
DOI: [10.1039/b816839c](https://doi.org/10.1039/b816839c)
- [21] Gu Z., Zhang L., Li C.: Preparation of highly conductive polypyrrole/graphite oxide composites via *in situ* polymerization. *Journal of Macromolecular Science Part B: Physics*, **48**, 1093–1102 (2009).  
DOI: [10.1080/00222340903035576](https://doi.org/10.1080/00222340903035576)
- [22] Gao J.-W., Li G., Yao Y.-F., Jang J.-M.: Preparation and characterization of montmorillonite/polypyrrole nanocomposites by *in-situ* chemical polymerization. *Journal of Macromolecular Science Part B: Physics*, **50**, 1364–1375 (2011).  
DOI: [10.1080/00222348.2010.497688](https://doi.org/10.1080/00222348.2010.497688)
- [23] Joo J., Lee J. K., Baeck J. S., Kim K. H., Oh E. J., Epstein J.: Electrical, magnetic, and structural properties of chemically and electrochemically synthesized polypyrroles. *Synthetic Metals*, **117**, 45–51 (2001).  
DOI: [10.1016/S0379-6779\(00\)00537-3](https://doi.org/10.1016/S0379-6779(00)00537-3)
- [24] Shen Y., Wan M.: Soluble conductive polypyrrole synthesized by *in situ* doping with  $\beta$ -naphthalene sulfonic acid. *Journal of Polymer Science Part A: Polymer Chemistry*, **35**, 3689–3695 (1997).  
DOI: [10.1002/\(SICI\)1099-0518\(199712\)35:17<3689::AID-POLA8>3.0.CO;2-N](https://doi.org/10.1002/(SICI)1099-0518(199712)35:17<3689::AID-POLA8>3.0.CO;2-N)
- [25] Jeon I.-Y., Choi H.-J., Tan L.-S., Baek J.-B.: Nanocomposite prepared from *in situ* grafting of polypyrrole to aminobenzoyl-functionalized multiwalled carbon nanotube and its electrochemical properties. *Journal of Polymer Science Part A: Polymer Chemistry*, **49**, 2529–2537 (2011).  
DOI: [10.1002/pola.24684](https://doi.org/10.1002/pola.24684)

- [26] Demoustier-Champagne S., Stavaux P. Y.: Effect of electrolyte concentration and nature on the morphology and the electrical properties of electropolymerized polypyrrole nanotubules. *Chemistry of Materials*, **11**, 829–834 (1999).  
DOI: [10.1021/cm9807541](https://doi.org/10.1021/cm9807541)
- [27] Gupta S.: Hydrogen bubble-assisted syntheses of polypyrrole micro/nanostructures using electrochemistry: Structural and physical property characterization. *Journal of Raman Spectroscopy*, **39**, 1343–1355 (2008).  
DOI: [10.1002/jrs.2002](https://doi.org/10.1002/jrs.2002)
- [28] Luo Y-L., Fan L-H., Xu F., Chen Y-S., Zhang C-H., Wei Q-B.: Synthesis and characterization of Fe<sub>3</sub>O<sub>4</sub>/PPy/P(MAA-co-AAm) trilayered composite microspheres with electric, magnetic and pH response characteristics. *Materials Chemistry and Physics*, **120**, 590–597 (2010).  
DOI: [10.1016/j.matchemphys.2009.12.002](https://doi.org/10.1016/j.matchemphys.2009.12.002)
- [29] Ruangchuay L., Schwank J., Sirivat A.: Surface degradation of  $\alpha$ -naphthalene sulfonate-doped polypyrrole during XPS characterization. *Applied Surface Science*, **199**, 128–137 (2002).  
DOI: [10.1016/S0169-4332\(02\)00564-0](https://doi.org/10.1016/S0169-4332(02)00564-0)
- [30] MacDiarmid A. G., Epstein A. J.: Polyanilines: A novel class of conducting polymers. *Faraday Discussions of the Chemical Society*, **88**, 317–332 (1989).  
DOI: [10.1039/DC9898800317](https://doi.org/10.1039/DC9898800317)
- [31] Malitesta C., Losito I., Sabbatini L., Zambonin P. G.: New findings on polypyrrole chemical structure by XPS coupled to chemical derivatization labelling. *Journal of Electron Spectroscopy and Related Phenomena*, **76**, 629–634 (1995).  
DOI: [10.1016/0368-2048\(95\)02438-7](https://doi.org/10.1016/0368-2048(95)02438-7)
- [32] Andreoli E., Rooney D. A., Redington W., Gunning R., Breslin C. B.: Electrochemical deposition of hierarchical micro/nanostructures of copper hydroxysulfates on polypyrrole–polystyrene sulfonate films. *The Journal of Physical Chemistry C*, **115**, 8725–8734 (2011).  
DOI: [10.1021/jp200465n](https://doi.org/10.1021/jp200465n)
- [33] Omastová M., Mravčáková M., Chodák I., Pionteck J., Häussler L.: Conductive polypropylene/clay/polypyrrole nanocomposites. *Polymer Engineering and Science*, **46**, 1069–1078 (2006).  
DOI: [10.1002/pen.20551](https://doi.org/10.1002/pen.20551)
- [34] Yuvaraj H., Shim J-J., Lim K. T.: Organic–inorganic polypyrrole-surface modified SiO<sub>2</sub> hybrid nanocomposites: A facile and green synthetic approach. *Polymers for Advanced Technologies*, **21**, 424–429 (2010).  
DOI: [10.1002/pat.1448](https://doi.org/10.1002/pat.1448)
- [35] Mpoukouvalas K., Wang J., Wegner G.: Conductivity of poly(pyrrole)-poly(styrene sulfonate) core–shell nanoparticles. *ChemPhysChem*, **11**, 139–148 (2010).  
DOI: [10.1002/cphc.200900643](https://doi.org/10.1002/cphc.200900643)
- [36] Bose S., Kuila T., Uddin M. E., Kim N. H., Lau A. K. T., Lee J. H.: In-situ synthesis and characterization of electrically conductive polypyrrole/graphene nanocomposites. *Polymer*, **51**, 5921–5928 (2010).  
DOI: [10.1016/j.polymer.2010.10.014](https://doi.org/10.1016/j.polymer.2010.10.014)
- [37] Beck F., Braun P., Oberst M.: Organic electrochemistry in the solid state-overoxidation of polypyrrole. *Berichte der Bunsen-Gesellschaft*, **91**, 967–974 (1987).

# Injection moulding of long glass fibre reinforced poly(ethylene terephthalate): Influence of carbon black and nucleating agents on impact properties

L. Cilleruelo<sup>1,2</sup>, E. Lafranche<sup>1,2\*</sup>, P. Krawczak<sup>1,2</sup>, P. Pardo<sup>3</sup>, P. Lucas<sup>3</sup>

<sup>1</sup>Université Lille Nord de France, 59000 Lille, France

<sup>2</sup>Ecole des Mines de Douai, Polymers and Composites Technology & Mechanical Engineering Department, 941 rue Charles Bourseul, BP 10838, 59508 Douai, France

<sup>3</sup>OCV Reinforcements, 767 Quai des Allobroges, BP 929, 73009 Chambéry, France

Received 3 January 2012; accepted in revised form 16 March 2012

**Abstract.** This paper aims at highlighting the influence of different additives (carbon black and nucleating agents) on both the notched and unnotched Charpy impact properties of long glass fibre reinforced poly(ethylene terephthalate) injection mouldings. The relationship with the polymer matrix and composite microstructure modifications (variations of crystalline morphology and local fibre content) was investigated. Adding carbon black alone decreases the impact performances. This highly conductive additive actually increases the cooling rate, and therefore the fibre ‘fretage’ effect (higher internal stresses). It also acts as filler, which increases the material brittleness. The nucleating agents allow reducing the mould temperature, but their effect on the impact strength may be favourable or not depending on the processing temperatures. The addition of such additives induces perturbations of the polymer melt rheology in the mould cavity and of the cooling kinetics of the part, which both act on the fibre distribution during mould filling and on the degree of crystallinity of the composite parts.

**Keywords:** polymer composites, long fibre thermoplastics, mechanical properties, nucleating agent, carbon black

## 1. Introduction

Combining some advantages of short glass fibre reinforced thermoplastics (e.g. easy processing by injection moulding) and GMT (Glass Mat reinforced Thermoplastic) composites (e.g. continuous fibre), long glass fibre reinforced thermoplastics (LFT) are finding ever-growing applications due to their excellent short and long term mechanical performances compared to their challengers. For instance in the automotive industry, LFTs show a great potential for metal substitution in terms of both cost-effectiveness and vehicle lightening [1, 2]. The marketed LFT compounds were originally limited to polypropylene (PP) reinforcement and

numerous studies are therefore available on this material (among others, an excellent paper series by Thomason and coworkers [3–9]). Other matrices are now also commercially available, such as polyamides (PA) 6 or 6-6 and polyesters (poly(ethylene terephthalate) (PET), poly(butylene terephthalate) (PBT)) among others. Unfortunately, the scientific literature is much more limited on PA 6-6 [10–16], and even more on PET [17] based LFTs.

Whatever is the forecasted industrial application, LFT-based solutions require in numerous cases a subtle balance between the short term mechanical properties and the durability, the mechanisms of brittleness and damage being in close relation with

\*Corresponding author, e-mail: [eric.lafranche@mines-douai.fr](mailto:eric.lafranche@mines-douai.fr)

the loading velocity. Generally, the failure of chopped fibre composites is mainly governed by fibre breakage in case of long fibres, and by the deformation of the matrix and the fibre/matrix debonding in case of short fibres [18]. The literature shows [15, 18–22] that the impact strength of the LFT is strongly influenced by the fibre residual length, concentration, distribution and orientation in the part, as well as by factors depending on processing and testing conditions (impact speed, temperature, presence of notch in the sample, etc.), much more in the case of high loading speed (typically in the range of a couple of  $\text{m}\cdot\text{s}^{-1}$ ) than in the case of low loading velocity (typically in the range of 1 to  $100\text{ mm}\cdot\text{min}^{-1}$ ).

Karger-Kocsis [19] reported a comparative analysis of notched Charpy impact behaviour of polypropylene (PP) reinforced with different long and short fibre contents. The ductility index (DI = crack growth energy/total breakage energy) increases with increasing fibre volume fraction of long fibres, whereas it quickly reaches a maximum and then drops in the case of short fibres. These trends were confirmed by Vu-Khanh and Denault [20]. These authors observed that the impact strength of chopped fibre polypropylene composites increases at lower temperatures and for parts reinforced with the longest fibres. Also, Thomason and Vluc [6] established the relationship existing between the fibre content and the impact strength of PP composites with different fibre lengths. The impact strength increases almost linearly with the fibre weight content and reaches an asymptote (plateau) when fibres are longer than 6 mm. More recently, the same author reported that the notched impact strength is the highest when fibre contents are in the range 40–50 wt%, whereas the maximum of the unnotched impact strength appears at a fibre content of about 30 wt% only [8]. The impact strength quickly drops above these limits. Moreover, as for the tensile or flexural strengths [5, 8, 10, 14, 15] different authors evidenced that the residual fibre length and the fibre orientations influence the impact strength [8, 21].

In the case of PP reinforced with 50 wt% glass fibres having initial fibre length of 10 mm (reduced to 1.8–2.0 mm after injection moulding), Skourlis *et al.* [22] furthermore highlighted the influence of the thickness of the skin and core layers of the part, induced by the shear and fountain flows during processing. As the reinforcement effect is related to the

fibre alignment along the flow direction, the processing parameters which favour the fibre orientation in the skin layer and the increase of its thickness (e.g. low mould temperature and low injection speed) lead to impact strength increase [22]. Cilleruelo *et al.* [17] confirmed that it is possible to optimise the impact strength of 30 wt% long fibre reinforced poly(ethylene terephthalate) (PET) by properly setting the two above-mentioned main influencing parameters, however at opposite setting levels compared to those recommended to optimise flexural properties [11, 15].

Beyond the factors mentioned previously, the incorporation of additives in the thermoplastic matrices (pigments/dyes, nucleating agents, etc.) which are likely to modify the structure of the composite (matrix morphology and fibre/matrix interphase), may also induce variations in mechanical performance, particularly in impact strength. Carbon black is the most used pigment in the plastics industry, particularly for automotive applications. Carbon black is available in the form of granules, fibres or powder. It is composed of crystalline agglomerated elements (micro-crystals). This ability to agglomerate induces the formation of a spatial network within the filled polymer that behaves as fibrous fillers. Its peculiar geometry modifies the polymer structure and causes a decrease in the material strength even at low concentrations [23]. It may also affect the polymer crystallisation acting as heterogeneous nucleating agent, and modifies the crystallisation kinetics and temperature.

Besides, nucleating agents (e.g. most commonly carboxylate or phosphate ester salts, and sorbitol acetals) are often added to semi-crystalline polymers such as PET [24–27] or PP [28, 29] in order to modify the crystallisation kinetics and mechanism (increase of the crystallisation rate, leading to a faster polymer solidification), consequently leading to injection moulding cycle time reduction. In particular, PET is characterised by a very slow crystallisation and nucleating agents are often added to control a more homogeneous structure through a uniform spherulite size more than to increase the degree of crystallinity of the polymer. The sodium salts usually used as nucleating agent do not act as nucleation centres themselves but interact with the PET molecules to give sodium terephthalate chains that are the effective nucleating species. These nucle-

ophilic substitution chemical reactions induce a global molecular weight decrease of the polymer [24–26]. Sodium benzoate nucleating agent is well-known to substantially increase the crystallization rate of poly(ethylene terephthalate) at higher temperature and to accelerate crystallization even more at lower temperature with an additional improvement of molecular mobility of PET chains, but the increase of crystallization rate is limited by the fact that sodium benzoate may be only partially soluble in PET matrix [26, 27]. The sodium 2,2'-methylenebis(4,6-di-tert-butylphenyl)phosphate nucleating agent is usually used to increase the crystallization rate of polyolefins, polyamides and PET; it may induce smaller spherulites than sodium benzoate at higher crystallization temperature with shorter crystallization half time [28, 29]. On the other hand, the nucleating agents strongly influence the crystalline zone between the fibre and the matrix. This zone is constituted by three areas the first one is the interface between the fibre and the transcrystalline phase of the polymer, the second one is the transcrystalline homogeneous part influenced by the cooling rate, the fibre treatment, the free surface of the fibre or by the nucleating agents, and the third one is the interphase between the transcrystalline phase and the matrix [30].

As a consequence, the composites mechanical properties (e.g. strength, toughness, brittleness) may be strongly affected. In particular, smaller spherulites resulting from nucleating agents addition are likely to improve the impact strength of crystalline matrices [31–33]. However, to our better knowledge, the influence of carbon black and/or nucleating agents addition on impact properties has never been reported in the case of PET-based LFTs.

In this context, as long glass fibre/PET compounds were rarely studied, the optimisation of long glass fibre/poly(ethylene terephthalate) injection moulding still needs dedicated research efforts. The effect

of injection moulding conditions and the existence of fibre segregation phenomena along the flow path and through the thickness were reported in a previous paper [17]. In the present paper, the influence of different additives (carbon black and nucleating agents) on the Charpy impact properties of long glass fibre/PET injection-mouldings is investigated. The relationship with the polymer matrix and composite microstructure modifications (variations of crystalline morphology and local fibre content) is highlighted.

## 2. Experimental

### 2.1. Materials

The material studied was a poly(ethylene terephthalate) (PET) reinforced by 30 wt% of 12.5 mm long glass fibres (LGF) having an 18  $\mu\text{m}$  diameter. It was obtained by diluting concentrated glass/PET commingled pellets (Twintex<sup>®</sup>, Saint-Gobain Vetrotex International, France) having a nominal fibre-glass content of 65 wt% in a PET matrix of 0.65 viscosity index IV (Acordis<sup>®</sup>, Acordis Industrial Fibers, The Netherlands). This standard formulation of PET containing 30 wt% glass fibres is named R0 (no additives) here after.

This 'virgin' material reference (R0) was modified by the addition of carbon black (compounds R1, R2 and R3) and nucleating agents (compounds R2 and R3) (Table 1). The R1 formulation is filled with carbon black but contains no nucleating agent. The two other formulations contain nucleating agents. These are sodium benzoate (109494, Ciba, Germany) in case of R2 formulation and sodium 2,2'-methylenebis-(4,6-di-tert-butylphenyl)phosphate (Irgastab<sup>®</sup> NA11, Ciba, Germany) in case of R3 formulation. An oxidation inhibitor (Irganox<sup>®</sup> 1010, Ciba, Germany) was also added into the matrix for all formulations. The additives (masterbatches) and concentrated glass/PET pellets were directly weighed and mixed with the neat PET material using a four com-

**Table 1.** Compounds formulations

Additive formulation (commercial reference)		Virgin	Carbon black only	Carbon black and nucleating agent	
		R0	R1 (109833)	R2 (109494)	R3 (109834)
Quantity added into the matrix	Additive	–	3%	5%	3%
	Carbon black	–	0.21%	0.21%	0.21%
	Oxidation inhibitor	0.11%	0.11%	0.11%	0.11%
	Nucleating agent	–	–	0.11%	0.11%
Average* fibre weight content (standard deviation)		33.3 (2.8)	31.3 (5.3)	31.3 (4.3)	31.5 (5.0)

\*measured over the entire plate

ponent weight blender (WSB 140, Maguire Product Inc., USA).

**2.2. Machine and mould**

The experiments were carried out on a 2000 kN clamping force injection-moulding machine (DK Codim, France). The machine has a vertical clamping unit (injection gate located in the mould parting line), and is equipped with a 55 mm diameter screw specially designed for long glass fibre reinforced composites processing (Euro-Stel, Belgium).

The prototype injection mould is a rectangular plate of 300 × 120 × 3 mm (Figure 1). A 4 mm thick fan gate feeds the cavity over its whole width (unidirectional flow in the longitudinal direction of the plate (Figure 1b)). This mould was specially designed so as to reproduce some geometrical discontinuities (like sharp frontal and tangential steps) occurring on real industrial moulds that locally disturb the melt flow and consequently induce local micro structural heterogeneity (Figure 1a). Three pressure transducers are located at 40, 110 and 220 mm from the gate and are associated with two temperature sensors at 40 and 220 mm.

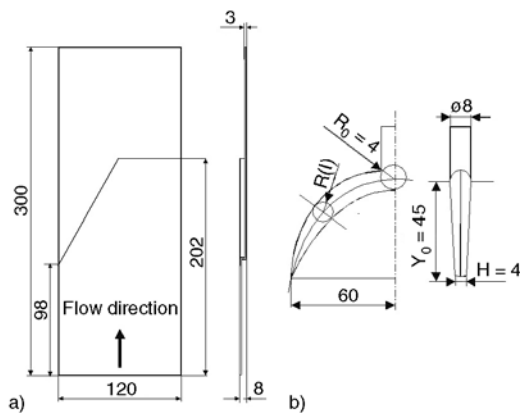


Figure 1. Plastic part (a) and gates geometries (b)

Table 2. Optimal moulding conditions from Taguchi DOE [17]

Processing parameters	Set up value
Mould temperature [°C]	150
Melt temperature [°C]	295
Volumetric flow rate [cm <sup>3</sup> ·s <sup>-1</sup> ]	178
Holding pressure [bar]	605
Back pressure [bar]	8
Screw rotation speed [rpm]	40
Cooling time [s]	20

**2.3. Moulding conditions**

A Taguchi Design of Experiments (DOE) [34] was used in a previous study in order to identify the main process parameters responsible for anisotropy and heterogeneity of the moulded part, and then to optimise the injection moulding process [17]. The moulding conditions resulting from this DOE used to manufacture the parts are summarised in Table 2.

**2.4. Impact testing**

Charpy impact tests were performed in order to determine the impact strength according to ISO 179-1 or 179-2 (instrumented impact test) on a standard pendulum impact machine (Model 5101, Zwick, Germany) at 3.8 mm·s<sup>-1</sup> with an 7.5 Joules impactor on ten 80 × 10 × 3 mm samples. The tests were carried out on V-shaped notched samples (type A: notched radius 0.25 mm, remaining width 8 mm) in edgewise position and on unnotched samples in flatwise position. The test sample was cut out of the injection-moulded plates in either flow or longitudinal (1, FD) and transverse (2, TD) directions before (beginning section, B) and after (end section, E) the step as shown in Figure 2. The impact strength was calculated according to Equation (1):

$$IS = \frac{E_c}{h \cdot b} \cdot 10^3 \tag{1}$$

where *IS* [kJ·m<sup>-2</sup>] is the impact strength, *E<sub>c</sub>* [J] the corrected impact energy, *h* [mm] the sample thickness, and *b* [mm] the sample width (unnotched test) or remaining sample width (notched test).

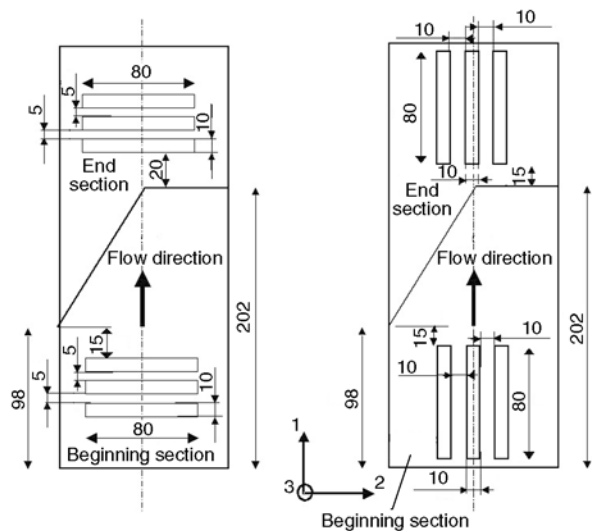
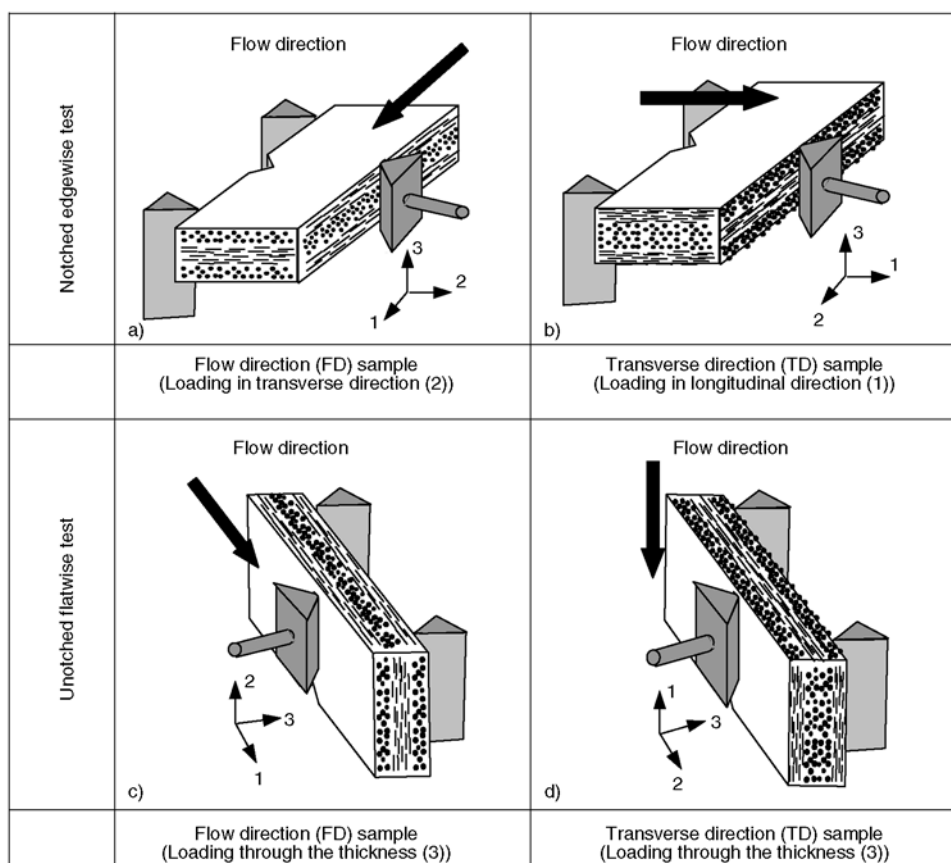


Figure 2. Location of test samples in the plate



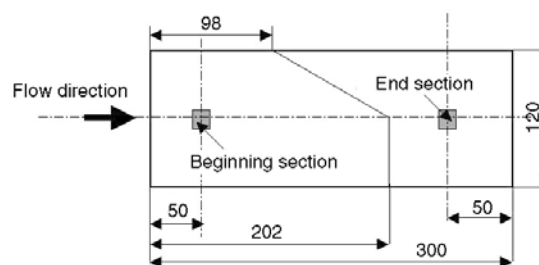
**Figure 3.** Charpy impact test configuration: Loading directions with respect to the sample multilayer structure

The loading directions of the samples are presented with respect to the induced skin/core microstructure of the samples in Figure 3. The shear and fountain flows occurring during cavity filling actually induce a well-known multilayer structure with skin layers showing a fibre orientation in the flow direction and a core layer where the fibres are oriented transversally to the flow [10, 11, 24].

The loading mode applied during the Charpy impact test is bending. This means that the normal tension-compression stresses applied are the highest on the sample surfaces (and equal to zero on the mid-plane). In edgewise position, all the three layers (skins and core) are subjected to the tensile or compressive loading and contribute to sustain these maximal stresses. In flatwise position, only the surface skin layers are preferentially loaded and subjected to the maximal tensile or compressive stresses. Carrying out the two types of impact test makes it therefore possible to assess relative effect of the skin.

**2.5. Fibre content measurement**

The fibre weight content was determined by ashing technique according to ASTM D 2584. The meas-



**Figure 4.** Cutting pattern of test samples for fibre weight content determination

urements were carried out on 25 × 25 mm samples cut from three injection-moulded parts according to the cutting pattern shown in Figure 4. The average fibre weight content was also measured over the entire plate (results are reported in Table 1).

**2.6. Degree of crystallinity measurement**

The degree of crystallinity was determined on a differential scanning calorimeter (DSC7, Perkin Elmer, USA) with a heating rate of 20°C/min. A thermogravimetric analysis (TGA, Perkin Elmer, USA) was carried out in order to obtain the local matrix and fibre weight contents. The degree of crystallinity,  $X_{cr}$  was calculated (Equation (2)) from the measure-



ments of the melt enthalpy,  $\Delta H_F$  and the cold crystallisation enthalpy,  $\Delta H_c$ , using the melt enthalpy of a fully crystalline poly(ethylene terephthalate),  $\Delta H_{F\infty}$  (140 J/g) [35] and the matrix weight content in the sample,  $m_{PET}$  (Equation (2)):

$$X_{cr} = 100 \cdot \frac{\Delta H_F - \Delta H_c}{\Delta H_{F\infty}} \cdot \frac{m_{PET}}{m} \quad (2)$$

where  $m$  is the composite weight. The measurements were carried out three times per sample at 50 and 250 mm from the injection gate on the plate symmetry axis.

### 3. Results and discussion

#### 3.1. Influence of the addition of carbon black

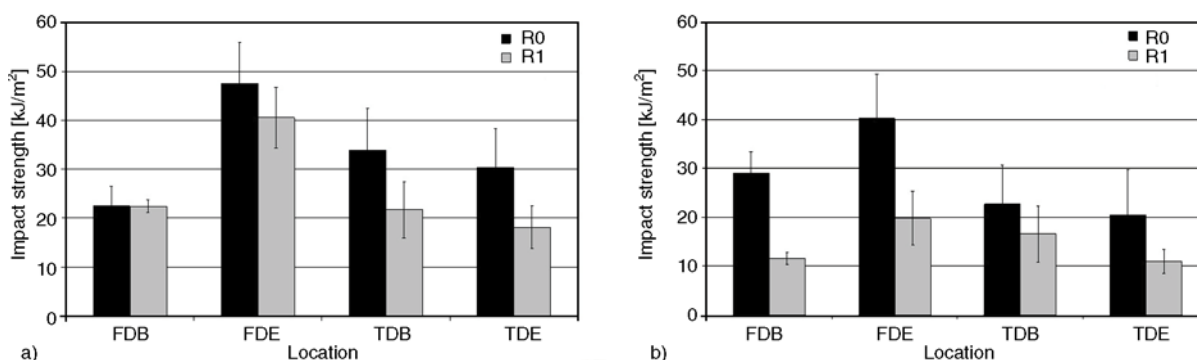
Figure 5 shows that carbon black addition (R1 formulation compared to R0) significantly reduces the impact strength of the composites. The property drop is higher for notched samples (Figure 5b).

In the unnotched flatwise impact test configuration, only the skin layers sustain the mechanical loading (highest tensile-compressive normal stresses) and thus participate to the reinforcement (Figures 3c and 3d). In the case of the flow direction (FD) samples (Figure 3c), the preferential orientation of fibres in the skin layers coincides with the sample length. The impact fracture energy is not affected by carbon black addition at the beginning section (B) of the part and is only slightly lower (15%) at the end section (E) of the part (Figure 5a). In that case, this is the aligned fibres that are loaded principally; the impact behaviour modification due to the addition of carbon black into the matrix is thus limited. In the case of transverse (TD) samples, the skin layers supporting the highest normal stresses have aligned fibres preferentially oriented through the sample width (Figure 3d). The strength decrease is much

more noticeable and reaches more than 35% wherever the measurement location is. In that case, it is the matrix that is principally loaded. Its modification by carbon black addition therefore significantly influences the impact behaviour accordingly.

In the notched edgewise impact test configuration, the entire multi-layered structure of the composite is subjected to mechanical loading; all the layers, i.e. both the skin and core layers, contribute to sustain the highest normal stresses and thus contribute to the impact resistance (Figures 3a and 3b). As a consequence, whatever the sample direction may be, there is at least one layer (either skin or core) for which the preferential fibre alignment does not match the normal stresses principal direction, that is to say for which the matrix is principally loaded. Thus, the addition of carbon black always induces a significant strength decrease. This decrease is about 50% for flow direction (FD) samples, and about 35% for transverse direction (TD) samples. As there is a fibre accumulation in the core layer due to fibre segregation phenomena reported previously [11, 17], the effect of the matrix brittleness is higher for the flow direction samples (most of the fibres are aligned in the impact direction (Figure 3a)).

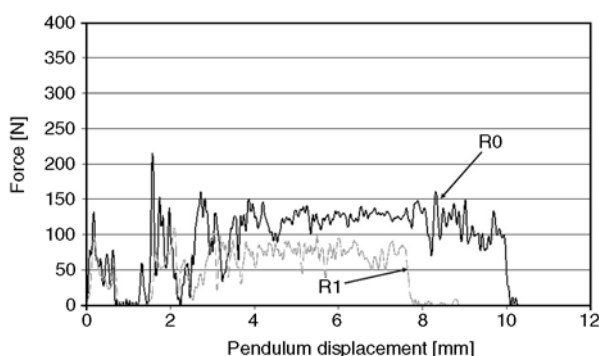
Recording the force/displacement curves provides data related to damage initiation and growth. In the unnotched flatwise impact test configuration, the energy dissipated during the fracture (area under the curve) are 1.3 times higher for the virgin formulation (R0) than for the black formulation (R1) in the transverse direction (Figure 6). It is however mainly the crack growth energy that differentiates both formulations. In the notched edgewise impact test configuration, in the flow direction where the carbon black induced weakening is the highest, the composites moulded with the black coloured com-



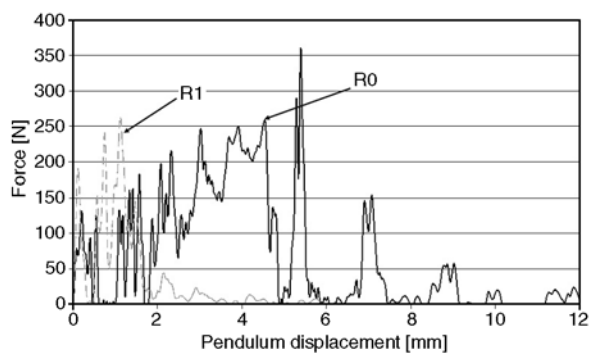
**Figure 5.** Unnotched flatwise (a) and notched edgewise (b) Charpy impact strengths in flow (FD) and transverse directions (TD) at beginning (B) and end (E) of the part – Effect of carbon black (R1) compared to virgin (R0) PET/30 wt% LGF

compound (R1) clearly resist less to crack growth (Figure 7); breakage rapidly occurs after crack initiation.

Carbon black influences the matrix crystallization, its particles forming nucleating sites [30] as glass fibres do. The measurement of the degree of crystallinity at the conventional locations (beginning and end sections of the part) indicates a homogenisation of the microstructure of the carbon black coloured part (R1) compared to the virgin one (R0). This noticeable effect has to be linked to the impor-



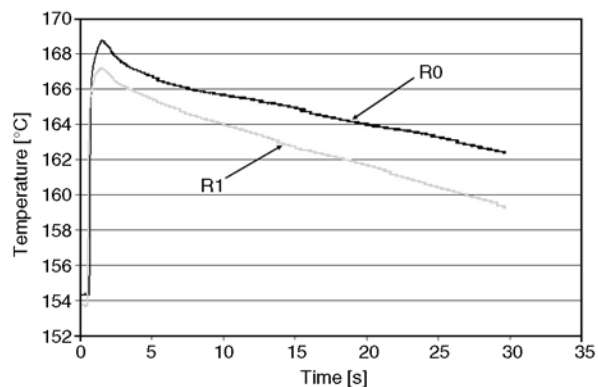
**Figure 6.** Force/displacement curve recorded during unnotched flatwise Charpy impact test in transverse direction at the beginning of the part – Effect of carbon black (R1) compared to virgin (R0) PET/30 wt% LGF



**Figure 7.** Force/displacement curve recorded during notched edgewise Charpy impact test in flow direction at the beginning of the part – Effect of carbon black (R1) compared to virgin (R0) PET/30 wt% LGF

tant fibre content decrease at the end of the plate (Table 3), fibres acting themselves as nucleating sites. The local fibre content is 8 wt% lower compared the virgin (R0) formulation may partly explain the impact strength drop at this location. Nonetheless, at the beginning of the part where fibre content and degree of crystallinity are similar, the notched impact strengths are still lower for the black coloured parts (R1).

Processing related data may explain the above-mentioned reduction of fibre segregation effect. Lower filling time (0.2 s measured in front of each pressure sensors) was recorded for the black coloured compound R1, that is to say lower pressure loss, suggesting higher fluidity. As a direct consequence, this viscosity diminution decreases the shear stresses in the melt flow and thus the previously noticed [11, 17] fibre segregation occurring during cavity filling. Thanks to its good thermal conductivity, carbon black induces a quicker cooling of the polymer in the cavity (Figure 8), thus shorter freezing times that decrease the holding phase efficiency. Carbon black seems therefore to act not only as a thermal transfer activator but also as a mechanical fluidization agent (lubricating agent) in the same way as talc or glass beads.



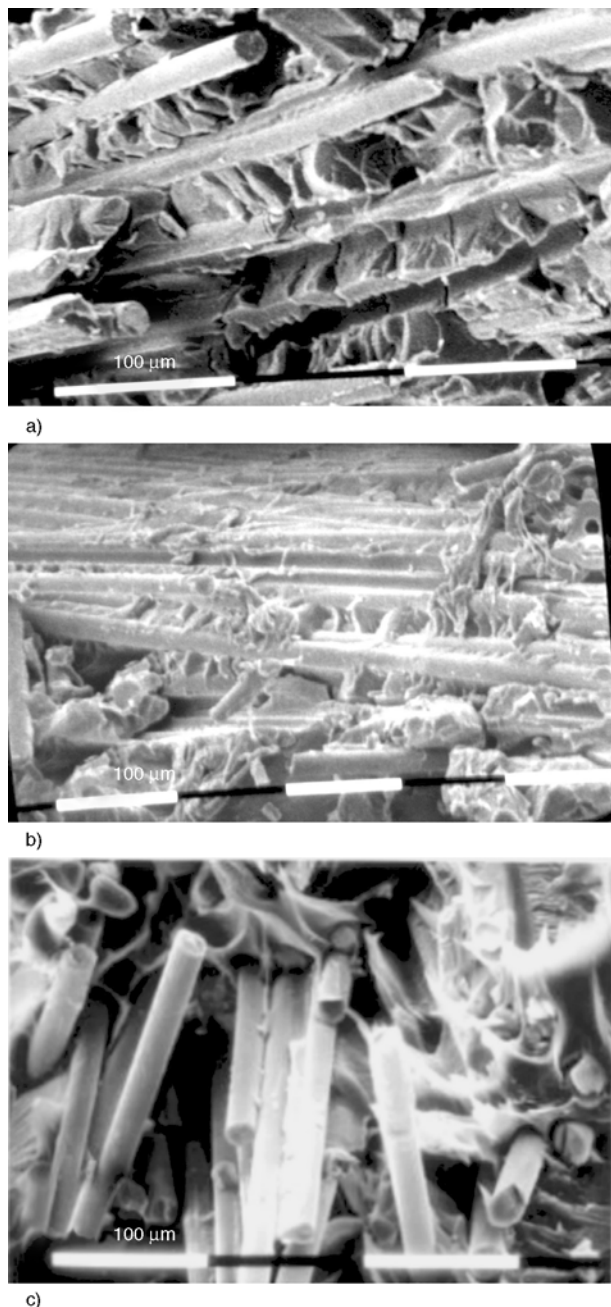
**Figure 8.** Part temperature during cooling in the mould at 40 mm from the gate – Effect of carbon black (R1) compared to virgin (R0) PET/30 wt% LGF

**Table 3.** Influence of nucleating agents, carbon black and mould temperature on the part microstructure

PET/30 wt% LGF reference	Mould temperature [°C]	Fibre content [wt%]				Degree of crystallinity $X_{cr}$ [%]			
		Beginning	SD*	End	SD*	Beginning	SD*	End	SD*
R0	150	30.6	0.8	38.2	2.6	30.9	4.6	39.1	1.8
R1	150	28.9	7.2	30.3	2.4	28.3	4.1	28.9	4.3
R2	150	29.5	6.0	33.1	0.4	36.8	1.8	36.1	2.0
R3	150	31.4	5.0	30.6	1.8	31.6	2.0	31.9	1.9
R2	140	28.7	5.6	33.9	1.1	32.3	2.2	30.7	3.3
R3	140	36.0	1.7	39.6	1.5	33.7	2.0	33.7	2.7

\*SD: Standard deviation

Besides, carbon black also acts as filler. It reduces the matrix ductility [36] and creates brittleness sites that participate to the composite fracture at low stress levels. The impact brittleness then depends on both the filler content and size [36, 37]. The fracture surfaces of the carbon black coloured material (R1) indicate a good fibre/matrix adhesion with limited fibre pull-out and debonding (Figures 9a and 9b). The matrix does not show any polymer strips to



**Figure 9.** Fracture surfaces after notched edgewise (a, c) or unnotched flatwise (b) Charpy impact test at plate beginning for R1 (a, b) and R0 (c) formulation

be related to plastic deformation but many cracks normal to the fibres (Figure 9a) probably originating from stress concentrations around them. The fracture surface of the virgin material (R0) is fully different (Figure 9c) showing smooth fibres and fibre pull-out, signs of poor fibre/matrix adhesion. The better fibre/matrix adhesion observed for R1 (compared to R0) may be ascribed to the so-called ‘fretage’ stresses (shrink-fitting or coiling effect), induced by the shrinkage of the matrix around the fibres and already explained elsewhere [17, 38]. This fibre ‘fretage’ effect depends on the cooling rate of the part (higher for R1 than for R0 as mentioned above). The latter also governs the stress relaxation ability of the material. At high cooling rate, the internal fretage stresses are frozen, cannot relax easily; the matrix is therefore pre-loaded and is much more sensitive to microcracking around the fibres when further mechanically loaded. The good interfacial adhesion is responsible for the low impact strength of the carbon black coloured material (R1), owing to the fact that its ability to dissipate the impact energy by fibre/matrix debonding and fibre pull-out is poor. The impact strength also depends on matrix ductility as well as on the amplitude of the fretage stresses around the fibres: The higher the matrix ductility and the lower the internal fretage stresses, the higher the impact strength of the material (case of R0 formulation).

### 3.2. Influence of the addition of nucleating agents

From an industrial standpoint, nucleating agents are often used to promote a quicker crystallization of the injection-moulded parts (modification of the crystallization kinetics of the matrix) in order to reduce cycle times or mould temperature. They are also likely to modify the (transcrystalline) inter-phase structure [36]. Knowing that the very first damage step of long fibre reinforced thermoplastics is fibre/matrix debonding [4], the impact behaviour may be consequently affected by nucleating agent addition. It is therefore worth assessing the influence on the impact properties of the addition of nucleating agents on the one hand, of their chemical nature on the other hand, and finally of the mould temperature (which governs the parts cooling rate).

### 3.2.1. Effect of nucleating agents

Consequently, this section is first going to focus on the three black coloured formulations (R1, R2, R3) injection-moulded in the standard conditions (mould temperature at 150°C, Table 2) in order to investigate the influence of different types of nucleating agents. Adding a nucleating agent such as sodium benzoate (R2) to the carbon black coloured compound allows improving its impact strength whatever the test configuration may be.

The chemical nature of the nucleating agent (sodium benzoate R2 or sodium 2,2'-methyl-4,6-di-tert-butylphenylphosphate R3) particularly influences the unnotched flatwise impact strength. The best mechanical performance is achieved with the sodium benzoate based (R2) formulation as shown in Figure 10a. The impact strength reached with this additive is always higher than that measured for the R1 formulation, which is not the case with the sodium phosphate nucleating agent (R3). In the notched edgewise impact test configuration, the addition of a nucleating agent (R2 or R3) improves the impact strength of the material (compared to R1), R2 being more efficient than R3. In this test configuration, where the entire multi-layered composite structure is submitted to mechanical loading and participates to sustain the applied maximum normal stresses, the chemical nature of the nucleating agent (R2 or R3) has only a limited effect on the impact strength in flow direction. A significant impact strength improvement is however noticed for the sodium benzoate based formulation (R2) in the transverse direction (+30% on average between the two formulations) (Figure 10b). Such a better efficiency of sodium benzoate (R2) compared to phosphate based (R3) nucleating agent may be surpris-

ing. Indeed, according to the literature, sodium 2,2'-methylene-bis(4,6-di-tert-butylphenyl)phosphate (R3) is likely to induce smaller spherulites than sodium benzoate (R2) in non-reinforced plastics [28, 29]. However, in the case of fibre-reinforced plastics, a more perfect crystalline structure (small spherulite sizes, homogeneous spherulite structure, possibly transcristalline interphase – as expected in the case of R3) increases the internal stresses in the fibre/matrix interface region and therefore the material brittleness [10]. These stresses concentrated around the fibres are easily revealed by means of a soda-ethanol chemical attack which induces material cracking due to stress relaxation (Figure 11).

Compared to the carbon black coloured formulation (R1), nucleating agents logically increase the crystallinity of the composites (Table 3). When the parts are moulded in the standard conditions (mould temperature at 150°C, Table 2), the local fibre contents are roughly similar whatever the additive may be. However, the PET matrix crystallizes much more

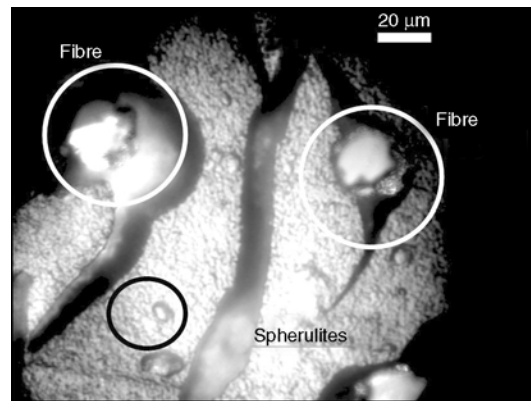


Figure 11. Fracture surface after chemical soda-ethanol attack for R3 formulation moulded at 150°C – Internal stresses at fibre/matrix interface

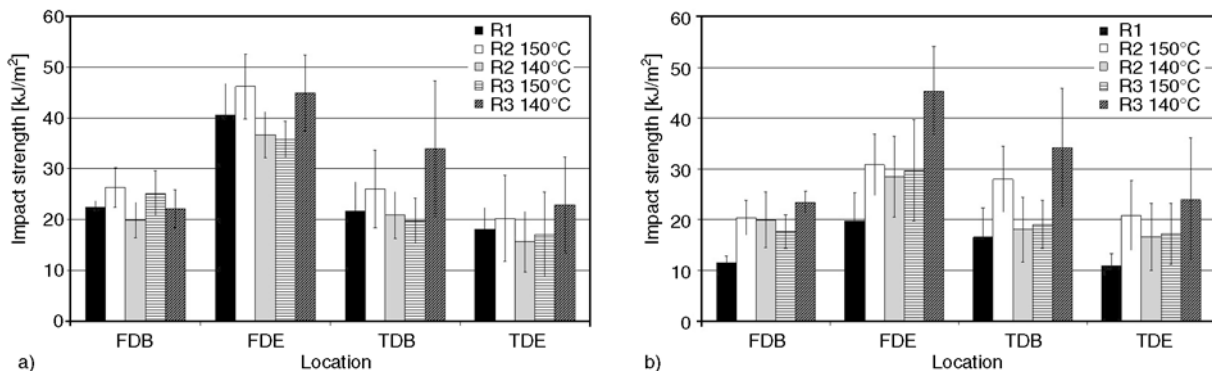
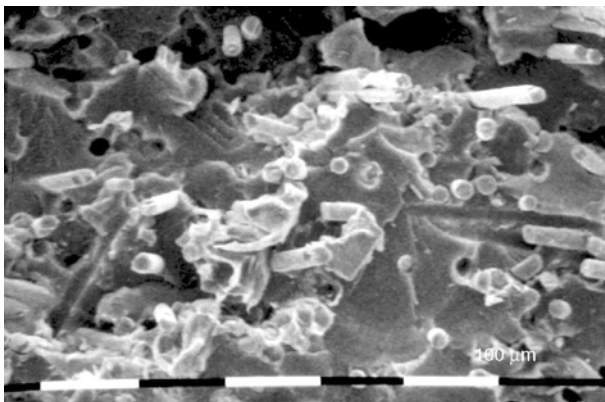


Figure 10. Unnotched flatwise (a) and notched edgewise (b) Charpy impact strengths in flow (FD) and transverse directions (TD) at beginning (B) and end (E) of the part – Effect of nucleating agent type (R2, R3) and mould temperature compared to black coloured (R1) PET/30 wt% LGF

easily when sodium benzoate (R2) is added as a nucleating agent. Compared to the additive-free reference material (R0), which is characterised by important microstructure variations between the beginning and the end of the plate, the parts are more homogeneous in terms of both fibre contents and degrees of crystallinity. Apart from the previously mentioned fluidisation effect of carbon black, such a limitation of the fibre segregation phenomenon may be also ascribed to another effect. In the case of the nucleating agent containing formulations (R2 and R3), the fibres or portions of fibres frozen in the solid layer during cavity filling may be more numerous due to the quicker crystallization kinetics induced by nucleating agents (the feeding of the molten layer with broken or pulled-out fibres being less in that case).

### 3.2.2. Influence of mould temperature

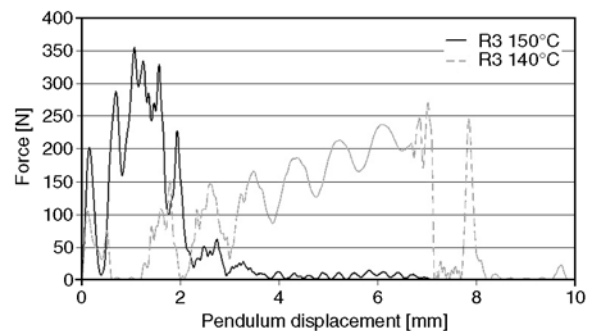
A decrease of the mould temperature (from 150 to 140°C) generally allows getting better impact properties when using sodium 2,2'-methylene-bis(4,6-di-tert-butylphenyl)phosphate nucleating agent (R3), if one excepts the peculiar behaviour of the FBD sample in the unnotched test configuration for which no relevant explanation was found here. The impact strength globally reaches the same values as those of the additive-free reference material (R0) moulded at 150°C (Figure 5), and is higher than (or if not at least almost equivalent to) that of the other carbon black coloured materials (R1, R2) moulded at 150°C (Figure 10). In contrary, the formulation based on sodium benzoate (R2) shows a clear property loss when moulded at lower temperature.



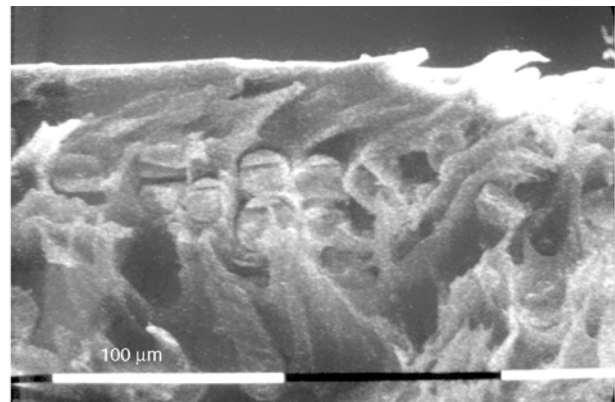
a)

The change of mould temperature can induce modifications of flow mechanisms, and consequently of the composite microstructure. In the case of sodium benzoate based formulation (R2), there is no change of fibre content distribution within the part; however a noticeable decrease of the degree of crystallinity is observed (Table 3). In the case of sodium 2,2'-methylene-bis(4,6-di-tert-butylphenyl)phosphate based formulation (R3), a longitudinal fibre segregation similar to the one already observed with the additive-free reference material (R0) is noticed with fibre accumulations at the end of the part, the degree of crystallinity remaining roughly the same whatever the mould temperature is.

The fracture behaviour also changes with the mould temperature. Hence, the fracture of the sodium phosphate based formulation (R3) is brittle at a mould temperature of 150°C (Figure 12a), whereas an important plastic deformation and breakage of fibres are observed at a mould temperature of 140°C (Figure 12b). The plastic strain observed for the sodium phosphate based formulation (R3) at

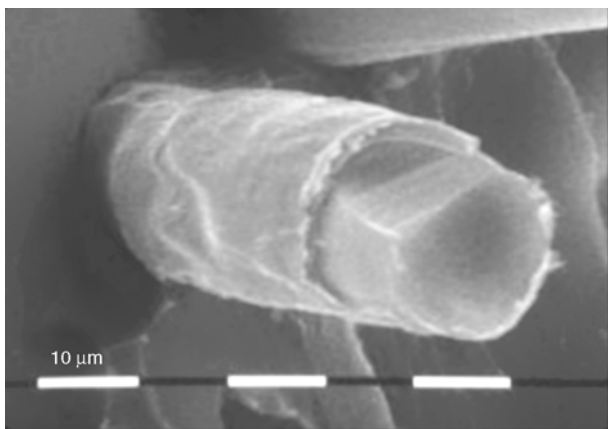


**Figure 13.** Force/displacement curve recorded during notched edgewise Charpy impact test in flow direction at the end of the part – Effect of moulding temperature for R3 formulation



b)

**Figure 12.** Fracture surfaces after unnotched flatwise Charpy impact test for R3 formulation – Effect of mould temperature (a) 150°C (b) 140°C



**Figure 14.** Fracture surface after notched edgewise Charpy impact test at plate beginning for R3 formulations moulded at 150°C – Transcrystalline structure

140°C may explain the impact strength strong increase whatever the test configuration is. It results in a ductility increase as shown on the force/displacement curves (Figure 13). This may be ascribed to a modification of the crystalline area between the fibres and the matrix (as defined by Vu-Khanh and Denault [20]), and especially the formation of a transcrystalline zone. Such a transcrystalline layer was evidenced for the R3 formulation only (Figure 14). For this reference only, a significant increase of the cooling rate was evidenced by the drop of internal pressure within the mould during the holding stage of the injection-moulding cycle.

#### 4. Conclusions

The presence of additives in the polymer matrix (pigments/dyes, nucleating agents) induces microstructure modification of long glass fibre reinforced PET composites that in turn causes variations in impact performances.

When carbon black is used as the only additive for a black colouring purpose, it generates an impact property loss whatever the loading mode is (unnotched flatwise impact or notched edgewise impact). A mechanical fluidisation during the filling stage of the mould modifies the local fibre content and thus is likely to influence fibre orientation, forming a more isotropic and homogeneous part. Due to its thermal conductivity, this additive increases the cooling rate of the part, thus decreasing the degree of crystallinity. However, it also acts as filler that significantly weakens the composite during impact loading.

The nucleating agents allow reducing mould temperatures, thus also cycle times by increasing the cooling rates. However their effect on impact strengths may be favourable or detrimental depending on their chemical nature and the processing temperatures. Moreover their effect is possibly hindered by the simultaneous addition of carbon black, which is very common in automotive applications. Adding carbon black or nucleating agents into the polymer matrix of PET long fibre thermoplastics induces perturbation of both the rheology of the melt flow in the cavity and the cooling kinetic of the parts that act together on the fibre distribution during the filling stage and on the composite degrees of crystallinity. The mechanical performances are consequently highly affected.

#### Acknowledgements

Thanks are due to the European Union (FEDER, European Funds for Regional Development) for contributing to the funding of equipment.

#### References

- [1] Markarian J.: Automotive composites. *Plastics Engineering*, **67**, 22–29 (2011).
- [2] Monteil J-B.: European automotive industry's demand for reinforced plastics on the rise. *JEC Composites Magazine*, **28**, 24–25 (2006).
- [3] Thomason J. L., Vlug M. A.: Influence of fibre length and concentration on the properties of glass fibre-reinforced polypropylene: 1. Tensile and flexural modulus. *Composites Part A: Applied Science and Manufacturing*, **27**, 477–484 (1996). DOI: [10.1016/1359-835X\(95\)00065-A](https://doi.org/10.1016/1359-835X(95)00065-A)
- [4] Thomason J. L., Groenewoud W. M.: The influence of fibre length and concentration on the properties of glass fibre reinforced polypropylene: 2. Thermal properties. *Composites Part A: Applied Science and Manufacturing*, **27**, 555–565 (1996). DOI: [10.1016/1359-835X\(96\)00016-4](https://doi.org/10.1016/1359-835X(96)00016-4)
- [5] Thomason J. L., Vlug M. A., Schipper G., Krikor H. G. L. T.: Influence of fibre length and concentration on the properties of glass fibre-reinforced polypropylene: Part 3. Strength and strain at failure. *Composites Part A: Applied Science and Manufacturing*, **27**, 1075–1084 (1996). DOI: [10.1016/1359-835X\(96\)00066-8](https://doi.org/10.1016/1359-835X(96)00066-8)
- [6] Thomason J. L., Vlug M. A.: Influence of fibre length and concentration on the properties of glass fibre-reinforced polypropylene: 4. Impact properties. *Composites Part A: Applied Science and Manufacturing*, **28**, 277–288 (1997). DOI: [10.1016/S1359-835X\(96\)00127-3](https://doi.org/10.1016/S1359-835X(96)00127-3)

- [7] Thomason J. L.: The influence of fibre length and concentration on the properties of glass fibre reinforced polypropylene. 5. Injection moulded long and short fibre PP. *Composites Part A: Applied Science and Manufacturing*, **33**, 1641–1652 (2002).  
DOI: [10.1016/S1359-835X\(02\)00179-3](https://doi.org/10.1016/S1359-835X(02)00179-3)
- [8] Thomason J. L.: The influence of fibre length and concentration on the properties of glass fibre reinforced polypropylene. 6. The properties of injection moulded long fibre PP at high fibre content. *Composites Part A: Applied Science and Manufacturing*, **36**, 995–1003 (2005).  
DOI: [10.1016/j.compositesa.2004.11.004](https://doi.org/10.1016/j.compositesa.2004.11.004)
- [9] Thomason J. L.: The influence of fibre length and concentration on the properties of glass fibre reinforced polypropylene: 7. Interface strength and fibre strain in injection moulded long fibre PP at high fibre content. *Composites Part A: Applied Science and Manufacturing*, **38**, 210–216 (2007).  
DOI: [10.1016/j.compositesa.2006.01.007](https://doi.org/10.1016/j.compositesa.2006.01.007)
- [10] Lafranche E., Krawczak P., Ciolczyk J. P., Maugey J.: Injection moulding of long glass fibre reinforced polyamide 6-6: Guidelines to improve flexural properties. *Express Polymer Letters*, **1**, 456–466 (2007).  
DOI: [10.3144/expresspolymlett.2007.64](https://doi.org/10.3144/expresspolymlett.2007.64)
- [11] Lafranche E., Krawczak P., Ciolczyk J-P., Maugey P.: Injection moulding of long glass fiber reinforced polyamide 66: Processing conditions/microstructure/flexural properties relationship. *Advances in Polymer Technology*, **24**, 114–131 (2005).  
DOI: [10.1002/adv.20035](https://doi.org/10.1002/adv.20035)
- [12] Thomason J. L.: The influence of fibre length, diameter and concentration on the strength and strain to failure of glass fibre-reinforced polyamide 6,6. *Composites Part A: Applied Science and Manufacturing*, **39**, 1618–1624 (2008).  
DOI: [10.1016/j.compositesa.2008.07.002](https://doi.org/10.1016/j.compositesa.2008.07.002)
- [13] Thomason J. L.: The influence of fibre length, diameter and concentration on the modulus of glass fibre reinforced polyamide 6,6. *Composites Part A: Applied Science and Manufacturing*, **39**, 1732–1738 (2008).  
DOI: [10.1016/j.compositesa.2008.08.001](https://doi.org/10.1016/j.compositesa.2008.08.001)
- [14] Thomason J. L.: The influence of fibre properties on the properties of glass-fibre-reinforced polyamide 6,6. *Journal of Composite Materials*, **34**, 158–172 (2000).  
DOI: [10.1177/002199830003400205](https://doi.org/10.1177/002199830003400205)
- [15] Thomason J. L.: Micromechanical parameters from macromechanical measurements on glass reinforced polyamide 6,6. *Composite Science and Technology*, **61**, 2007–2016 (2001).  
DOI: [10.1016/S0266-3538\(01\)00062-8](https://doi.org/10.1016/S0266-3538(01)00062-8)
- [16] Thomason J. L.: The influence of fibre length, diameter and concentration on the impact performance of long glass-fibre reinforced polyamide 6,6. *Composites Part A*, **40**, 114–124 (2009).  
DOI: [10.1016/j.compositesa.2008.10.013](https://doi.org/10.1016/j.compositesa.2008.10.013)
- [17] Cilleruelo L., Lafranche E., Krawczak P., Pardo P., Lucas P.: Injection moulding of long-glass-fibre-reinforced poly(ethylene terephthalate): Influence of processing conditions on flexural and impact strengths. *Polymers and Polymer Composites*, **16**, 577–588 (2008).
- [18] Karger-Kocsis J., Harmia T., Czigány T.: Comparison of the fracture and failure behavior of polypropylene composites reinforced by long glass fibers and by glass mats. *Composites Science and Technology*, **54**, 287–298 (1995).  
DOI: [10.1016/0266-3538\(95\)00068-2](https://doi.org/10.1016/0266-3538(95)00068-2)
- [19] Karger-Kocsis J.: Instrumented impact fracture and related failure behavior in short- and long-glass-fiber-reinforced polypropylene. *Composites Science and Technology*, **48**, 273–283 (1993).  
DOI: [10.1016/0266-3538\(93\)90144-6](https://doi.org/10.1016/0266-3538(93)90144-6)
- [20] Vu-Khanh T., Denault J.: Fracture behaviour of long fibre reinforced thermoplastics. *Journal of Materials Science*, **29**, 5732–5738 (1994).  
DOI: [10.1007/BF00349973](https://doi.org/10.1007/BF00349973)
- [21] Bartus S. D., Vaidya U. K.: Performance of long fiber reinforced thermoplastics subjected to transverse intermediate velocity blunt object impact. *Composite Structures*, **67**, 263–277 (2005).  
DOI: [10.1016/j.compstruct.2004.07.023](https://doi.org/10.1016/j.compstruct.2004.07.023)
- [22] Skourlis T. P., Mehta S. R., Chassapis C., Manoochehri S.: Impact fracture behavior of injection molded long glass fiber reinforced polypropylene. *Polymer Engineering and Science*, **38**, 79–89 (1998).  
DOI: [10.1002/pen.10167](https://doi.org/10.1002/pen.10167)
- [23] Mucha M., Marszalek J., Firdych A.: Crystallization of isotactic polypropylene containing carbon black as a filler. *Polymer*, **41**, 4137–4142 (2000).  
DOI: [10.1016/S0032-3861\(99\)00706-5](https://doi.org/10.1016/S0032-3861(99)00706-5)
- [24] Dekoninck J. M., Legras R., Mercier J. P.: Nucleation of poly(ethylene terephthalate) by sodium compounds: A unique mechanism. *Polymer*, **30**, 910–913 (1989).  
DOI: [10.1016/0032-3861\(89\)90191-2](https://doi.org/10.1016/0032-3861(89)90191-2)
- [25] Garcia D.: Heterogeneous nucleation of poly(ethylene terephthalate). *Journal of Polymer Science: Polymer Physics Edition*, **22**, 2063–2072 (1984).  
DOI: [10.1002/pol.1984.180221206](https://doi.org/10.1002/pol.1984.180221206)
- [26] Ye M., Wang X., Huang W., Hu J., Bu H.: Fast crystallization of poly(ethylene terephthalate). *Journal of Thermal Analysis and Calorimetry*, **46**, 905–920 (1996).  
DOI: [10.1007/BF01983610](https://doi.org/10.1007/BF01983610)
- [27] Jiang X. L., Luo S. J., Sun K., Chen X. D.: Effect of nucleating agents on crystallization kinetics of PET. *Express Polymer Letters*, **1**, 245–251 (2007).  
DOI: [10.3144/expresspolymlett.2007.37](https://doi.org/10.3144/expresspolymlett.2007.37)
- [28] Botkin J. H., Dunski N., Maeder D.: Improving molding productivity and enhancing mechanical properties of polypropylene with nucleating agents. in ‘SPE Automotive TPO Global Conference 2002 Conference Proceedings, Dearborn, USA’ 163–170 (2002).

- [29] Zhang Y-F., Xin Z.: Effects of substituted aromatic heterocyclic phosphate salts on properties, crystallization, and melting behaviors of isotactic polypropylene. *Journal of Applied Polymer Science*, **100**, 4868–4874 (2006).  
DOI: [10.1002/app.23209](https://doi.org/10.1002/app.23209)
- [30] Pompe G., Mäder E.: Experimental detection of a transcrystalline interphase in glass-fibre/polypropylene composites. *Composites Science and Technology*, **60**, 2159–2167 (2000).  
DOI: [10.1016/S0266-3538\(00\)00120-2](https://doi.org/10.1016/S0266-3538(00)00120-2)
- [31] Zhang X., Xie F., Pen Z., Zhang Y., Zhang Y., Zhou W.: Effect of nucleating agent on the structure and properties of polypropylene/poly(ethylene–octene) blends. *European Polymer Journal*, **38**, 1–6 (2002).  
DOI: [10.1016/S0014-3057\(01\)00182-3](https://doi.org/10.1016/S0014-3057(01)00182-3)
- [32] Salazar A., Rico A., Rodríguez S., Navarro J. M., Rodríguez J.: Relating fracture behavior to spherulite size in controlled-rheology polypropylene. *Polymer Engineering and Science*, **52**, 805–813 (2011).  
DOI: [10.1002/pen.22145](https://doi.org/10.1002/pen.22145)
- [33] Xu T., Yu J., Jin Z.: Effects of crystalline morphology on the impact behavior of polypropylene. *Materials and Design*, **22**, 27–31 (2001).  
DOI: [10.1016/S0261-3069\(00\)00033-9](https://doi.org/10.1016/S0261-3069(00)00033-9)
- [34] Taguchi G., Konishi S., Wu Y.: Taguchi methods: Research and development. *Quality Engineering Series*, Vol. 1. ASI Press, Dearborn (1992).
- [35] Arnoult M., Dargent E., Mano J. F.: Mobile amorphous phase fragility in semi-crystalline polymers: Comparison of PET and PLLA. *Polymer*, **48**, 1012–1019 (2007).  
DOI: [10.1016/j.polymer.2006.12.053](https://doi.org/10.1016/j.polymer.2006.12.053)
- [36] Unal H.: Morphology and mechanical properties of composites based on polyamide 6 and mineral additives. *Materials and Design*, **25**, 483–487 (2004).  
DOI: [10.1016/j.matdes.2004.01.007](https://doi.org/10.1016/j.matdes.2004.01.007)
- [37] Mareri P., Bastide S., Binda N., Crespy A.: Mechanical behaviour of polypropylene composites containing fine mineral filler: Effect of filler surface treatment. *Composites Science and Technology*, **58**, 747–752 (1998).  
DOI: [10.1016/S0266-3538\(97\)00156-5](https://doi.org/10.1016/S0266-3538(97)00156-5)
- [38] Tancrez J. P.: Study of the brittleness of injection moulded short-glass-fibre-reinforced polypropylene matrix composites (in French). PhD Thesis, University of Lille I – Ecole des Mines de Douai (1994).



# Carboxyl-terminated butadiene-acrylonitrile-toughened epoxy/carboxyl-modified carbon nanotube nanocomposites: Thermal and mechanical properties

Y. T. Wang<sup>1</sup>, C. S. Wang<sup>1</sup>, H. Y. Yin<sup>1</sup>, L. L. Wang<sup>1</sup>, H. F. Xie<sup>1\*</sup>, R. S. Cheng<sup>1,2</sup>

<sup>1</sup>Key Laboratory for Mesoscopic Chemistry of Ministry of Education, Department of Polymer Science and Engineering, School of Chemistry and Chemical Engineering, Nanjing University, 210093 Nanjing, China

<sup>2</sup>College of Material Science and Engineering, South China University of Technology, 510640 Guangzhou, China

Received 21 January 2012; accepted in revised form 26 March 2012

**Abstract.** Carboxyl-modified multi-walled carbon nanotubes (MWCNT–COOHs) as nanofillers were incorporated into diglycidyl ether of bisphenol A (DGEBA) toughened with carboxyl-terminated butadiene-acrylonitrile (CTBN). The carboxyl functional carbon nanotubes were characterized by Fourier-transform infrared spectroscopy and thermogravimetric analysis. Furthermore, cure kinetics, glass transition temperature ( $T_g$ ), mechanical properties, thermal stability and morphology of DGEBA/CTBN/MWCNT–COOHs nanocomposites were investigated by differential scanning calorimetry (DSC), dynamic mechanical analysis (DMA), universal test machine, thermogravimetric analysis and scanning electron microscopy (SEM). DSC kinetic studies showed that the addition of MWCNT–COOHs accelerated the curing reaction of the rubber-toughened epoxy resin. DMA results revealed that  $T_g$  of rubber-toughened epoxy nanocomposites lowered with MWCNT–COOH contents. The tensile strength, elongation at break, flexural strength and flexural modulus of DGEBA/CTBN/MWCNT–COOHs nanocomposites were increased at lower MWCNT–COOH concentration. A homogenous dispersion of nanocomposites at lower MWCNT–COOH concentration was observed by SEM.

**Keywords:** nanocomposites, thermal properties, thermosetting resin, carbon nanotubes, epoxy resin

## 1. Introduction

Epoxy resins are widely used as coatings, adhesives, insulating materials and matrices for fibrous composites for their rigidity, high temperature performance, chemical resistance and adhesive properties. However, the inherent brittleness due to the high crosslinking density becomes one of the biggest troubles in advanced application use in industries. Therefore, great efforts have been exerted in the modifications of epoxy resins for further improvement of multifunctional properties [1, 2].

Presently, reactive liquid rubber, thermoplastics, interpenetrating polymer networks (IPNs), thermotropic liquid crystal and nanofillers are used to

toughen epoxies for improving properties of epoxy networks. The elastomeric toughening is the most frequently used and widely accepted among these methods. Recently, Tripathi and Srivastava [1, 3] reported that a two-phase morphology was observed and the best balance of mechanical properties were achieved with a concentration of carboxyl-terminated butadiene-acrylonitrile (CTBN) ranging between 15 and 20 phr (part per hundred resin) in the cured epoxy resin. Varley [4] effectively toughened the diglycidyl ether of bisphenol A (DGEBA) by both epoxy-terminated aliphatic polyesters and CTBN with a great improvement of the fracture properties whereas the addition of aminopropyl-ter-

\*Corresponding author, e-mail: [hfxie@nju.edu.cn](mailto:hfxie@nju.edu.cn)

minated siloxane showed no improvement due to the poor dispersion. Kishi *et al.* [5] found that though the CTBN/DGEBA/DDM (diamino diphenyl methane) resins indicated high damping performance and high adhesive strength to aluminum substrates, there was always loss of strength of the materials accompanied with the improvement of toughness. The work of Ratna and Banthia [6] showed that the tensile strength and flexural strength of the epoxy resins modified by carboxyl terminated poly(2-ethylhexyl acrylate) decreased rapidly with increase of the rubber. Similar observations have been reported by other authors [7, 8].

Carbon nanotubes (CNTs) and carbon nanofibers (CNFs) are considered as reinforcement for polymer matrix because of the remarkable physical, chemical and electrical properties with small dimensions and high aspect ratios [9–12]. In order to transfer the outstanding properties to the modified epoxy, functionalization of pristine CNTs is essential for getting strong interfacial bonding and proper dispersion [13–17]. Gojny *et al.* [18] studied the mechanical properties of epoxy matrix composites with different types of CNTs which exhibited an improved strength, stiffness and fracture toughness. Liu and Wagner [19] reported two epoxy matrices with widely different mechanical properties both were reinforced by CNTs. Sui *et al.* [20] reported that epoxy resins were reinforced and toughened more effectively by CNTs than CNFs [21]. However, the enhancement was not as significant as expected. Recently, Hsieh *et al.* [22] proved that the addition of CNTs increased the modulus of the epoxy. The measured fracture energy was increased, from 133 to 223 J/m<sup>2</sup> with the addition of 0.5 wt% of nanotubes.

To our knowledge, few studies have been carried out on the influence of CNTs on the rubber-tough-

ened epoxy [23]. In present paper, CTBN and carboxyl-functionalized multi-walled carbon nanotubes (MWCNTs) were first reacted with DGEBA to form adducts, which were then cured with a flexible curing agent, Jeffamine to further increase the toughness of the epoxy. The dynamic cure kinetics, thermal stability, glass transition temperature, mechanical properties, and morphology of carboxyl-functionalized MWCNT/epoxy/rubber nanocomposites were studied.

## 2. Experimental

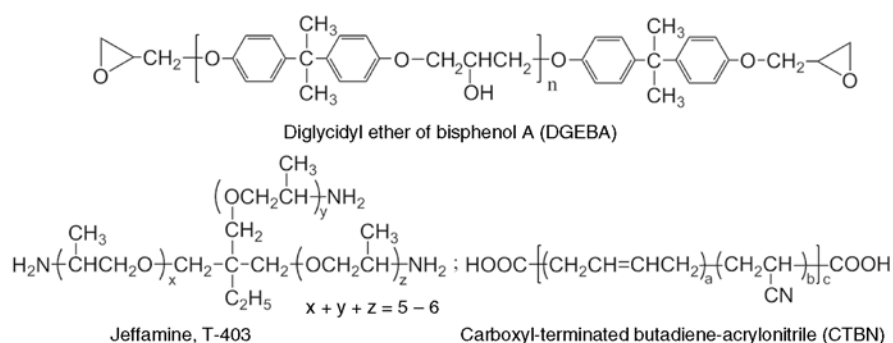
### 2.1. Materials

The epoxy resin used in this study was DGEBA, E51, with an epoxide equivalent weight of 196 g/eq, from Wuxi Resin Factory (Wuxi, China). The curing agent was Jeffamine, T403, from Huntsman Corporation (Texas, USA). The elastomeric toughener used was a liquid CTBN rubber with an acrylonitrile content of 30–35%, from Lanzhou Petrochemical Company (Lanzhou, China). Chemical structures of DGEBA, Jeffamine and CTBN are showed in Figure 1. MWCNTs with diameters of 40–60 nm and lengths of 5–15 μm were supplied by Shenzhen Nanotech Port Co. Ltd. (Shenzhen, China).

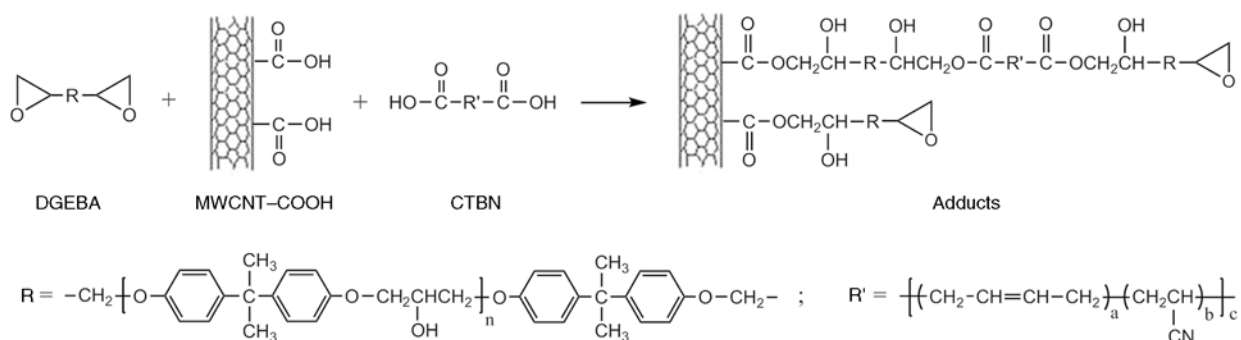
### 2.2. Sample preparation

3 g MWCNTs were mixed with 100 mL nitric acid with a concentration of 5 mol/L and sonicated for 1 h in water bath, then the suspension reacted at 130°C for 10 h. After they were washed with deionized water until the filtrate reached a pH value of *ca.* 6–7, MWCNT–COOHs were dried in vacuum at 60°C for 3 day and collected then.

DGEBA and 15 phr (part per hundred resin) CTBN were mixed, then MWCNT–COOHs were added, the mixture was reacted for 2 h with mechanical



**Figure 1.** Chemical structures of DGEBA, Jeffamine and CTBN



**Figure 2.** The reaction scheme between carboxyl groups in CTBN and MWCNT-COOHs and epoxy groups in DGEBA

stirring at 145°C and then sonicated for 1.5 h at 30°C, during which adducts could be formed among DGEBA, CTBN and MWCNT-COOHs, as shown in Figure 2. The adducts were placed in an oil bath at 75°C, then a stoichiometric amount of Jeffamine was added with continuous mechanical stirring until a homogeneous mixture was observed. Several DSC aluminum pans were filled with the reaction mixture. The mixtures (*ca.* 10 mg) were then cooled and stored in a freezer until they were required for the DSC measurements. Other mixtures were immediately poured into polytetrafluoroethylene molds and cured for 2 h at 80°C and 3 h at 125°C. DGEBA/CTBN/MWCNT-COOHs nanocomposites with 0, 0.5, 1, 2 wt% MWCNT-COOHs noted as MWCNT0, MWCNT0.5, MWCNT1 and MWCNT2, respectively.

### 2.3. Characterization

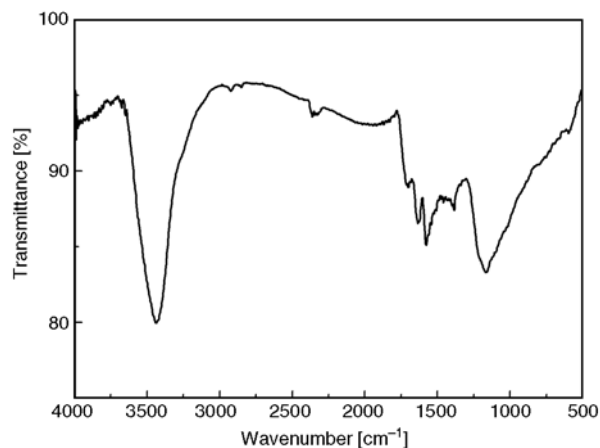
The FT-IR spectrum of MWCNT-COOHs was recorded on a Nicolet Avatar 360 FT-IR spectrometer (Thermo Scientific, USA) in the wavelength range of 4000–400  $\text{cm}^{-1}$ , at a resolution of 4  $\text{cm}^{-1}$ . MWCNT-COOHs were pressed into a pellet together with potassium bromide (KBr) powder. Studies on dynamic curing kinetics of epoxy nanocomposites were performed on Pyris 1 DSC (Perkin-Elmer, USA) under an argon flow of 20 mL/min. The samples for kinetic analysis were heated up from 50 to 300°C at heating rates of 5, 10, 15 and 20°C/min, respectively. The  $T_g$ s of the cured samples were tested using dynamic mechanical analysis (DMA; DMA + 450, 01 dB-Mettravib, France). The measurements were taken under tension mode from –80 to 140°C with a frequency of 1 Hz at a heating rate of 2°C/min. All mechanical tests were performed on an Instron 4466 universal material tester (Instron, USA) at room temperature. The tensile tests were

measured according to ASTM D638 at 5 mm/min. For the flexural test, rectangular specimens were cut with dimensions of 100 × 10 × 5 mm according to ASTM-D790 and tested at a crosshead speed of 4 mm/min. Four specimens were tested in the mechanical measurements. TGA was performed at a Pyris 1 thermogravimetric analyzer (Perkin-Elmer, USA) with a heating rate of 20°C/min over a temperature range of 25–600°C under a nitrogen flow of 40 mL/min. Scanning electronic microscopy (SEM) images of the fracture surfaces were obtained on a Hitachi S-4800 field-emission scanning electronic microscope (Hitachi, Japan). The cured samples were fractured under liquid nitrogen, and then the fractured surfaces were vacuum-coated with a thin gold layer.

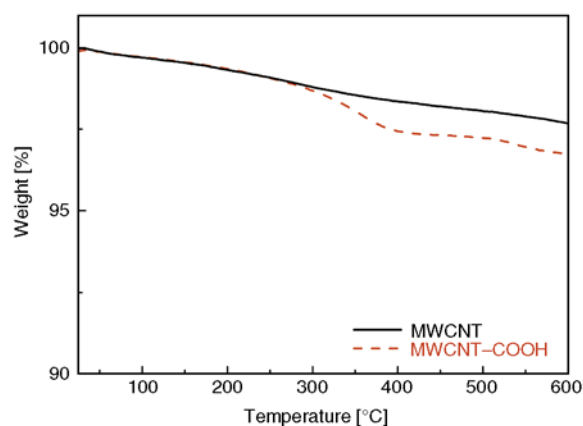
## 3. Results and discussion

### 3.1. Characterization of carboxyl-modified carbon nanotubes

Figure 3 shows the FT-IR spectrum of MWCNT-COOHs. The peaks at around 3435 and 1714  $\text{cm}^{-1}$  could be respectively assigned to the O–H stretching vibrations and C=O stretching vibrations, so it



**Figure 3.** FT-IR spectrum of carboxyl-modified MWCNTs



**Figure 4.** TGA curves of MWCNT and carboxyl-modified MWCNTs

is clear that MWCNTs were successfully modified with the introduction of the carboxyl functionalities. Besides, the peaks observed at around 1579 and 1384  $\text{cm}^{-1}$  should be ascribed to the carbonic C–C stretch bonds [24].

The samples of MWCNTs and MWCNT-COOHs were studied with TGA (as shown in Figure 4). Compared with the pristine MWCNTs, carboxyl-functionalized MWCNTs displayed more weight loss between 300 and 600°C. This weight loss results from the losing of carboxyl groups on the surface of MWCNTs.

### 3.2. Cure behaviors

DSC is often used to study the effect of nanofillers on the cure behaviors of epoxy resin [11, 16, 25–27]. In present work, dynamic kinetic studies based on Kissinger and Flynn-Wall-Ozawa (FWO) models [26–28] were utilized to investigate the DGEBA/CTBN/MWCNT-COOHs nanocomposites. Both

models do not require prior knowledge of the reaction mechanism.

According to the Kissinger model [28], the activation energy can be obtained from Equation (1):

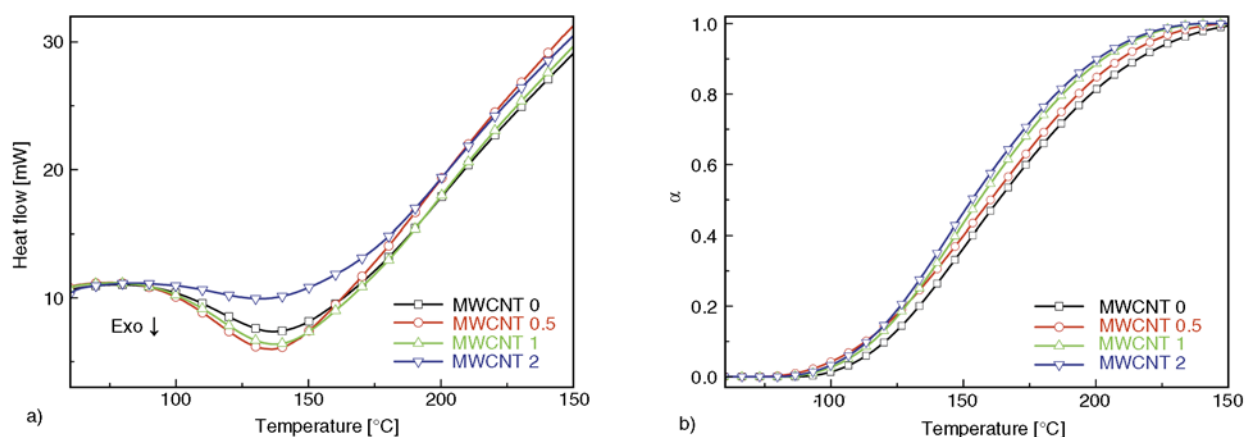
$$\frac{d[\ln(\beta/T_p^2)]}{d(1/T_p)} = -\frac{E_\alpha}{R} \quad (1)$$

where  $T_p$  is the peak exothermal temperature,  $\beta$  is the constant heating rate,  $E_\alpha$  is the activation energy of the reaction, and  $R$  is the universal gas constant. The value of  $E_\alpha$  can be obtained by plotting  $\ln(T_p^2)$  versus  $1/T_p$ .

The Flynn-Wall-Ozawa (FWO) model [29, 30] yields a simple relationship between the activation energy  $E_\alpha$ , the heating rate  $\beta$ , and the peak exothermal temperature  $T_p$ , giving the activation energy as shown by Equation (2):

$$\log\beta = A - 0.457\frac{E_\alpha}{RT_p} \quad (2)$$

Figure 5 shows DSC thermograms from dynamic heating experiments and conversion versus temperature curves for DGEBA/CTBN/MWCNT-COOHs nanocomposites conducted at a heating rate of 20°C/min, while the conversion is defined as the ratio of the heat generated up to time  $t$  to the total heat of the reaction. Clearly, the samples with MWCNT-COOHs reacted faster than the rubber-only toughened epoxy (MWCNT 0). Furthermore, the reaction rate of MWCNT-COOHs nanocomposites increased with the rise of MWCNT-COOH contents. The initial reaction temperature ( $T_i$ ), exothermal peak temperature ( $T_p$ ) and heat of curing ( $\Delta H$ ) of DGEBA/CTBN/MWCNT-COOHs nanocomposites at differ-



**Figure 5.** DSC curves (a) and relationship between conversion ( $\alpha$ ) and temperature (b) for DGEBA/CTBN/MWCNT-COOHs nanocomposites at a heating rate of 20°C/min

ent heating rates are listed in Table 1. It is observed that both  $T_i$  and  $T_p$  decrease with the increase of MWCNT–COOH contents, indicating that MWCNT–COOHs act as catalysts and facilitate the curing reaction and the catalytic effect increases with the MWCNT–COOH contents.

By applying the Kissinger and FWO methods, activation energies can be obtained from the slope of

**Table 1.** The initial temperature, peak temperature and heat of curing for DGEBA/CTBN/MWCNT–COOHs nanocomposites

MWCNT–COOH [wt%]	Heating rate [°C/min]	$T_i$ [°C]	$T_p$ [°C]	$\Delta H$ [J/g]
0	5	80.500	107.200	315.255
	10	81.100	121.200	313.661
	15	83.100	130.100	318.466
	20	87.700	137.200	315.875
0.5	5	78.600	103.300	313.303
	10	79.300	120.800	306.760
	15	81.200	127.300	313.697
	20	85.100	135.100	310.983
1	5	75.300	102.600	312.719
	10	78.000	118.100	308.868
	15	80.500	126.600	305.528
	20	81.200	134.500	299.297
2	5	73.400	100.000	310.877
	10	76.700	116.000	296.764
	15	78.600	125.300	291.877
	20	79.900	132.500	284.224

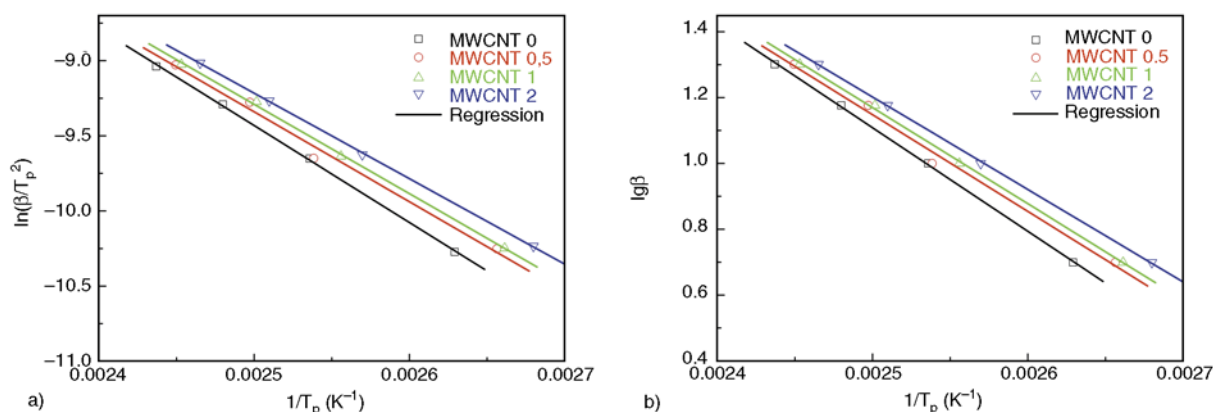
**Table 2.** Activation energies of DGEBA/CTBN/MWCNT–COOHs nanocomposites

MWCNT–COOH [wt%]	$E_a$ [kJ/mol]	
	Kissinger	FWO
0	53.6	57.2
0.5	49.7	53.4
1	49.4	53.1
2	47.3	51.1

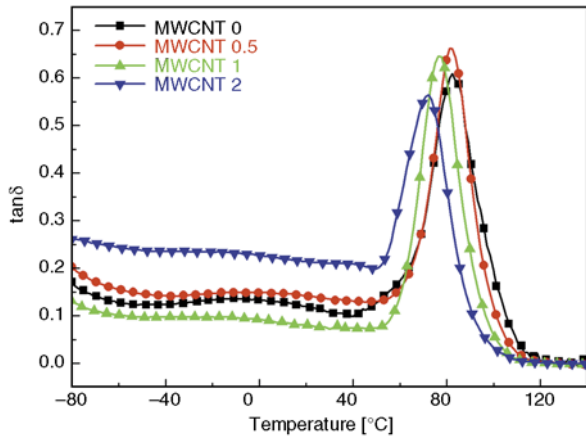
the lines as presented in Figure 6. Linear relationships were obtained, confirming the validity of the models for the systems under study. Table 2 summarizes the results obtained from the dynamic kinetic analysis. The activation energies calculated from the two models were in close agreement. It is obvious that  $E_a$  of nanocomposites decreased with the increasing of MWCNT–COOH contents. A decrease in activation energy implies that less energy of the reacting resin components is required and indicates an accelerating effect. This suggests that the addition of carboxyl-MWCNTs into rubber-toughened epoxy resin facilitates the curing reaction, which is consistent with the results of other workers [31, 32]. The high thermal conductivity of the MWCNTs is considered to be the origin for the decrease in activation energy [31].

### 3.3. Glass transition temperature ( $T_g$ )

The loss tangent ( $\tan \delta$ ) as a function of temperature is shown in Figure 7. The temperature at which the  $\tan \delta$  is maximum is defined as  $T_g$ . The  $T_g$  of MWCNT 0.5 was almost equal to that of MWCNT 0, but it decreased markedly with the increasing of MWCNT–COOH contents. One possibility is that the addition of MWCNT–COOHs causes over-stoichiometric active hydrogen which can react with the epoxy groups, since it is well known that the stoichiometric ratio of curing agent to epoxide group leads to maximum  $T_g$  [33]. Similar results were reported in fluorinated MWCNTs/epoxy nanocomposites [34]. The introduction of MWCNT–COOHs would increase the viscosity of the mixture significantly, resulting in the rapid decrease of the cure degree in the diffusion-controlled stage. Thus,  $T_g$ s of the MWCNT–COOHs nanocomposites are expected



**Figure 6.** Relationship between  $\ln(\beta/T_p^2)$  and  $1/T_p$  (a) and between  $\ln \beta$  (b) and  $1/T_p$  (b) for DGEBA/CTBN/MWCNT–COOHs nanocomposites

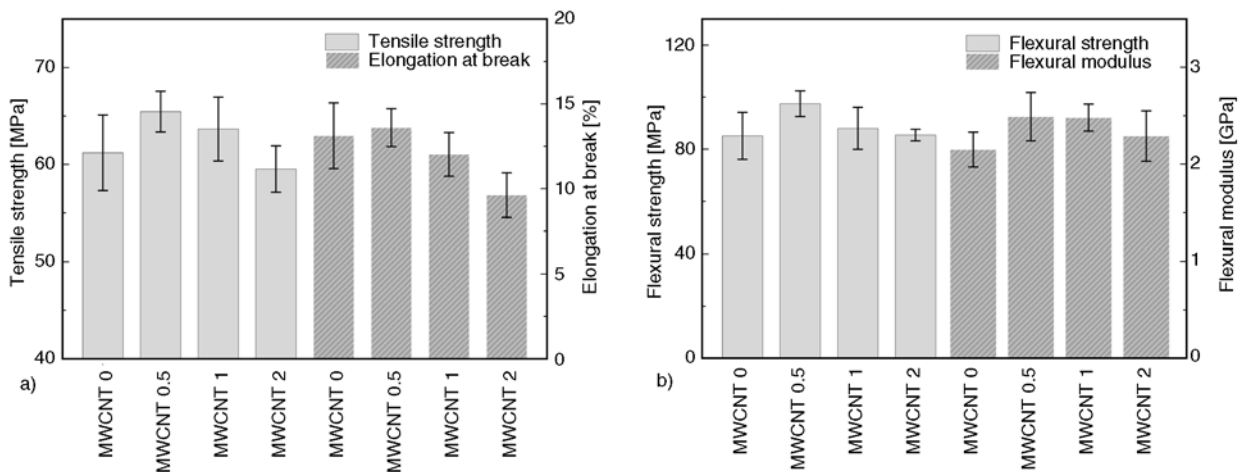


**Figure 7.** Temperature dependence of  $\tan\delta$  for the CTBN-toughened epoxy and DGEBA/CTBN/MWCNT–COOHs nanocomposites

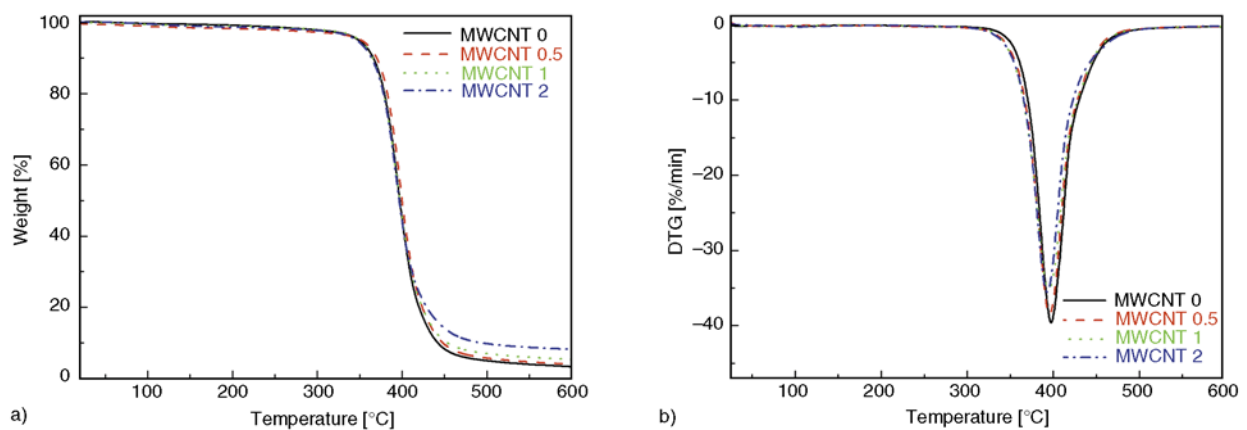
to be lower than the rubber-only toughened one (MWCNT 0). Though MWCNTs could limit the mobility of the polymer chains to elevate the  $T_g$ s of the composites, the effect was counterbalanced by the poor dispersion of MWCNT–COOHs for MWCNT 1 and MWCNT 2 [26].

### 3.4. Mechanical properties

To evaluate the effects of MWCNT–COOHs on the mechanical properties of the toughened epoxy, tensile tests and flexural tests were performed, as showed in Figure 8a and 8b, respectively. It is known that the addition of rubber inevitably decreases the tensile strength of epoxy resin. With the addition of MWCNT–COOHs, tensile strengths of MWCNT 0.5 and MWCNT 1 and elongation at break of MWCNT 0.5 were greater than that of rubber-toughened epoxy (MWCNT 0). Moreover, with the increasing of MWCNT–COOH content, the tensile strength and elongation at break decreased gradually. As shown in Figure 8b, with the incorporation of CTBN, the addition of MWCNT–COOHs increased the flexural strength modulus of rubber-toughened epoxy. Furthermore, the flexural strength and modulus for DGEBA/CTBN/MWCNT–COOHs nanocomposites decreased with the increasing of MWCNT–COOH contents. The mechanical properties of nanocomposites depend on the dispersion of



**Figure 8.** Tensile strengths and elongations at break (a) and flexural strengths and flexural moduli (b) for the CTBN-toughened epoxy and DGEBA/CTBN/MWCNT–COOHs nanocomposites

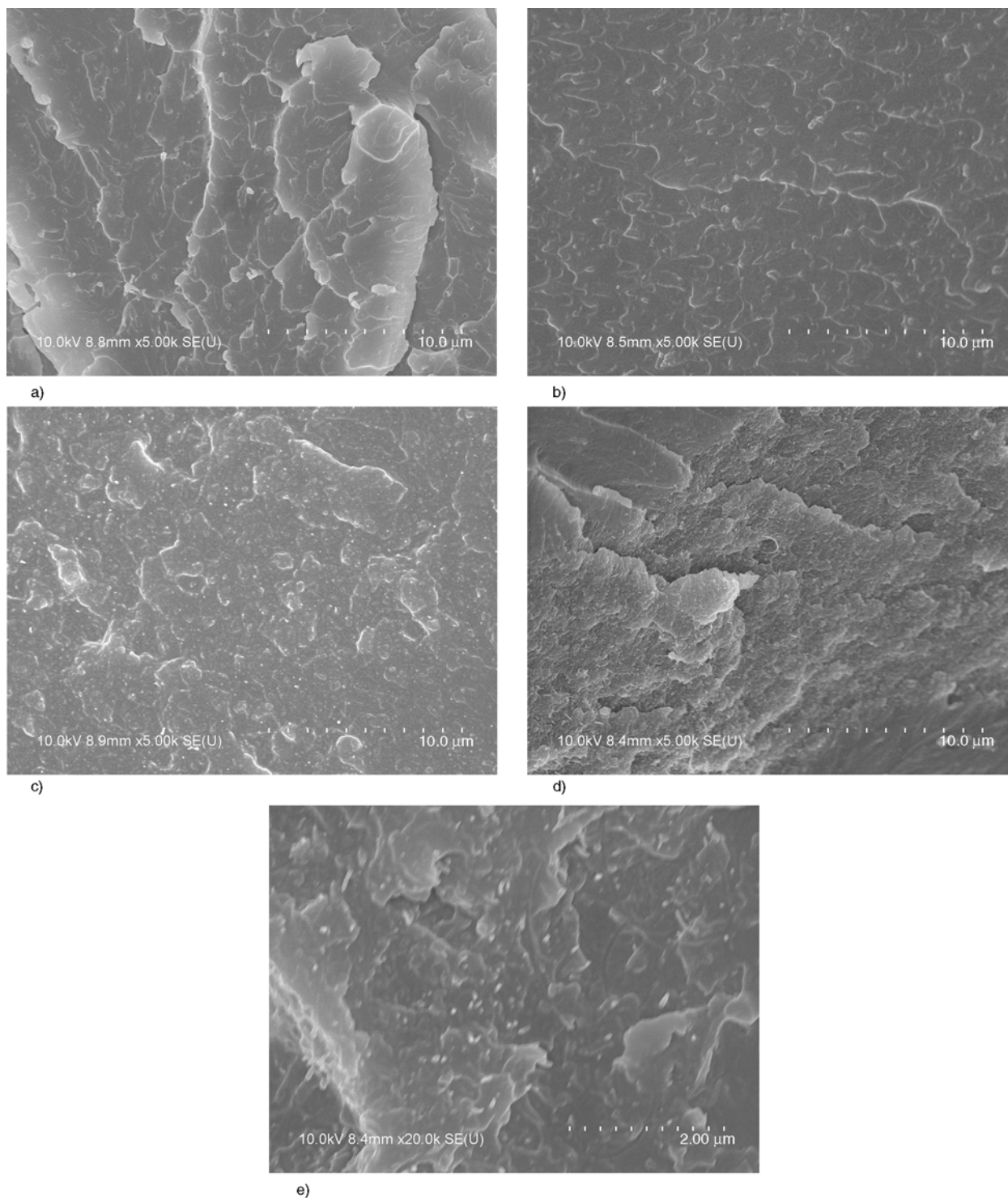


**Figure 9.** TGA (a) and DTG (b) curves for DGEBA/CTBN/MWCNT–COOHs nanocomposites

carbon nanotubes in the polymer matrix and the interaction between nanotubes and polymers [35, 36]. In other words, more homogeneous dispersion and better interface between the nanotubes and the epoxy matrix result in better mechanical properties. For MWCNT–COOHs, good dispersion can be achieved at lower concentration. However, higher nanotube concentration will cause higher viscosity

**Table 3.** TGA and DTG results for DGEBA/CTBN/MWCNT–COOH nanocomposites

MWCNT [wt%]	IDT [°C]	T <sub>max</sub> [°C]	Residue at 600°C [%]
0	349	397	3.2
0.5	352	395	3.9
1	350	395	5.3
2	347	393	8.2



**Figure 10.** SEM images of cryo-fracture surfaces for (a) MWCNT 0, (b) MWCNT 0.5, (c) MWCNT 1 and (d) MWCNT 2; (e) high magnification image of (d)

and agglomerates with poor dispersion. The agglomerates present in poorly dispersed nanocomposites cause cracks to initiate and propagate easily. The generated cracks reduce the strength of the rubber-toughened epoxy nanocomposites.

### 3.5. Thermal stability

TGA and DTG curves for DGEBA/CTBN nanocomposites with different concentration of MWCNT–COOHs are presented in Figure 9. The initial decomposition temperature (IDT) which is set as the temperature at 5% weight loss, maximum rate of degradation temperatures ( $T_{max}$ ) and residue at 600°C are summarized in Table 3. The negligible changes of IDTs and  $T_{max}$ s illustrate that MWCNT–COOHs do not affect the thermal stabilities of the resin matrices. The residues of the nanocomposites at 600°C increased with the growing concentration of MWCNT–COOHs. In Figure 9b, every curve showed a single peak at about 396°C, proving the strong interaction of the epoxy with CTBN and MWCNT–COOHs.

### 3.6. Morphology

SEM images of cryo-fracture surfaces for rubber-toughened epoxy and its MWCNT–COOHs nanocomposites are shown in Figure 10. Two-phase morphology was easily observed in MWCNT0 (Figure 10a). MWCNT–COOHs dispersed relatively uniformly at a low concentration in the CTBN-toughened epoxy system (MWCNT0.5, Figure 10b), while agglomerates were increased in both size and amount with the increasing of the concentration of MWCNT–COOHs, as shown in Figure 10c and 10d. These results indicate the existence of strong interfacial bonding between 0.5 wt% MWCNT–COOHs and CTBN-toughened epoxy in the nanocomposites. In contrast, 2 wt% MWCNT–COOHs have weak interfacial interactions with the rubber toughened matrix because of the agglomeration of MWCNT–COOHs. Many MWCNT–COOHs were pulled out from the fractured surface (Figure 10e), which phenomena have also been observed in our previous reports [17]. The poor dispersion of MWCNTs had significant influence on the glass transition temperature and mechanical properties of nanocomposites as discussed above.

## 4. Conclusions

Carboxyl-modified multi-walled carbon nanotubes were successfully prepared by treating MWCNTs with acid and then incorporated into the epoxy/CTBN matrix. Dynamic kinetic analysis showed that the activation energy of rubber-toughened epoxy nanocomposites decreased with the increasing of MWCNT–COOH contents, indicating carboxyl-functionalized carbon nanotubes accelerate the cure reactions of the rubber-toughened epoxy system. The incorporation of MWCNT–COOHs improved mechanical properties of the CTBN-toughened epoxy systems, whereas the improvement was not linear with the concentration of MWCNT–COOHs. The maximum tensile and flexural properties were obtained at MWCNT–COOH concentration of 0.5 wt% with uniform dispersion. Nevertheless, at higher concentrations, MWCNT–COOHs agglomerated in the viscous epoxy/CTBN system and resulted in the decreasing of mechanical properties. The glass transition temperature of rubber-toughened nanocomposites decreased with the increasing MWCNT–COOH contents.

## Acknowledgements

The authors would like to thank the Fundamental Research Funds for the Central Universities (1106020514) for financial support.

## References

- [1] Tripathi G., Srivastava D.: Studies on the physico-mechanical and thermal characteristics of blends of DGEBA epoxy, 3,4 epoxy cyclohexylmethyl, 3',4'-epoxycyclohexane carboxylate and carboxyl terminated butadiene co-acrylonitrile (CTBN). *Materials Science and Engineering: A*, **496**, 483–493 (2008). DOI: [10.1016/j.msea.2008.06.035](https://doi.org/10.1016/j.msea.2008.06.035)
- [2] Thomas R., Ding Y., He Y., Yang L., Moldenaers P., Yang W., Czigany T., Thomas S.: Miscibility, morphology, thermal, and mechanical properties of a DGEBA based epoxy resin toughened with a liquid rubber. *Polymer*, **49**, 278–294 (2008). DOI: [10.1016/j.polymer.2007.11.030](https://doi.org/10.1016/j.polymer.2007.11.030)
- [3] Tripathi G., Srivastava D.: Effect of carboxyl-terminated poly(butadiene-co-acrylonitrile) (CTBN) concentration on thermal and mechanical properties of binary blends of diglycidyl ether of bisphenol-A (DGEBA) epoxy resin. *Materials Science and Engineering: A*, **443**, 262–269 (2007). DOI: [10.1016/j.msea.2006.09.031](https://doi.org/10.1016/j.msea.2006.09.031)



- [4] Varley R. J.: Toughening of epoxy resin systems using low-viscosity additives. *Polymer International*, **53**, 78–84 (2004).  
DOI: [10.1002/pi.1321](https://doi.org/10.1002/pi.1321)
- [5] Kishi H., Nagao A., Kobayashi Y., Matsuda S., Asami T., Murakami A.: Carboxyl-terminated butadiene acrylonitrile rubber/epoxy polymer alloys as damping adhesives and energy absorbable resins. *Journal of Applied Polymer Science*, **105**, 1817–1824 (2007).  
DOI: [10.1002/app.26189](https://doi.org/10.1002/app.26189)
- [6] Ratna D., Bantia A. K.: Toughened epoxy adhesive modified with acrylate based liquid rubber. *Polymer International*, **49**, 281–287 (2000).  
DOI: [10.1002/\(SICI\)1097-0126\(200003\)49:3<281::AID-PI353>3.0.CO;2-F](https://doi.org/10.1002/(SICI)1097-0126(200003)49:3<281::AID-PI353>3.0.CO;2-F)
- [7] Day R. J., Lovell P. A., Wazzan A. A.: Thermal and mechanical characterization of epoxy resins toughened using preformed particles. *Polymer International*, **50**, 849–857 (2001).  
DOI: [10.1002/pi.690](https://doi.org/10.1002/pi.690)
- [8] Du J., Thouless M. D., Yee A. F.: Development of a process zone in rubber-modified epoxy polymers. *International Journal of Fracture*, **92**, 271–285 (1998).  
DOI: [10.1023/A:1007530801531](https://doi.org/10.1023/A:1007530801531)
- [9] Bokobza L.: Multiwall carbon nanotube elastomeric composites: A review. *Polymer*, **48**, 4907–4920 (2007).  
DOI: [10.1016/j.polymer.2007.06.046](https://doi.org/10.1016/j.polymer.2007.06.046)
- [10] Byrne M. T., Gun'ko Y. K.: Recent advances in research on carbon nanotube–polymer composites. *Advanced Materials*, **22**, 1672–1688 (2010).  
DOI: [10.1002/adma.200901545](https://doi.org/10.1002/adma.200901545)
- [11] Xie H., Liu B., Sun Q., Yuan Z., Shen J., Cheng R.: Cure kinetic study of carbon nanofibers/epoxy composites by isothermal DSC. *Journal of Applied Polymer Science*, **96**, 329–335 (2005).  
DOI: [10.1002/app.21415](https://doi.org/10.1002/app.21415)
- [12] Xie H., Liu B., Yang H., Wang Z., Shen J., Cheng R.: Thermal characterization of carbon-nanofiber-reinforced tetraglycidyl-4,4'-diaminodiphenylmethane/4,4'-diaminodiphenylsulfone epoxy composites. *Journal of Applied Polymer Science*, **100**, 295–298 (2006).  
DOI: [10.1002/app.23106](https://doi.org/10.1002/app.23106)
- [13] Ma P. C., Kim J.-K., Tang B. Z.: Effects of silane functionalization on the properties of carbon nanotube/epoxy nanocomposites. *Composites Science and Technology*, **67**, 2965–2972 (2007).  
DOI: [10.1016/j.compscitech.2007.05.006](https://doi.org/10.1016/j.compscitech.2007.05.006)
- [14] Wang S., Liang Z., Liu T., Wang B., Zhang C.: Effective amino-functionalization of carbon nanotubes for reinforcing epoxy polymer composites. *Nanotechnology*, **17**, 1551–1557 (2006).  
DOI: [10.1088/0957-4484/17/6/003](https://doi.org/10.1088/0957-4484/17/6/003)
- [15] Xie H., Liu C., Yuan Z., Yang H., Wang Z. L., Cheng R.: Thermoanalytical studies of high performance epoxy/carbon nanotube composites. *Acta Polymerica Sinica*, **4**, 332–336 (2008).  
DOI: [10.3724/SP.J.1105.2008.00332](https://doi.org/10.3724/SP.J.1105.2008.00332)
- [16] Xie H., Liu B., Yuan Z., Shen J., Cheng R.: Cure kinetics of carbon nanotube/tetrafunctional epoxy nanocomposites by isothermal differential scanning calorimetry. *Journal of Polymer Science Part B: Polymer Physics*, **42**, 3701–3712 (2004).  
DOI: [10.1002/polb.20220](https://doi.org/10.1002/polb.20220)
- [17] Wang C., Chen X., Xie H., Cheng R.: Effects of carbon nanotube diameter and functionality on the properties of soy polyol-based polyurethane. *Composites Part A: Applied Science and Manufacturing*, **42**, 1620–1626 (2011).  
DOI: [10.1016/j.compositesa.2011.07.010](https://doi.org/10.1016/j.compositesa.2011.07.010)
- [18] Gojny F. H., Wichmann M. H. G., Fiedler B., Schulte K.: Influence of different carbon nanotubes on the mechanical properties of epoxy matrix composites – A comparative study. *Composites Science and Technology*, **65**, 2300–2313 (2005).  
DOI: [10.1016/j.compscitech.2005.04.021](https://doi.org/10.1016/j.compscitech.2005.04.021)
- [19] Liu L., Wagner H. D.: Rubbery and glassy epoxy resins reinforced with carbon nanotubes. *Composites Science and Technology*, **65**, 1861–1868 (2005).  
DOI: [10.1016/j.compscitech.2005.04.002](https://doi.org/10.1016/j.compscitech.2005.04.002)
- [20] Sui G., Zhong W. H., Liu M. C., Wu P. H.: Enhancing mechanical properties of an epoxy resin using ‘liquid nano-reinforcements’. *Materials Science and Engineering: A*, **512**, 139–142 (2009).  
DOI: [10.1016/j.msea.2009.01.023](https://doi.org/10.1016/j.msea.2009.01.023)
- [21] Sun L., Warren G., O'Reilly J. Y., Everett W. N., Lee S. M., Davis D., Lagoudas D., Sue H.-J.: Mechanical properties of surface-functionalized SWCNT/epoxy composites. *Carbon*, **46**, 320–328 (2008).  
DOI: [10.1016/j.carbon.2007.11.051](https://doi.org/10.1016/j.carbon.2007.11.051)
- [22] Hsieh T. H., Kinloch A. J., Taylor A. C., Kinloch I. A.: The effect of carbon nanotubes on the fracture toughness and fatigue performance of a thermosetting epoxy polymer. *Journal of Materials Science*, **46**, 7525–7535 (2011).  
DOI: [10.1007/s10853-011-5724-0](https://doi.org/10.1007/s10853-011-5724-0)
- [23] Salinas-Ruiz M. d. M., Skordos A. A., Partridge I. K.: Rubber-toughened epoxy loaded with carbon nanotubes: structure-property relationships. *Journal of Materials Science*, **45**, 2633–2639 (2010).  
DOI: [10.1007/s10853-010-4241-x](https://doi.org/10.1007/s10853-010-4241-x)
- [24] Kim Y. J., Shin T. S., Choi H. D., Kwon J. H., Chung Y.-C., Yoon H. G.: Electrical conductivity of chemically modified multiwalled carbon nanotube/epoxy composites. *Carbon*, **43**, 23–30 (2005).  
DOI: [10.1016/j.carbon.2004.08.015](https://doi.org/10.1016/j.carbon.2004.08.015)
- [25] Qiu S. L., Wang C. S., Wang Y. T., Liu C. G., Chen X. Y., Xie H. F., Huang Y. A., Cheng R. S.: Effects of graphene oxides on the cure behaviors of a tetrafunctional epoxy resin. *Express Polymer Letters*, **5**, 809–818 (2011).  
DOI: [10.3144/expresspolymlett.2011.79](https://doi.org/10.3144/expresspolymlett.2011.79)

- [26] Allaoui A., El Bounia N.: How carbon nanotubes affect the cure kinetics and glass transition temperature of their epoxy composites? – A review. *Express Polymer Letters*, **3**, 588–594 (2009).  
DOI: [10.3144/expresspolymlett.2009.73](https://doi.org/10.3144/expresspolymlett.2009.73)
- [27] Zhou T., Wang X., Liu X. H., Lai J. Z.: Effect of silane treatment of carboxylic-functionalized multi-walled carbon nanotubes on the thermal properties of epoxy nanocomposites. *Express Polymer Letters*, **4**, 217–226 (2010).  
DOI: [10.3144/expresspolymlett.2010.28](https://doi.org/10.3144/expresspolymlett.2010.28)
- [28] Kissinger H. E.: Reaction kinetics in differential thermal analysis. *Analytical Chemistry*, **29**, 1702–1706 (1957).  
DOI: [10.1021/ac60131a045](https://doi.org/10.1021/ac60131a045)
- [29] Flynn J. H., Wall L. A.: A quick, direct method for the determination of activation energy from thermogravimetric data. *Journal of Polymer Science Part B: Polymer Letters*, **4**, 323–328 (1966).  
DOI: [10.1002/pol.1966.110040504](https://doi.org/10.1002/pol.1966.110040504)
- [30] Ozawa T.: Kinetic analysis of derivative curves in thermal analysis. *Journal of Thermal Analysis*, **2**, 301–324 (1970).  
DOI: [10.1007/BF01911411](https://doi.org/10.1007/BF01911411)
- [31] Chen S., Hsu S-H., Wu M-C., Su W. F.: Kinetics studies on the accelerated curing of liquid crystalline epoxy resin/multiwalled carbon nanotube nanocomposites. *Journal of Polymer Science Part B: Polymer Physics*, **49**, 301–309 (2011).  
DOI: [10.1002/polb.22179](https://doi.org/10.1002/polb.22179)
- [32] Choi W. S., Shanmugaraj A. M., Ryu S. H.: Study on the effect of phenol anchored multiwall carbon nanotube on the curing kinetics of epoxy/Novolac resins. *Thermochimica Acta*, **506**, 77–81 (2010).  
DOI: [10.1016/j.tca.2010.04.019](https://doi.org/10.1016/j.tca.2010.04.019)
- [33] Gupta V. B., Drzal L. T., Lee C. Y-C., Rich M. J.: The temperature-dependence of some mechanical properties of a cured epoxy resin system. *Polymer Engineering and Science*, **25**, 812–823 (1985).  
DOI: [10.1002/pen.760251305](https://doi.org/10.1002/pen.760251305)
- [34] Miyagawa H., Rich M. J., Drzal L. T.: Thermo-physical properties of epoxy nanocomposites reinforced by carbon nanotubes and vapor grown carbon fibers. *Thermochimica Acta*, **442**, 67–73 (2006).  
DOI: [10.1016/j.tca.2006.01.016](https://doi.org/10.1016/j.tca.2006.01.016)
- [35] Tasis D., Tagmatarchis N., Bianco A., Prato M.: Chemistry of carbon nanotubes. *Chemical Review*, **106**, 1105–1136 (2006).  
DOI: [10.1021/cr050569o](https://doi.org/10.1021/cr050569o)
- [36] Song Y. S., Youn J. R.: Influence of dispersion states of carbon nanotubes on physical properties of epoxy nanocomposites. *Carbon*, **43**, 1378–1385 (2005).  
DOI: [10.1016/j.carbon.2005.01.007](https://doi.org/10.1016/j.carbon.2005.01.007)

# Facile synthesis of stereoregular carbon fiber precursor polymers by template assisted solid phase polymerization

G. Santhana Krishnan<sup>1\*</sup>, A. Burkanudeen<sup>2</sup>, N. Murali<sup>1</sup>, H. Phadnis<sup>3</sup>

<sup>1</sup>Materials Science Division, CSIR-National Aerospace Laboratories, 560017 Bangalore, India

<sup>2</sup>Post Graduate and Research Department of Chemistry, Jamal Mohammed College (Bharathidasan University), Tiruchirappalli, India

<sup>3</sup>Malvern-Aimil Application Laboratory, Naimex House, 560045 Bangalore, India

Received 8 February 2012; accepted in revised form 1 April 2012

**Abstract.** Predominantly isotactic stereoregular polyacrylonitrile copolymers (PAC) were prepared by solid phase polymerization techniques using hexagonal crystalline metal salts as template compounds. Stereoregular distributions of the prepared polymer were studied using high resolution <sup>13</sup>C nuclear magnetic resonance spectroscopy (<sup>13</sup>C NMR) spectra. The extent of isotacticity was directly determined from the peak intensity of the methine carbon (CH). The triad tacticity from the intensities of methine carbon peaks were examined by statistical methods. It was found that the PAC was predominantly isotactic in stereoregularity, and its sequence distribution obeys Bernoulli statistics. The optimum polymerization conditions ensuring isotactic content over 50% were disclosed experimentally. The chemical composition of PAC was confirmed with <sup>1</sup>H NMR data. The obtained polyacrylonitrile copolymers were also characterized for molecular parameters such as viscosity average molecular weight ( $M_v$ ), number average molecular weight ( $M_n$ ), weight average molecular weight ( $M_w$ ) and polydispersity index.

**Keywords:** polymer synthesis, polyacrylonitrile copolymer, NMR, stereoregularity, molecular weight distribution

## 1. Introduction

Carbon fibers generally have excellent mechanical properties such as high specific strength, specific modulus and are therefore widely used as strength modifiers for various reinforcing materials in aerospace applications, leisure goods, industrial materials and the like. Because of their superior mechanical properties, they have potential application for reducing automobile weight and are receiving increasing attention as an important advancement in solving the urgent problem of reducing carbon dioxide [1]. Acrylonitrile based copolymers (PAC) are an important class of precursors for high value carbon based materials, such as carbon fiber composites with high mechanical, thermal resistance and mesoporous carbon for use in photoelectronic

devices [2–5]. The essential requirements that PAC precursors for high performance carbon materials must possess are high molecular weight and well controlled molecular architecture [6–7].

Commercially high molecular weight PAC is prepared by conventional radical polymerization much of them aqueous slurry process using various water soluble free radical initiators [8]. Various parameters such as comonomers type, temperature, initiator systems, polymerization media etc., influence the properties of the final polymer [9]. It is difficult to control polydispersity index (typically,  $M_w/M_n < 3.0$ ). Similarly, it is difficult to control the chain architecture and microstructure of the polymer, specifically the stereoregularity of the polymer main chain described by its tacticity. The carbon

\*Corresponding author, e-mail: [santhana@nal.res.in](mailto:santhana@nal.res.in)

© BME-PT

fiber microstructure depends on the precursors and processing conditions. The stereoregularity as defined in terms of isotactic triad content of PAC often significantly affects the properties and functions of the polymers. Therefore, stereocontrol during polymerization is very important. More than three decades ago, Lewis acids were found to significantly influence the monomer reactivity during free-radical polymerization [10], and later, its stereochemistry [11]. However, the influence of Lewis acids on the stereochemistry during radical polymerization had not been reported. Isobe *et al.* [12] reported the efficient stereocontrol radical polymerization of acrylamides using Lewis acids as catalyst such as scandium trifluoromethanesulfonate and benzyl  $\alpha$ -methoxymethylacrylate. In general, stereospecific polymerization has been attained through an ionic or coordination process with metal based initiator as catalyst, which can provide a counteranionic or anionic species at the growing end. Conventional radical polymerization as applied to all vinyl monomers lacks a counter ionic species in the process, thereby resulting in the stereoirregular structures in the obtained polymers. Most commonly employed method for preparing high molecular weight PAC with well controlled stereoregularity is anionic polymerization, however this method yields polymer with branched structures which affects the process efficiency during the solution spinning process and stability of the polymer solution. Therefore, a method for facile synthesis of stereo controlled PAC continues to be subject of study. The stereoregularity of polyacrylonitrile was first determined by Matsuzaki *et al.* [13] from proton NMR spectra of deuterated polymers and established that the radically obtained polymer has an atactic structure.

Kamide and coworkers [14, 15] have synthesized highly isotactic PAN by gamma-ray irradiation assisted solid state polymerization on acrylonitrile-urea canal complex. Matsuzaki and coworkers [13, 16] and later Minagawa *et al.* [17] established that polyacrylonitrile obtained through X-ray or gamma-ray irradiation by solid phase polymerization of urea-canal complex has isotactic rich structure. Kamide *et al.* [18] have reported a polymer synthesis procedure for preparing high molecular weight, linear and high stereoregular polyacrylonitrile using anionic initiators including dialkylmagnesium. Considering the large scale requirements of PAC in

the manufacture of carbon fiber precursor polymers, these processes seem to be extravagant. The synthesis of a carbon fiber polymer precursor with high linearity, molecular weight and isotactic stereoregularity include the solid phase polymerization at low temperature ( $-75^{\circ}\text{C}$ ) using a urea/monomer clathrate complex reported by White [19]. However the unsaturated comonomers are absorbed on to crystalline materials, reducing the comonomer content in PAC. Therefore a robust synthesis procedure is a huge step toward development of a process for industrial scale production of high molecular weight PAC with isotacticity content more than 30 wt%.

PAC with high isotactic stereoregularity is preferred over atactic and syndiotactic contents in the manufacture of high tensile grade carbon fibers. One of the critical stages in the carbon fiber production is thermal oxidative stabilization reaction which involves intramolecular cyclization of adjacent nitrile groups in the structural chain. PAC with high isotactic content, wherein the nitrile groups are in a meso configuration is advantageous from a positional point of view for cyclization of the adjacent nitrile groups as compared to the other stereo structures [12]. Moreover, the dimensions of the hexagonal plane layer which forms during the subsequent carbonization or graphitization is larger than one achieved using conventional PAC with an atactic structure and thereby the strength of the resulting carbon fibers is increased.

Controlled radical polymerization (CRP), which has undergone significant progress in the past decade, enables the facile synthesis of polymers with controlled molar mass, narrow distribution of molecular weights, well defined architecture and site specific functionalities [20–26]. Among these CRP methods, atom transfer radical polymerization is perhaps the most desirable mechanism in terms of controllability. However, it is difficult to scale-up these processes due to the complex synthesis procedures involved. Moreover the physical properties of polymer depend on the primary structure of the polymer chain; therefore the polymer synthesis is designed to control the primary structure such as molecular mass of polymer, molecular mass distribution, branch structure and terminal structure or stereo structure [27–30]. The main objective of this study was the synthesis of well defined, linear, high stereo

regular PAC by applying a new polymerization technique.

In this research work, the PAC polymers such as poly(acrylonitrile-co-itaconic acid) and poly(acrylonitrile-co-acrylamide) were synthesized using template assisted solid phase polymerization technique and characterized for their molecular characteristics such as viscosity average molecular weight ( $M_v$ ), weight average molecular weight ( $M_w$ ), number average molecular weight ( $M_n$ ), molecular weight distribution and stereo regularity in terms of isotactic triad content [mm wt%]. This research has revealed that carbon fiber precursor polymer with high linearity, average molecular weight and isotacticity triad content greater than 50% could be successfully obtained through the solid phase polymerization assisted by template compounds.

## 2. Experimental

### 2.1. Materials

Synthesis grade acrylonitrile (AN) (110213), acrylamide (ACM) (79-06-1) and itaconic acid (ITA) (129204) [Sigma Aldrich Co. Ltd., Germany] were used in the polymer synthesis. Acrylonitrile was washed with sodium hydroxide solution of lower concentration 0.5 wt% and distilled at its boiling range just before polymerization to remove the inhibitor content. The hexagonal crystalline metal salts (anhydrous nickel chloride or magnesium chloride) (449172) [Sigma Aldrich Co. Ltd., Germany] was used as a template compound. Acrylamide and Itaconic acid were used as comonomers without further purification. Commercially available  $\alpha$ ,  $\alpha$  azoisobutyronitrile (AIBN) (78-67-1) [Sigma Aldrich Co. Ltd., Germany] was used as initiator after crystallization in methanol. Analytical grade dimethylsulphoxide (DMSO) (276855) [Sigma Aldrich Co. Ltd., Germany] was used for the measurements of polymer solution properties.

### 2.2. Synthesis of isotactic rich stereoregular poly(acrylonitrile-co-itaconic acid), poly(acrylonitrile-co-acrylamide)

The polymerization was carried out in a 500 mL three-necked round bottom flask, equipped with mechanical stirrer and a reflux condenser. The flask was bubbled with ultra pure  $N_2$  gas for 240 min. to ensure an oxygen-free atmosphere. The template compounds used in this polymer synthesis is a

hexagonal crystalline metal salt ( $NiCl_2$  or  $MgCl_2$ ). The size of the template metal crystalline particles was in the range of 25–50  $\mu m$ . The molar ratio of monomer and crystalline template compound was kept between 0.3 and 0.6, to give an optimal amount of monomer to coordinate with template compound. Then, a mixture of acrylonitrile (AN), acrylamide/itaconic acid, and (2–2.5 wt%) AIBN was added to the three-necked flask containing nickel chloride (N) at room temperature, and allowed to thoroughly absorb to prepare an AN/N complex. In order to enhance the interconnectivity between template compound and monomer mixture, the mixture was kept under a constant stirring. A solid-phase polymerization was carried out by keeping the above AN/N complex in a hot air circulating drier for 6 h at 70°C, and the final reaction mixture was poured into a pure methanol and precipitated. The white precipitate was filtered and washed several times with deionized water to remove the traces of metal salts and then dried under vacuum at 40°C for 24 h.

### 2.3. Characterization

#### FTIR

FTIR spectra (National Aerospace Laboratories, Bangalore, India) were recorded on a Shimadzu IR Affinity 1 model (Shimadzu Corp. Tokyo, Japan), the resolution being 2  $cm^{-1}$ , using KBr pellets (1 mg samples as 400 mg KBr). Typical conditions were as follows: wavenumber, 400–4000  $cm^{-1}$ , scanning, 32 counts; and purging gas,  $N_2$  (flow rate, 10 L/min). FTIR spectra were recorded using the KBr disk method.

#### NMR

The  $^1H$  NMR and  $^{13}C$  NMR (Bruker AMX-400, at Indian Institute of Science, Bangalore, India) spectra of the copolymers were recorded in DMSO using tetramethylsilane (TMS) as an internal standard [31]. Samples were concentrated in dimethyl sulphoxide about 5% (w/w) for  $^1H$  NMR and 5% (w/w) for  $^{13}C$  NMR and 2D NMR by using a 5 mm NMR tube at room temperature.  $^1H$  NMR spectra were acquired using 21738 data points, spectral width 6 kHz, broadening 0.3 Hz, pulse delay 1 s, pulse width 90°, and 32 scans.  $^{13}C$  NMR spectra were acquired using 24996 data points, spectral width 22 kHz, broadening 3 Hz, pulse delay 2 s, pulse width 90°, and 1024 scans. Nuclear

overhauser effect (NOE) was suppressed by gating the decouple sequence. Heteronuclear multiple quantum coherence (HMQC) was performed by using the standard Bruker pulse sequence with a pulse program. The spectrum was obtained with 256 increments in the F1 dimension and 1024 data points in the F2 dimension, with 200 scans and relaxation delay 1.5 s.

#### Solution viscometry

One hundred and fifty milligrams of a PAC sample dried by heat treatment at a temperature of 120°C for 2 hours and is dissolved at a temperature of 60°C into DMSO. The dropping time of the obtained solution between gauge marks is measured at an accuracy of 1/100 seconds using Ubbelohde viscometer at a temperature of 25°C. The measured dropping time is expressed as  $t$  [sec]. Similarly the dropping time of DMSO is expressed as  $t_0$ . Intrinsic viscosity ( $\eta$ ) was obtained according to the following Equation (1) [32]:

$$[\eta] = \{(1.44 \cdot \eta_{sp} + 1)\}^{1/2} - \frac{1}{0.36} \quad (1)$$

where  $\eta_{sp} = t/t_0 - 1$ . The viscosity average molecular weight of PAC was calculated by Equation (2) [33]:

$$[\eta] = 2.53 \cdot 10^{-4} [M_w]^{0.72} \quad (2)$$

#### Membrane osmometry

Osmotic pressure ( $\Pi$ ) of polymer solution was measured in the range of polymer concentration ( $C$ ) from 0.3 to 0.9 g/dL in DMSO at 60°C with Osmomat 090, Gonotec GmbH (Berlin, Germany) [34, 35]. Number average molecular weight ( $M_n$ ) was obtained as  $\Pi/C$  extrapolated to  $C = 0$  according to Equation (3):

$$\lim_{C \rightarrow 0} \Pi C^{-1} = RT(M_n^{-1}) + A_2 C \quad (3)$$

where  $R$  is gas constant.

#### Size exclusion chromatography –

##### Low angle laser light scattering (SEC-LALLS)

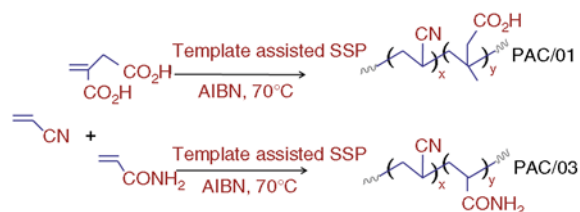
The SEC-LALLS instrument of Malvern Viscotek TDA 305 (Triple Detector Array, Malvern, United Kingdom) was used in this study [36]. The instru-

ment was operated at 50°C with DMSO as solvent. A flow rate of 1 mL/min and injection volume of 100  $\mu$ L was maintained. A concentration of ~4.0 wt% was maintained in all samples. Low angle laser light scattering (LALLS) instrument was used as a detector at a fixed wavelength of 633 nm. The molecular weight parameters were computed using SEC-LALLS data processing system. A set of polymethyl methacrylate (PMMA) standards of narrow molecular weight distribution (PolyCAL™, Viscotek, US) of molecular weight  $2.0 \cdot 10^4$ – $4.51 \cdot 10^5$  was used to calibrate the SEC-LALLS instrument. The carrier solvent was DMSO containing 0.05 m lithium bromide (LiBr) with a flow rate of 1 mL/min.

### 3. Results and discussion

This study primarily aimed to facilitate synthesis of a well defined, linear high molecular weight, and isotactic rich stereoregular PAC by thermal solid phase polymerization technique using hexagonal crystalline metal salts (Nickel chloride or Magnesium Chloride) with AIBN as initiator. The hexagonal crystalline metal salts adopt a layer structure on the macroscopic scale. Acrylonitrile monomers and unsaturated comonomers become enclosed between the crystalline metal compound layers with the polar groups orientated in the same direction to produce a regularly ordered arrangement. When particle size of the metallic compound is fine (<5  $\mu$ m), the PAC polymers were found to have lower molecular weight fractions. The general mechanism for the synthesis of PAC is represented in Figure 1. The Figure 2 shows the detailed representation of the various synthesis steps involved in the polymer synthesis.

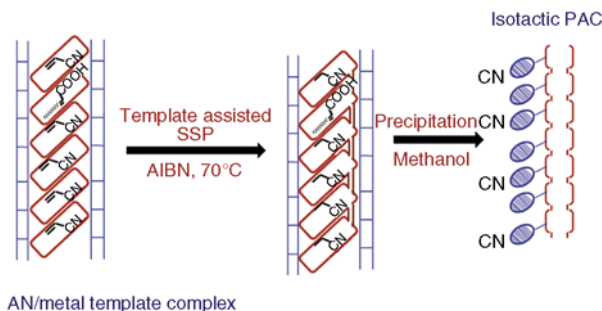
The chemical composition of the respective copolymers as determined from  $^1\text{H}$  NMR is given in Table 1. FTIR spectra of PAC are shown in Figure 3. The chemical structures of the copolymer are presented in Figure 4. The specific peak appearing at  $\sim 2244 \text{ cm}^{-1}$  in all spectra is associated with  $-\text{CN}$



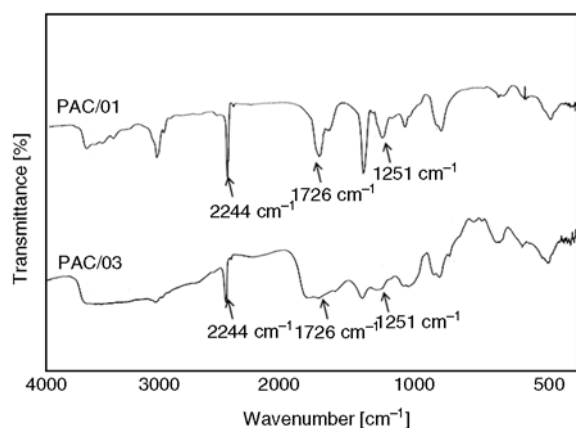
**Figure 1.** General mechanism for the synthesis of PAC

**Table 1.** Chemical composition of PAC

Sample code	Polymer composition [mol%]		AIBN [wt%]
PAC/01	AN(98.5)	ITA(1.5)	2.5
PAC/02	AN(98.5)	ITA(1.5)	2.0
PAC/03	AN(98.5)	ACM(1.5)	2.0
PAC/04	AN(98.5)	ACM(1.5)	2.5

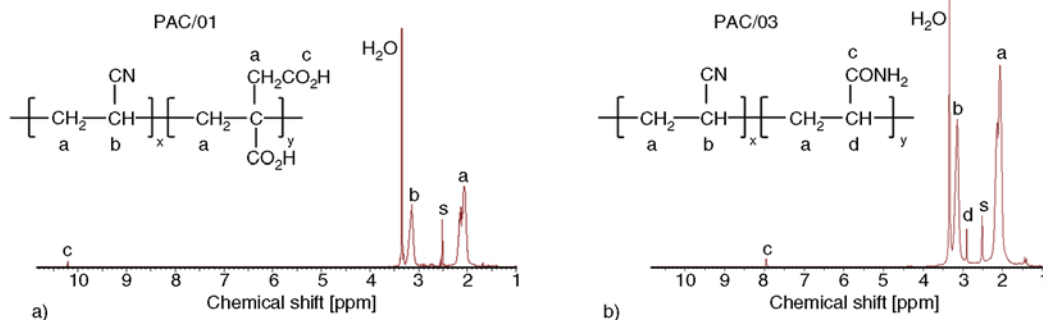


**Figure 2.** Schematic representation of the solid state polymerization process

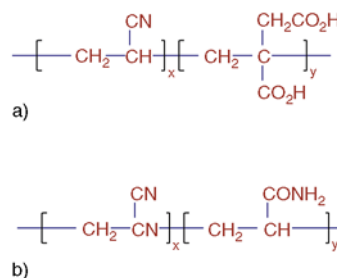


**Figure 3.** FTIR spectra of PAC/01 and PAC/03 copolymer sample

groups stretching vibration. The strong peak at  $\sim 1726\text{ cm}^{-1}$  appearing in both spectrum of the copolymers is associated with carboxyl groups (C=O) stretching vibration. The absorption peak at  $\sim 1251\text{ cm}^{-1}$  corresponds to C–O or C–N stretching vibration. These characteristics peaks in the spectra confirm the copolymer structures.



**Figure 5.** <sup>1</sup>H NMR spectra of (a) PAC/01 and (b) PAC/03 in DMSO-d<sub>6</sub> at 25°C



**Figure 4.** Chemical structures of PAC samples: (a) PAC/01 & PAC/02, and (b) PAC/03 & PAC/04

<sup>1</sup>H NMR spectra of PAC/01 and PAC/03 corresponding to poly[acrylonitrile-co-itaconic acid], poly[acrylonitrile-co-acrylamide] are shown in Figure 5a and 5b. It can be seen that, the spectrum was complicated due to spin-split and coupling of methylene protons from both acrylonitrile and itaconic acid monomers in Figure 5a. The signals of methylene protons (–CH<sub>2</sub>) from acrylonitrile and itaconic acid monomer units appeared at 2.1–2.2, and 2.3–2.4 ppm respectively. The signals corresponding to characteristic methine proton (–CH) and –COOH proton from itaconic acid were observed at 3.25 and 10.2 ppm respectively. The characteristic amide proton (–CONH<sub>2</sub>) from acrylamide corresponding to signal at 7.9 ppm. Compositions of the PAC/01–PAC/04 were determined by measuring the integrated areas of the resolved peaks corresponding to functional groups of respective monomers in <sup>1</sup>H NMR spectra.

The plot of reduced viscosity as a function of concentration of all samples in DMSO is shown in Figure 6. The viscosity average molecular weight of the PAC polymers determined using Equation (2) is given in Table 2. The osmotic pressure values of samples such as PAC/01–PAC/04 are measured in DMSO at 60°C. The plot of reduced osmotic pressure,  $\Pi/C$ , against concentration, C, of all the polymer solutions is shown in the Figure 7. In all cases

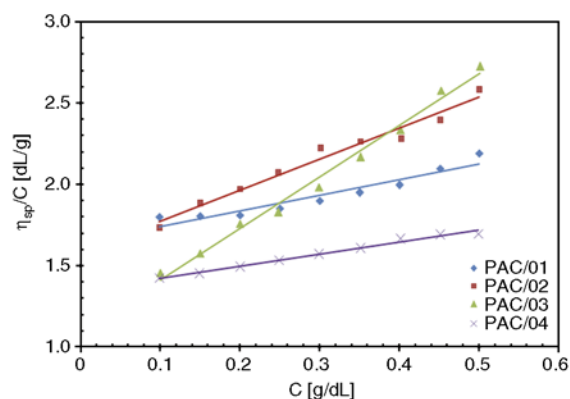
**Table 2.** Viscometry, osmometry, and SEC-LALLS results for different samples

Sample code	$[\eta]^a$ [g/dL]	$M_v^a \cdot 10^{-5}$ [g/mol]	$M_n^b \cdot 10^{-4}$ [g/mol]	$M_n^c \cdot 10^{-4}$ [g/mol]	$M_w^c \cdot 10^{-5}$ [g/mol]	$M_z^c \cdot 10^{-5}$ [g/mol]	$M_v^a/M_n^b$	$M_w/M_n^c$	$M_z/M_w^c$
PAC/01	2.24	3.06	14.3	11.8	2.57	4.31	2.13	2.168	1.68
PAC/02	1.43	1.64	7.8	4.7	1.17	2.25	2.10	2.503	1.92
PAC/03	1.70	3.26	10.2	7.21	1.73	3.18	3.20	2.411	1.84
PAC/04	1.90	2.44	11.2	7.49	1.60	3.17	3.03	2.147	1.99

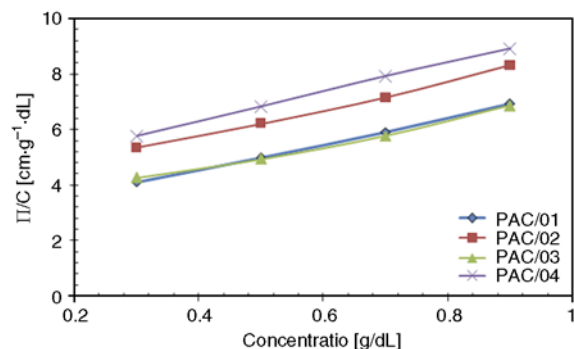
<sup>a</sup>By viscometry

<sup>b</sup>By membrane osmometry

<sup>c</sup>By SEC-LALLS



**Figure 6.** The plots of reduced viscosity as a function of concentration for PAC in DMSO at 30°C



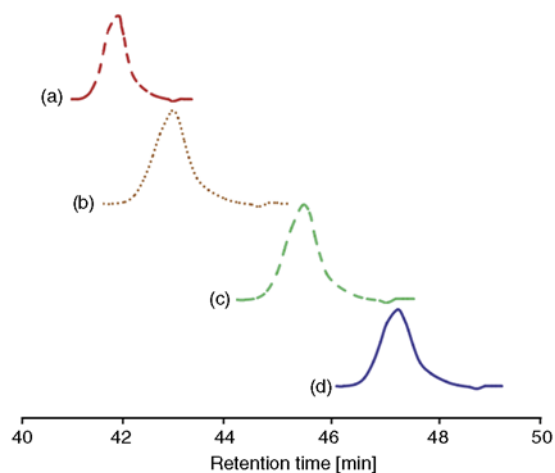
**Figure 7.** The plots of reduced osmotic pressure ( $\Pi/C$ ) against concentration  $C$  for PAC in DMSO at 60°C

linear relations are obtained when extrapolated to  $C = 0$  with a linear regression coefficient of 0.9945. From the extrapolation of the Van't Hoff plots, the value of number average molecular weight ( $M_n$ ) is determined. A set of four monodispersed polymethyl methacrylate (PMMA) standards corresponding to molecular weights from  $2.0 \cdot 10^4$ – $4.51 \cdot 10^5$  is used to calibrate SEC-LALLS instrument. A calibration data of retention volume-detector response corresponding to four different monodisperse (PMMA) standards is given in Table 3.

The molecular weight ( $M_n$ ,  $M_w$ ,  $M_z$ ) and the molecular weight distribution ( $M_w/M_n$ ) were determined using SEC-LALLS. The values of  $M_n$ ,  $M_w$ ,  $M_z$  and

**Table 3.** Average molecular weight of PMMA calibration standards

Sample No	Molecular weight [g/mol]
PMMA1	451 000
PMMA2	139 000
PMMA3	52 600
PMMA4	20 800

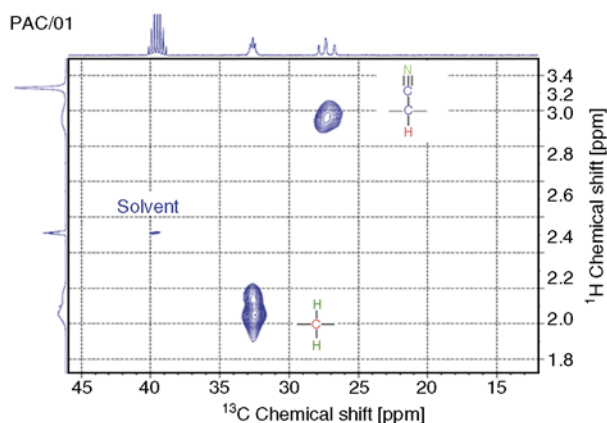


**Figure 8.** SEC-LALLS elution curves for PAC, a) PAC/01, b) PAC/04, c) PAC/03, d) PAC/04

MWD are calculated for PAC/01–PAC/04 using SEC-LALLS data processing system which is given in Table 2. The ratio of  $M_w/M_n$  varies between 2.1 to 2.5 and also the ratio of  $M_z/M_w$  varies between 1.6 to 2.0. Figure 8a–d shows SEC-LALLS elution curves for PAC/01–PAC/04. The values of  $M_v$ ,  $M_n$  ( $_{osm}$ ),  $M_n$  (SEC-LALLS),  $M_w$ , and  $M_z$  are  $1.61$ – $3.26 \cdot 10^4$ ,  $7.8$ – $14.3 \cdot 10^4$ ,  $4.7$ – $11.8 \cdot 10^4$ ,  $1.1$ – $2.57 \cdot 10^5$ , and  $2.25$ – $4.31 \cdot 10^5$  g/mol respectively. It has been authors' experience that  $M_n$  values determined by SEC-LALLS are rarely in agreement with  $M_n$  values from the membrane osmometer, SEC-LALLS values generally being lower than  $M_n$  values determined from the osmometer.

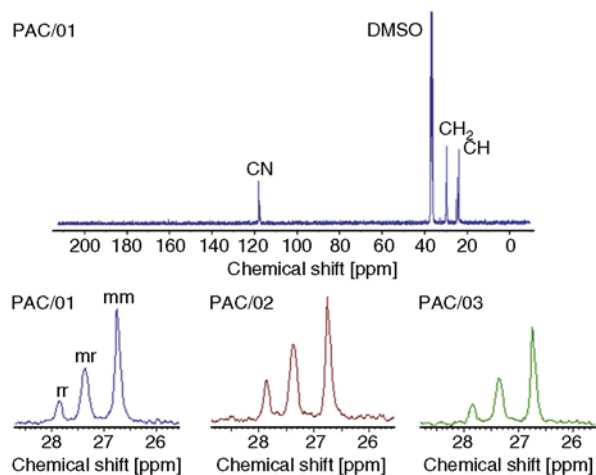
The stereoregularity of PAC/01–PAC/04 are also estimated in terms of triad tacticity content using  $^{13}C$  NMR spectra. Basically, due to higher resolu-





**Figure 9.** 2D-NMR – COSY-HMQC Techniques:  $^{13}\text{C}$ – $^1\text{H}$  shift correlation NMR spectra

tion and more extensive sweep width, this technique is used in most studies. The bonding network between methine carbon and methine hydrogen is established using 2D-NMR – COSY-HMQC technique which is shown in Figure 9. HMQC spectrum can also be used in the assignment of the proton spectrum by dispersing the proton resonances along the  $^{13}\text{C}$  dimension and reducing its multiplet overlaps.  $^{13}\text{C}$  NMR spectra with wide magnetization field caused higher splitting which was observed for all carbons.



**Figure 10.**  $^{13}\text{C}$  NMR spectra of isotactic PAC. Only methine carbon region is expanded (bottom).

Figure 10 shows the typical  $^{13}\text{C}$  NMR spectra of stereoregular isotactic PAC in which three types of carbon are observed: methine (CH), methylene ( $\text{CH}_2$ ), and cyano-carbon (CN). Assignments of methine carbon peaks were adopted as Minagawa *et al.* [37] which used NMR-400 MHz spectrometer with similar splitting for carbons. The triad tacticities of the polymers prepared were analyzed using methine carbon (CH) signals in the region 26.7–27.9 ppm. They consisted of three main peaks, corresponding to three possible steric triad configurations. The peaks at 26.75, 27.3, and 27.86 ppm correspond to isotactic (mm), atactic (mr), and syndiotactic (rr) respectively. The relative intensities of the peaks corresponding to methine carbon were used for determining the triad tacticity of PAC. The extent of isotacticity (mm) of these samples was found to be in the range of 47.6–51.4% (Table 4). The Bernoulli statistics is held satisfactorily for the PAC samples as listed in Table 4.

Two of the essential requirements that, polymer precursors for high performance carbon fiber materials must possess are high molecular weight and well controlled architecture [6, 7]. The molecular and structural characteristics of carbon fiber precursor polymers synthesized through conventional polymerization processes such as aqueous slurry, and solution techniques are presented in Table 5. Typically the molecular characteristics of PAC are  $M_n$  ( $4.25 \cdot 10^4$ ),  $M_v$  ( $2.09 \cdot 10^5$ ),  $M_w$  ( $1.82 \cdot 10^5$ ) (suspension process) and  $M_n$  ( $4.28 \cdot 10^4$ ),  $M_v$  ( $1.61 \cdot 10^5$ ),  $M_w$  ( $1.43 \cdot 10^5$ ) (solution process). In the present solid phase polymerization technique, the molecular weight increased with conversion and molecular weight distribution around 2.1–2.5 throughout the polymer synthesis. There was also a strong dependence of the initiator concentration on the molecular weight of the polymer. Then, the molecular weights increased in a linear fashion with increasing conversion and that the absolute molecular weights ( $M_n$  (osmometry) ( $7.8$ – $14.3 \cdot 10^4$ )) were close to the

**Table 4.** Characterization of stereoregular PAC samples

Sample code	Chemical shift [ppm]			Triad tacticity [%]			
	mm	mr	rr	I <sup>a</sup>	A <sup>b</sup>	S <sup>c</sup>	4IS/A <sup>2</sup>
PAC/01	26.77	27.39	27.86	47.8	37.4	14.8	2.023
PAC/02	26.76	27.39	27.85	47.6	36.9	15.5	2.167
PAC/03	26.76	27.36	27.86	51.4	33.9	14.7	2.629
PAC/04	26.76	27.37	27.84	50.1	35.6	14.3	2.261

<sup>a</sup>Isotactic

<sup>b</sup>Atactic

<sup>c</sup>Syndiotactic

**Table 5.** Molecular characteristics of PAC through different polymerization techniques

Entry	Polymer	Process	Solvent	Molecular parameters				Structural parameters Triad tacticity [%]		
				$M_v \cdot 10^{-5}$ [g/mol]	$M_n \cdot 10^{-4}$ [g/mol]	$M_w \cdot 10^{-5}$ [g/mol]	$M_w/M_n$	I	A	S
1	AN/ITA copolymer 98.5/1.5; wt/wt AIBN, 50°C	Aqueous slurry polymerization	DMSO/H <sub>2</sub> O	2.09	4.25	1.82	4.28	28.1	47	24.9
2	AN/ITA copolymer 98.5/1.5; wt/wt AIBN, 55°C	Solution polymerization	DMSO	1.61	4.28	1.43	3.34	26.4	48.5	25.1
3	AN/ITA copolymer 98.5/1.5; wt/wt AIBN, 70°C	Solid phase polymerization	No solvent used	1.64	4.70	1.17	2.503	50.1	35.6	14.3

theoretical values determined by the ratio of the initial monomer and initiator concentration (i.e.,  $M_{n,theo} = 53[AN]_0/[AIBN]_0$ ). This means that the initiator efficiency of the polymerization was close to unity. The molecular weight characteristics of PAC obtained through solid phase polymerization are  $M_n$  ( $4.7 \cdot 10^4$ ),  $M_v$  ( $1.64 \cdot 10^5$ ),  $M_w$  ( $1.17 \cdot 10^5$ ). This compares well with the other conventional polymerization processes.

#### 4. Conclusions

Isotactic rich stereoregular PAC was synthesized by solid phase polymerization using hexagonal crystalline metal salts (Nickel chloride or Magnesium chloride) with AIBN as initiator. The bonding network between methine carbon and methine hydrogen is established using 2D-NMR – COSY-HMQC technique. <sup>1</sup>H NMR via HMQC triad sequence was also performed for methine protons. Assignment of stereosequences was performed on methine carbon at triad sequences level using <sup>13</sup>C spectroscopy. Bernoullian statistics is fitted well by the experimental results. The molecular weight distributions and various average molecular weights of PAC were estimated. Structure-property relationship, such as the intrinsic viscosity ( $\eta$ ) versus the number average molecular weight ( $M_n$ ) found in DMSO is  $\eta = 2.53 \cdot 10^{-4} \cdot M_n^{0.72}$ . The molecular weight distributions of these polymers as determined from  $M_v/M_n$  and  $M_w/M_n$  were 2.1 to 3.2 and 2.1 to 2.5 respectively. It is concluded that PAC with isotactic content over 50% can be prepared successfully by solid phase polymerization.

#### Acknowledgements

Financial support by Council of Scientific and Industrial Research (CSIR), New Delhi under Supra Institutional Project (SIP-IFCAP-04) is gratefully acknowledged. We thank The Director, CSIR-National Aerospace Laboratories, Bangalore for his support and permission to publish this work. The authors also grateful to the management and principal of Jamal Mohammed College, Bharathidasan University, Tiruchirpalli, India for their encouragement and help.

#### References

- [1] Frohs W., Jaeger H.: Carbon fiber and composite material. *Tanso*, **249**, 174–178 (2011). DOI: [10.7209/tanso.2011.174](https://doi.org/10.7209/tanso.2011.174)
- [2] Kroschwitz J. I.: Encyclopedia of polymer science and technology. Wiley, Hoboken (2003).
- [3] Kowalewski T., Tsarevsky N. V., Matyjaszewski K.: Nanostructured carbon arrays from block copolymers of polyacrylonitrile. *Journal of American Chemical Society*, **124**, 10632–10633 (2002). DOI: [10.1021/ja0178970](https://doi.org/10.1021/ja0178970)
- [4] Kruk M., Dufour B., Celer E. B., Kowalewski T., Jaroniec M., Matyjaszewski K.: Synthesis of mesoporous carbons using ordered and disordered mesoporous silica templates and polyacrylonitrile as carbon precursor. *Journal of Physical Chemistry B*, **109**, 9216–9225 (2005). DOI: [10.1021/jp045594x](https://doi.org/10.1021/jp045594x)
- [5] Long J. W., Dunn B., Rolison D. R., White H. S.: Three-dimensional battery architectures. *Chemical Reviews*, **104**, 4463–4492 (2004). DOI: [10.1021/cr0207401](https://doi.org/10.1021/cr0207401)
- [6] Hou C., Qu R., Liu J., Ying L., Wang C.: High-molecular-weight polyacrylonitrile by atom transfer radical polymerization. *Journal of Applied Polymer Science*, **100**, 3372–3376 (2006). DOI: [10.1002/app.23727](https://doi.org/10.1002/app.23727)

- [7] Pitto V., Voit B. I., Loontjens T. J. A., van Benthem R. A. T. M.: New star-branched poly(acrylonitrile) architectures: ATRP synthesis and solution properties. *Macromolecular Chemistry and Physics*, **205**, 2346–2355 (2004).  
DOI: [10.1002/macp.200400319](https://doi.org/10.1002/macp.200400319)
- [8] Morgan P.: Carbon fiber and their composites. CRC Press, Boca Raton (2005).
- [9] Kamide K., Dobashi T.: Physical chemistry of polymer solutions. Theoretical background. Elsevier, Amsterdam (2000).
- [10] Wu G. Y., Qi Y. C., Lu G. J., Wei Y. K.: Alternating copolymerization of acrylate and isobutylene. *Polymer Bulletin*, **22**, 393–400 (1989).  
DOI: [10.1007/BF00263078](https://doi.org/10.1007/BF00263078)
- [11] Gotoh Y., Yamashita M., Nakamura M., Toshima N., Hirai H.: Stereoregulation in the alternating copolymerization giving highly coheterotactic poly(methyl methacrylate-alt-styrene). Direct determination of coisotactic parameters. *Chemistry Letters*, **21**, 53–56 (1991).  
DOI: [10.1246/cl.1991.53](https://doi.org/10.1246/cl.1991.53)
- [12] Isobe Y., Fujioka D., Habaue S., Okamoto Y.: Efficient Lewis acid-catalyzed stereocontrolled radical polymerization of acrylamides. *Journal of American Chemical Society*, **123**, 7180–7181 (2001).  
DOI: [10.1021/ja0158881](https://doi.org/10.1021/ja0158881)
- [13] Matsuzaki K., Uryu T., Okada M., Shiroki H.: The stereoregularity of polyacrylonitrile and its dependence on polymerization temperature. *Journal of Polymer Science*, **6**, 1475–1487 (1968).  
DOI: [10.1002/pol.1968.150060606](https://doi.org/10.1002/pol.1968.150060606)
- [14] Kamide K., Yamazaki H., Miyazaki Y.: Effects of stereoregularity on molecular parameters of polyacrylonitrile polymerized by gamma-ray irradiation. *Polymer Journal*, **18**, 819–836 (1986).  
DOI: [10.1295/polymj.18.819](https://doi.org/10.1295/polymj.18.819)
- [15] Yamazaki H., Miyazaki Y., Kamide K.: Stereospecific polymerization of acrylonitrile using acrylonitrile-urea canal complex initiated by  $\gamma$ -ray irradiation: Roles of radical chain transfer reagents. *Polymer Journal*, **23**, 765–779 (1991).  
DOI: [10.1295/polymj.23.765](https://doi.org/10.1295/polymj.23.765)
- [16] Matsuzaki K., Okada M., Uryu T.: Triad tacticity of polyacrylonitrile. *Journal of Polymer Science Part A1: Polymer Chemistry*, **9**, 1701–1714 (1971).  
DOI: [10.1002/pol.1971.150090619](https://doi.org/10.1002/pol.1971.150090619)
- [17] Minagawa K., Ute K., Kitayama T., Hatada K.: Determination of stereoregularity of  $\gamma$ -irradiation canal polymerized polyacrylonitrile by 1H 2D J-resolved NMR spectroscopy. *Macromolecules*, **27**, 3669–3671 (1994).  
DOI: [10.1021/ma00091a032](https://doi.org/10.1021/ma00091a032)
- [18] Kamide K., Ono H., Hisatani K.: Stereospecificity in the polymerization of acrylonitrile using anionic initiators including dialkylmagnesium. *Polymer Journal*, **24**, 917–930 (1992).  
DOI: [10.1295/polymj.24.917](https://doi.org/10.1295/polymj.24.917)
- [19] White D. M.: Stereospecific polymerization in urea canal complexes. *Journal of American Chemical Society*, **82**, 5678–5685 (1960).  
DOI: [10.1021/ja01506a031](https://doi.org/10.1021/ja01506a031)
- [20] Matyjaszewski K., Xia J.: Atom transfer radical polymerization. *Chemical Reviews*, **101**, 2921–2990 (2001).  
DOI: [10.1021/cr940534g](https://doi.org/10.1021/cr940534g)
- [21] Venkatesh R., Yajjou L., Koning C. E., Klumperman B.: Novel brush copolymers via controlled radical polymerization. *Macromolecular Chemistry and Physics*, **205**, 2161–2168 (2004).  
DOI: [10.1002/macp.200400252](https://doi.org/10.1002/macp.200400252)
- [22] Feng W., Brash J., Zhu S.: Atom-transfer radical grafting polymerization of 2-methacryloyloxyethyl phosphorylcholine from silicon wafer surfaces. *Journal of Polymer Science Part A: Polymer Chemistry*, **42**, 2931–2942 (2004).  
DOI: [10.1002/pola.20095](https://doi.org/10.1002/pola.20095)
- [23] Hadjichristidis N., Latrou H., Pitsikalis M., Mays J.: Macromolecular architectures by living and controlled/living polymerizations. *Progress in Polymer Science*, **31**, 1068–1132 (2006).  
DOI: [10.1016/j.progpolymsci.2006.07.002](https://doi.org/10.1016/j.progpolymsci.2006.07.002)
- [24] Matyjaszewski K., Müller A. H. E.: 50 years of living polymerization. *Progress in Polymer Science*, **31**, 1039–1040 (2006).  
DOI: [10.1016/j.progpolymsci.2006.09.002](https://doi.org/10.1016/j.progpolymsci.2006.09.002)
- [25] Braunecker W. A., Matyjaszewski K.: Recent mechanistic developments in atom transfer radical polymerization. *Journal of Molecular Catalysis A: Chemical*, **254**, 155–164 (2006).  
DOI: [10.1016/j.molcata.2006.01.076](https://doi.org/10.1016/j.molcata.2006.01.076)
- [26] Braunecker W. A., Matyjaszewski K.: Controlled/living radical polymerization: Features, developments, and perspectives. *Progress in Polymer Science*, **32**, 93–146 (2007).  
DOI: [10.1016/j.progpolymsci.2006.11.002](https://doi.org/10.1016/j.progpolymsci.2006.11.002)
- [27] Cossens V., Pintauer T., Matyjaszewski K.: Functional polymers by atom transfer radical polymerization. *Progress in Polymer Science*, **26**, 337–377 (2001).  
DOI: [10.1016/S0079-6700\(01\)00003-X](https://doi.org/10.1016/S0079-6700(01)00003-X)
- [28] Pyun J., Matyjaszewski K.: Synthesis of nanocomposite organic/inorganic hybrid materials using controlled/‘living’ radical polymerization. *Chemistry of Materials*, **13**, 3436–3448 (2001).  
DOI: [10.1021/cm011065j](https://doi.org/10.1021/cm011065j)
- [29] Davis K., Matyjaszewski K.: *Advances in polymer science*. Springer, Berlin (2002).
- [30] Pyun J., Kowalewski T., Matyjaszewski K.: Synthesis of polymer brushes using atom transfer radical polymerization. *Macromolecular Rapid Communications*, **24**, 1043–1059 (2003).  
DOI: [10.1002/marc.200300078](https://doi.org/10.1002/marc.200300078)

- [31] Ravi P., Divakar S.:  $\beta$ -cyclodextrin regulated stereoregularity and molecular weight in inclusion polymerization of acrylonitrile. *Journal of Macromolecular Science Part A: Pure and Applied Chemistry*, **36**, 1935–1948 (1999).  
DOI: [10.1081/MA-100101635](https://doi.org/10.1081/MA-100101635)
- [32] Tomoko I., Yuhei M.: Method for producing polyacrylonitrile based fiber and method for producing carbon fiber. Japanese Patent JP2011042893, Japan (2011).
- [33] Sho T., Koichi S.: Precursor for carbon fiber, method for producing the same. Japanese Patent JP2001288613A, Japan (2001).
- [34] Kany H-P., Hasse H., Maurer G.: Thermodynamic properties of aqueous poly(vinylpyrrolidone) solutions from laser-light-scattering, membrane osmometry, and isopiestic measurements. *Journal of Chemical Engineering Data*, **48**, 689–698 (2003).  
DOI: [10.1021/je020203y](https://doi.org/10.1021/je020203y)
- [35] Ren L., Hardy C. G., Tang S., Doxie D. B., Hamidi N., Tang C.: Preparation of side-chain 18-e cobaltocenium-containing acrylate monomers and polymers. *Macromolecules*, **43**, 9304–9310 (2010).  
DOI: [10.1021/ma101935a](https://doi.org/10.1021/ma101935a)
- [36] Imaizumi M., Okino Y., Yoshikawa K., Koyama K.: Relationship between intrinsic viscosity and molecular weight (MW) of PBS and PBSA determined by SEC-LALLS and SEC-viscometry (in Japanese). *Seikei-Kakou*, **15**, 419–423 (2003).  
DOI: [10.4325/seikeikakou.15.419](https://doi.org/10.4325/seikeikakou.15.419)
- [37] Minagawa M., Taira T., Yabuta Y., Nozaki K., Yoshii F.: An anomalous tacticity–crystallinity relationship: A WAXD study of stereoregular isotactic (83–25) poly(acrylonitrile) powder prepared by urea clathrate polymerization. *Macromolecules*, **34**, 3679–3683 (2001).  
DOI: [10.1021/ma002173e](https://doi.org/10.1021/ma002173e)

# Crystallization behavior and mechanical properties of nano-CaCO<sub>3</sub>/β-nucleated ethylene-propylene random copolymer composites

J. H. Mai<sup>1,2</sup>, M. Q. Zhang<sup>1</sup>, M. Z. Rong<sup>1</sup>, T. Bárány<sup>3</sup>, W. H. Ruan<sup>1,2\*</sup>

<sup>1</sup>Materials Science Institute, Sun Yat-sen (Zhongshan) University, 510275 Guangzhou, China

<sup>2</sup>Key Laboratory for Polymeric Composite and Functional Materials of Ministry of Education, DSAPM Lab, School of Chemistry and Chemical Engineering, Sun Yat-sen (Zhongshan) University, 510275 Guangzhou, China

<sup>3</sup>Department of Polymer Engineering, Faculty of Mechanical Engineering, Budapest University of Technology and Economics, Műegyetem rkp. 3., H-1111 Budapest, Hungary

Received 11 December 2011; accepted in revised form 8 April 2012

**Abstract.** To provide ethylene-propylene random copolymer (PPR) with balanced mechanical properties, β-nucleating agent and CaCO<sub>3</sub> nanoparticles are incorporated into PPR matrix by melt blending. It is found that crystallization rate and relative content of β-crystal increase with the addition of β-nucleating agent together with nanoparticles. Size of PPR spherulite is greatly reduced, and a specific morphology appears, in which α-crystal lamella is grown upon the β-nucleus. The results suggest that both β-nucleating agent and nano-CaCO<sub>3</sub> have heterogeneous nucleation and synergistic effects on β-nucleation of PPR. Mechanical characterization shows that mechanical properties of PPR can be tuned by incorporation of β-nucleating agent and nano-CaCO<sub>3</sub> particles. Under suitable compositions, low temperature impact strength and high temperature creep resistance of PPR, the bottlenecks of application of such material, can be simultaneously improved without sacrificing the Young's modulus and tensile strength.

**Keywords:** mechanical properties, ethylene-propylene random copolymer, β-nucleating agent, nano-CaCO<sub>3</sub>, crystallization

## 1. Introduction

As one of the most popular commodity plastics, polypropylene (PP) is facing the challenge of improving its mechanical properties to meet versatile application requirements. Accordingly, random copolymers of propylene with a low amount of 1-olefins such as ethylene, 1-butene, 1-hexene and 1-octane are synthesized. Among these copolymers, ethylene-propylene random copolymer (PPR) has received a great deal of attentions owing to its higher impact strength than isotactic PP [1]. It has been used for making pipes, plates, domestic appliances and automobiles. However, the introduction of ethylene units leads to lower crystallization temperature and

degree of crystallinity of the polymer. Meanwhile, stiffness, strength, creep properties and thermal deformation temperature of PPR also decrease. Low temperature impact strength of such materials is still poor, causing problems for parts assembling and potential safety hazards. In this context, modification of PPR is necessary for acquiring balanced mechanical properties. Considering that crystalline morphology and degree of crystallinity determine structure and properties of semi-crystalline polymers [2], improving of overall performance of PPR had better to start with crystallization aspects. So far as we know, toughness and thermal deformation temperature of β-form isotactic polypropylene

\*Corresponding author, e-mail: [cesrwh@mail.sysu.edu.cn](mailto:cesrwh@mail.sysu.edu.cn)  
© BME-PT

(iPP) are much higher than that of  $\alpha$ -form iPP [3–10]. However,  $\beta$ -modification contingently occurs in commercial PP and can only be formed under critical conditions like large temperature gradient [11, 12], shearing the melt [13, 14] or adding selective  $\beta$ -nucleating agent ( $\beta$ -NA) [15]. Comparatively, the addition of specific nucleating agents is the most reliable method for the preparation of the beta-form PP [15]. It would increase crystallization temperature and degree of crystallinity of iPP, and accelerates the crystallization rate.

Additionally, incorporation of nanometer-scale inorganic particles is a promising approach to improve both mechanical and thermal properties of polymeric materials. It was reported that when nano- $\text{CaCO}_3$  particles were added to iPP, not only modulus and toughness of the matrix were significantly improved [16], but also  $\beta$ -crystals were formed [17].

Although most available documents deal with  $\beta$ -nucleated i-PP modification, and few have paid attention to random polypropylene copolymer [18–25], the results are meaningful. Considering that nano- $\text{CaCO}_3$  have applications in PPR products, and gaining enlightenment from the studies on filled  $\beta$ -nucleated iPP [26–30], we plan to add  $\beta$ -nucleating agent and  $\text{CaCO}_3$  nanoparticles into PPR together. Crystalline characteristics, structure and mechanical properties of PPR composites prepared under processing conditions will be studied. It is hoped that synergistic effect would appear, overcoming the above-mentioned shortcomings of PPR. Furthermore, knowledge of structure and properties adjustment of PPR can be acquired. These are the objectives of the present work.

## 2. Experimental

### 2.1. Materials

Ethylene-propylene random copolymer (trade name: PPR4220; MFI = 0.25 g/10 min at 230°C and 2.16 kg, content of ethylene is approximately 5.0 mol% and the molecular weight distribution is approximately 4.0) was supplied by Yanshan Petrochemical Co., Beijing, China. The rare-earth  $\beta$ -nucleating agent (trade name WBG-II, which is a heteronuclear dimetal complex of lanthanum and calcium with some specific ligands) was obtained from Guangdong Winner Functional Materials Co., Ltd. Foshan, China. A commercial grade of active

calcium carbonate nanoparticles surface pre-treated by stearic acid (with average size of 30 nm, content of  $\text{CaCO}_3 \geq 95\%$  and pH = 8.5~10.5) were obtained from Henan Keli New Material Co., Ltd. Xuchang, China.

### 2.2. Sample preparation

Before melt mixing, PPR and nano- $\text{CaCO}_3$  particles were dried at 60°C for 12 h. The  $\beta$ -nucleating agent and nanofillers were blended with PPR under certain proportions in a Haake mixer (Rheocord 300p, Haake, Germany) at 180°C and 60 rpm for 10 min. For comparison,  $\beta$ -nucleating agent/PPR and nano- $\text{CaCO}_3$ /PPR composites were prepared under same ways. Then, the compounds were broken and injection molded into standard bars for mechanical tests by a vertical injection molding machine (Y-350, Yida Co., Ltd, China) at barrel temperature of 210°C. Prior to the tests, samples were conditioned at room temperature (23±2°C) and relative humidity of 50±5% for 48 h.

### 2.3. Characterization

Non-isothermal melting and crystallization behaviors of PPR and its composites were tested by differential scanning calorimeter (DSC) (MDSC2910, TA, USA) with nitrogen as purge gas. Pure indium and zinc were used as standard materials to calibrate both the temperature scale and melting enthalpy. All the samples for DSC measurements were cut from injection molded bars. For each measurement, sample was heated up to 200°C and maintained at this temperature for 5 min to eliminate thermal history. Afterwards, the sample was cooled down to 50°C and reheated to 200°C again. Both heating and cooling rates were 10°C/min.

Wide angle X-ray diffraction (WAXD,) pattern of the materials was collected at room temperature by a diffractometer (D-max 2200 VPC, Rigaku, Japan) with  $\text{Cu K}_\alpha$  radiation. The X-ray source was set at voltage of 40 kV and current of 30 mA in a range of  $2\theta = 5\text{--}35^\circ$ , with a scanning rate of 5°/min. All the samples for WAXD measurements were cut from injection molded bars. The dimension of samples is 10 × 10 × 2 mm.

A Leitz polarized light microscopy (PLM) (Orthoplan Pol, Leitz, German) with heating stage (THMS600, Linkam, England) was used for morphology observation. The sample sliced to thickness of 10–20  $\mu\text{m}$

was firstly heated to 230°C, kept for 5 min to eliminate thermal history, and slid into a chamber set at the predetermined crystallization temperature of 130°C until completion of crystallization. In addition, morphological change during heating (heating rate = 0.1°C/min) was observed. The images presented in this paper were taken under orthogonally polarized condition.

Tensile test was conducted on ASTM D638-98 Type V specimens using a universal testing machine (H10K-S, Hounsfield, England) at a crosshead speed of 2 mm/min for Young’s modulus and 50 mm/min for tensile strength under room temperature. Notched Charpy impact strengths of the specimens were measured at room temperature and –10°C according to ISO 179-2 by an advanced pendulum impact device (ATLAS, America) at a rate of 3.8 m/s. The specimens (size: 80 × 10 × 4 mm<sup>3</sup>) were notched with an automatic sample notcher (ASN, Dynisco instruments, USA). An initial crack length of 2 mm and a span of 40 mm were selected. Five specimens were tested for each group of specimens.

Creep resistance of PPR and its composites was determined at 70°C under constant stress of 1 MPa and static force of 0.1 N with a dynamic mechanical analysis instrument (DMA2980, TA, USA), using three-point bending mode. The specimen size was 55 × 10 × 3 mm<sup>3</sup>.

### 3. Results and discussion

#### 3.1. Non-isothermal crystallization and melting behaviors

Since PPR is mostly processed under non-isothermal conditions, study of its non-isothermal crystallization and melting behaviors is of great technological significance. Figures 1 shows the cooling and

heating traces of PPR and its composites measured by DSC. The corresponding characteristic parameters are summarized in Table 1.

For pristine PPR, the temperature at which the crystallization curve starts to deviate from the baseline,  $T_c^i$ , peak temperature of crystallization,  $T_c^p$ , and onset temperature of crystallization,  $T_c^{on}$ , are 111.1, 103.0 and 106.3°C, respectively (Figure 1a). When a small amount of  $\beta$ -nucleating agent, nano-CaCO<sub>3</sub> or nano-CaCO<sub>3</sub>/ $\beta$ -nucleating agent is added, the values of  $T_c^i$ ,  $T_c^p$  and  $T_c^{on}$  of the composites become higher than those of PPR, and the increment amplitudes are about 10°C for  $\beta$ -nucleating agent or nano-CaCO<sub>3</sub>/ $\beta$ -nucleating agent added systems. It means that  $\beta$ -nucleating agent and CaCO<sub>3</sub> nanoparticles have heterogeneous nucleation effects on PPR, and nucleation of  $\beta$ -nucleating agent is more effective than that of nano-CaCO<sub>3</sub>.

Careful analysis of the data in Table 1 reveals that the addition of  $\beta$ -nucleating agent increases the half width of the crystallization peak in the high temperature region,  $\Delta T_1$ , and reduces the slope of the high-temperature side of exotherm,  $S_i$ , of PPR. On the contrary,  $\Delta T_1$  of composites decreases, and  $S_i$  increases when the nano-CaCO<sub>3</sub> added alone. In fact, the two parameters of  $\Delta T_1$  and  $S_i$  are closely related to crystal growth rate [31]. The higher  $\Delta T_1$  and smaller  $S_i$ , the lower crystal growth rate is. From Table 1 it is also noted that when nano-CaCO<sub>3</sub>/ $\beta$ -nucleating agent are incorporated to PPR,  $S_i$  values of the composites are smaller, and  $\Delta T_1$  values are also higher than those of  $\beta$ -nucleated PPR. Evidently, the rate of crystal growth of PPR increases with the addition of nano-CaCO<sub>3</sub>, but decreases with the addition of  $\beta$ -nucleating agent or  $\beta$ -nucleating agent/nano-CaCO<sub>3</sub>. So far as we know, for the given random

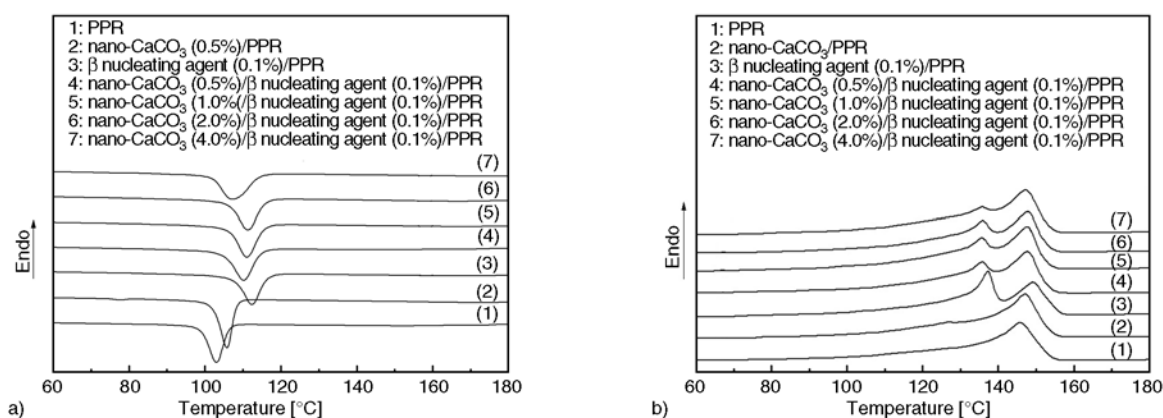


Figure 1. (a) DSC cooling and (b) heating curves of PPR and its composites

**Table 1.** Non-isothermal crystallization and melting data of PPR and its composites obtained from DSC

Samples	<sup>a</sup> T <sub>c</sub> <sup>i</sup> [°C]	<sup>b</sup> T <sub>c</sub> <sup>p</sup> [°C]	<sup>c</sup> T <sub>c</sub> <sup>on</sup> [°C]	<sup>d</sup> ΔT <sub>1</sub> [°C]	<sup>e</sup> ΔT <sub>2</sub> [°C]	<sup>f</sup> S <sub>i</sub>	<sup>g</sup> T <sub>m</sub> <sup>α</sup> [°C]	<sup>h</sup> T <sub>m</sub> <sup>β</sup> [°C]	<sup>i</sup> T <sub>m</sub> <sup>i</sup> [°C]
PPR	111.1	103.0	106.3	3.3	42.5	0.51	145.6	–	142.7
β-NA (0.1 wt%)/PPR	123.8	112.4	116.4	4.0	24.9	0.34	149.1	137.3	132.3
β-NA (0.2 wt%)/PPR	124.7	112.5	116.7	4.2	24.7	0.32	149.0	137.2	133.0
β-NA (0.3 wt%)/PPR	124.7	111.7	116.1	4.4	25.3	0.30	149.0	137.1	133.1
β-NA (0.5 wt%)/PPR	125.2	112.9	117.7	4.8	24.2	0.27	148.8	137.1	133.1
0.5 wt% CaCO <sub>3</sub> /PPR	113.9	105.8	108.3	2.5	41.2	0.87	147.0	–	142.3
1.0 wt% CaCO <sub>3</sub> /PPR	114.1	105.9	108.2	2.3	40.7	0.94	146.6	–	143.1
2.0 wt% CaCO <sub>3</sub> /PPR	114.0	105.6	108.2	2.6	41.4	0.86	147.0	–	141.9
4.0 wt% CaCO <sub>3</sub> /PPR	113.9	105.9	108.3	2.4	40.9	0.81	146.8	–	142.1
Nano-CaCO <sub>3</sub> (0.5 wt%)/β-NA (0.1 wt%)/PPR	120.8	110.2	114.7	4.5	25.7	0.29	147.6	135.9	132.5
Nano-CaCO <sub>3</sub> (1.0 wt%)/β-NA (0.1 wt%)/PPR	124.7	111.0	115.5	4.5	24.5	0.30	147.5	135.6	132.6
Nano-CaCO <sub>3</sub> (2.0 wt%)/β-NA (0.1 wt%)/PPR	126.2	111.3	115.8	4.5	24.7	0.30	147.7	135.9	133.0
Nano-CaCO <sub>3</sub> (4.0 wt%)/β-NA (0.1 wt%)/PPR	125.3	107.3	114.3	7.0	28.3	0.17	147.2	135.6	133.0

<sup>a</sup>T<sub>c</sub><sup>i</sup>: the temperature at which exothermic curve starts to deviate from the baseline  
<sup>b</sup>T<sub>c</sub><sup>p</sup>: peak temperature of crystallization  
<sup>c</sup>T<sub>c</sub><sup>on</sup>: onset temperature of crystallization  
<sup>d</sup>ΔT<sub>1</sub> = T<sub>c</sub><sup>on</sup> – T<sub>c</sub><sup>p</sup>: half width of crystallization peak in the high temperature region  
<sup>e</sup>ΔT<sub>2</sub> = T<sub>m</sub><sup>p</sup> – T<sub>c</sub><sup>p</sup>: degree of supercooling  
<sup>f</sup>S<sub>i</sub>: slope of high-temperature side of exotherm  
<sup>g</sup>T<sub>m</sub><sup>α</sup>: peak temperature of melting of α crystal  
<sup>h</sup>T<sub>m</sub><sup>β</sup>: peak temperature of melting of β crystal  
<sup>i</sup>T<sub>m</sub><sup>i</sup>: initial melting temperature

copolymer in a wide temperature range, growth rate of β-phase crystal is lower than that of α-phase [15, 21, 23]. Therefore, the decrease of crystal growth rate of β-nucleating agent/PPR might be caused by generation of β-phase crystal. The obviously lower S<sub>i</sub> values of the composites containing both β-nucleating agent and nano-CaCO<sub>3</sub> indicate that the two components exert synergistic effect on inducing the formation of β-crystal of PPR.

On the other hand, the degree of supercooling, ΔT<sub>2</sub>, which characterizes the overall rate of crystallization, decreases with the addition of β-nucleating agent or nano-CaCO<sub>3</sub>/β-nucleating agent, demonstrating that the rates of crystallization of the composites are still higher than that of PPR. It is known that crystallization includes nucleation and crystal growth. In the above discussion, it was found that crystal growth rates of β-nucleated PPR and nano-CaCO<sub>3</sub>/β-nucleated PPR are lower than that of PPR, while the higher rate of crystallization hints effective heterogeneous nucleation effects of β-nucleating agent and nano-CaCO<sub>3</sub>/β-nucleating agent on PPR.

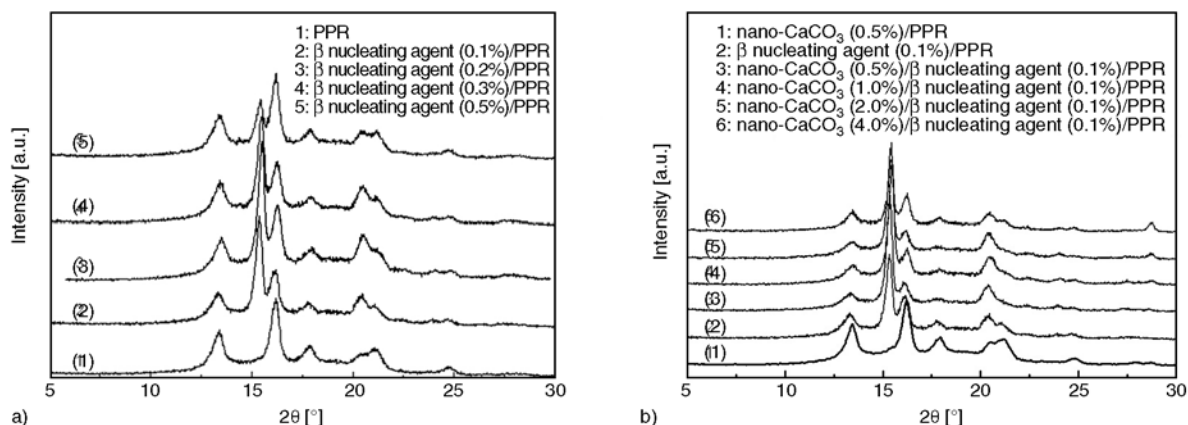
Similarly, melting behavior of PPR is largely affected by the incorporation of β-nucleating agent and nano-CaCO<sub>3</sub>/β-nucleating agent (Figure 1b). In the case of pristine PPR, there is only a single melting

peak on the heating curve with peak temperature of 145.6°C, which is much lower than that of isotactic PP due to the random embedment of ethylene units. For nano-CaCO<sub>3</sub>/PPR, a single melting peak on the heating curve with peak temperature around 147°C appears. When β-nucleating agent or nano-CaCO<sub>3</sub>/β-nucleating agent is added into PPR, two endothermic peaks appear: one around 148°C and another around 136°C. Considering the lower melting temperature of β-crystal than that of α-crystal [15], the melting peak in the higher temperature regime should represent melting of α-crystal, and the one in the lower temperature regime should result from melting of β-crystal. The increase of T<sub>m</sub><sup>α</sup> and appearance of T<sub>m</sub><sup>β</sup> with the addition of β-nucleating agent and nano-CaCO<sub>3</sub>/β-nucleating agent prove heterogeneous nucleation and β-crystal formation.

### 3.2. Crystalline characteristics

Figure 2 shows WAXD spectra of PPR and its composites. For the spectrum of PPR, the most intense reflections are present at 2θ of 14.0, 16.8, 18.6, 21.2 and 21.9°, corresponding to (110), (040), (130), (111) and (131) lattice planes of the most common α-monoclinic crystal. There is no new peak appearing in the spectra of nano-CaCO<sub>3</sub>/PPR, meaning that CaCO<sub>3</sub> nanoparticles used actually have no β-nucle-





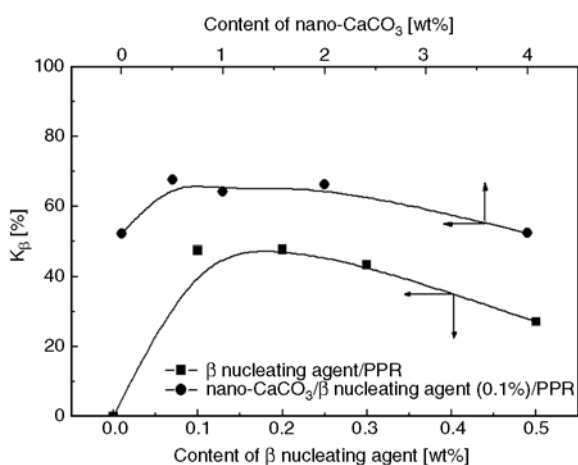
**Figure 2.** WAXD spectra of PPR and its composites a)  $\beta$ -nucleating/PPR systems, b) nano/ $\text{CaCO}_3$ / $\beta$ -nucleating/PPR systems

ating effect on PPR. For the spectra of  $\beta$ -nucleated PPR and nano- $\text{CaCO}_3$ / $\beta$ -nucleated PPR, a new peak at  $2\theta$  of around  $16.0^\circ$  is observed. It is assigned to (300) lattice plane of  $\beta$ -crystal, indicating the existence of  $\beta$ -crystal in PPR composites. There may also be (301) reflection of  $\beta$ -crystal at  $21.2^\circ$ , which overlaps (111) reflection of  $\alpha$ -crystal.

By using peak intensity of (300) reflection, the relative proportion of the  $\beta$ -crystal,  $K_\beta$ , can be calculated according to the empirical Equation (1) of Turner-Jones *et al.* [32]:

$$K_\beta = \frac{I_{(300)}}{I_{(110)} + I_{(040)} + I_{(130)} + I_{(300)}} \quad (1)$$

where  $I_{(300)}$  is the intensity of the (300) diffraction peaks of the WAXD patterns and  $I_{(110)}$ ,  $I_{(040)}$ ,  $I_{(130)}$  are the intensities of the (110), (040), and (130) diffraction peaks, respectively. The calculated values of  $K_\beta$  were plotted as a function of contents of  $\beta$ -nucleating agent and nano- $\text{CaCO}_3$  (Figure 3).



**Figure 3.** Relative amount of  $\beta$  crystal,  $K_\beta$ , of PPR as a function of contents of  $\beta$  nucleating agent and nano- $\text{CaCO}_3$

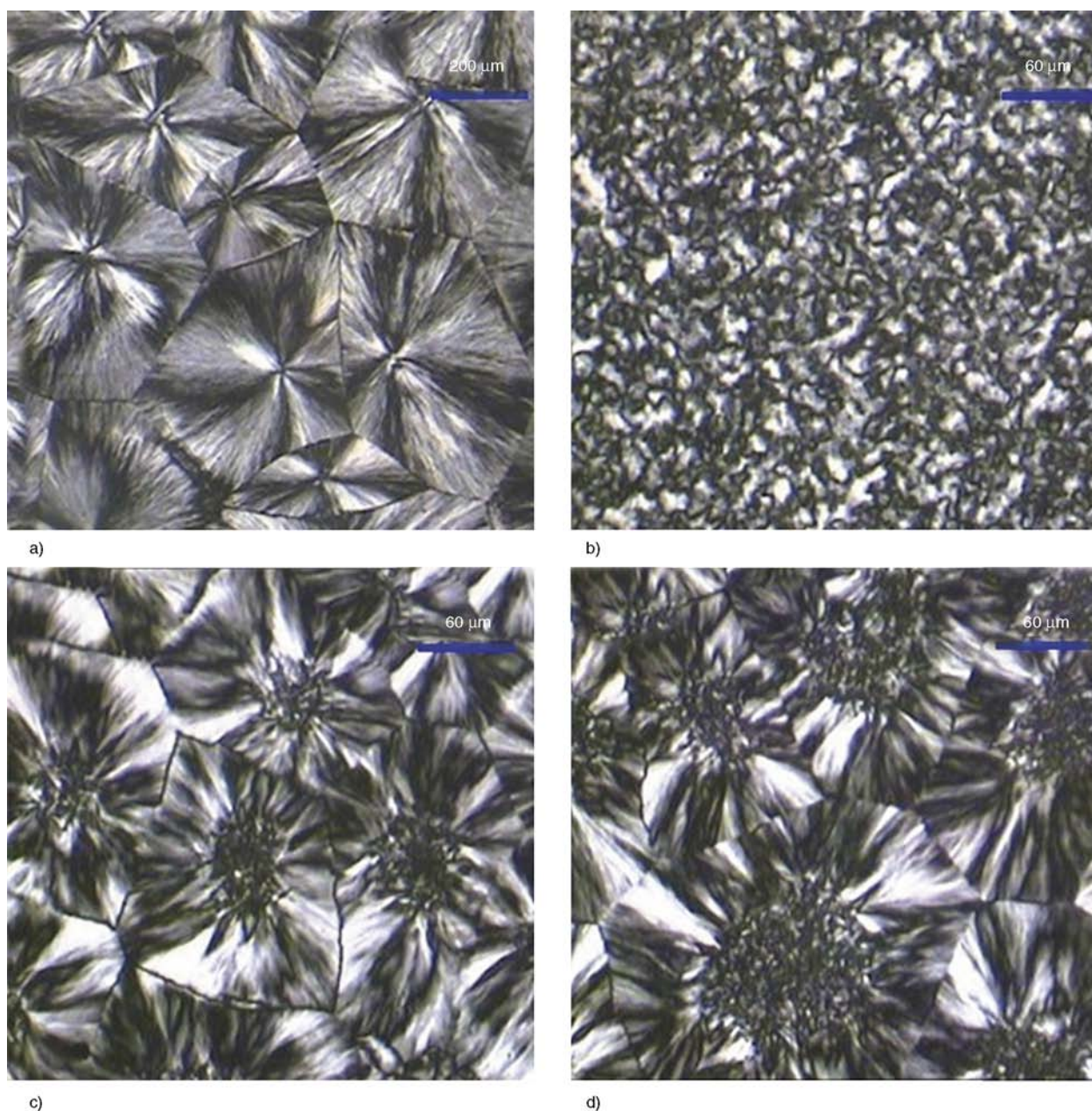
Clearly,  $K_\beta$  increases with a rise in content of  $\beta$ -nucleating agent, and reaches the maximum of 48.0% when the content of  $\beta$ -nucleating agent is around 0.1–0.15 wt%. Further increase of concentration of  $\beta$ -nucleating agent leads to slight reduction in  $K_\beta$ . The lowering the  $\beta$ -form content with increasing concentration of the  $\beta$ -nucleating agent might be ascribed to the dual nucleating ability of rare-earth typed  $\beta$ -nucleating agent [33, 34], on the surface of which formation of  $\alpha$ - and  $\beta$ -phase takes place. A similar phenomenon of the ‘critical’ content of nucleating agent was observed by Varga and Menyhárd [35]. In the case of constant content of  $\beta$ -nucleating agent of 0.1 wt%, the incorporation of nano- $\text{CaCO}_3$  can further increase  $K_\beta$  (Figure 3), manifesting that  $\beta$ -nucleating agent and nano- $\text{CaCO}_3$  have a synergistic effect on the formation of  $\beta$ -crystal. Above WAXD studies show that nano- $\text{CaCO}_3$  used has no  $\beta$ -nucleating effect on PPR. The synergistic  $\beta$ -nucleating effect of nanoparticles and  $\beta$ -nucleating agent might be attributed to formation of  $\text{CaCO}_3$ -supported  $\beta$ -nucleator. During processing, the  $\beta$ -nucleating agent is adsorbed and supported on the surface of the  $\text{CaCO}_3$  nanoparticles due to the polar interaction between rare-earth  $\beta$ -nucleating agent and  $\text{CaCO}_3$  particles. A monolayer of  $\beta$ -nucleating agent adsorbed on the surface of the  $\text{CaCO}_3$  particles might be obtained. Because of larger specific surface area of nanoparticles,  $\text{CaCO}_3$ -supported  $\beta$ -nucleator exhibits high  $\beta$ -nucleating efficiency for PPR crystallization. It has been reported that the content of  $\beta$ -phase in iPP nucleated by the nanoparticles supported  $\beta$ -nucleator are higher than that of iPP nucleated by same  $\beta$ -nucleator [36].  $K_\beta$  decreases with the increase of content of nano- $\text{CaCO}_3$  owing to enhanced  $\alpha$ -phase nucle-

ating ability of nanoparticles. Thus, the content of  $\beta$ -phase can be tuned by tuning composition of  $\beta$ -nucleating agent and nano- $\text{CaCO}_3$  particles.

Figure 4 shows optical micrographs of PPR and its composites crystallized under isothermal conditions. Pristine PPR specimen cooled from melt exhibits conventional spherulitic structure with a diameter of  $\sim 400 \mu\text{m}$  or more, and the interfaces between the spherulites are sharp and clear (Figure 4a). The introduction of nano- $\text{CaCO}_3$  and/or  $\beta$ -nucleating agent greatly changes crystalline morphology of PPR, including the decrease of spherulites size. A large

number of nuclei are induced within short time, accelerating the crystallization of PPR. The resultant spherulites overlapped each other, and hence become much smaller than those in pristine PPR.

It is worth noting that an interesting morphology, spherulites overgrowths onto the smaller crystal core, is observed in  $\beta$ -nucleated PPR or nano- $\text{CaCO}_3/\beta$ -nucleated PPR (Figure 4c and 4d). Výchopňová *et al.* [37] reported the same peculiar structure made of  $\beta$ -core and  $\alpha$ -crystal overgrowing on it in PP. There are two possibilities for formation of such mixed polymorphic forms. On one hand,  $\beta$ - $\alpha$  growth tran-

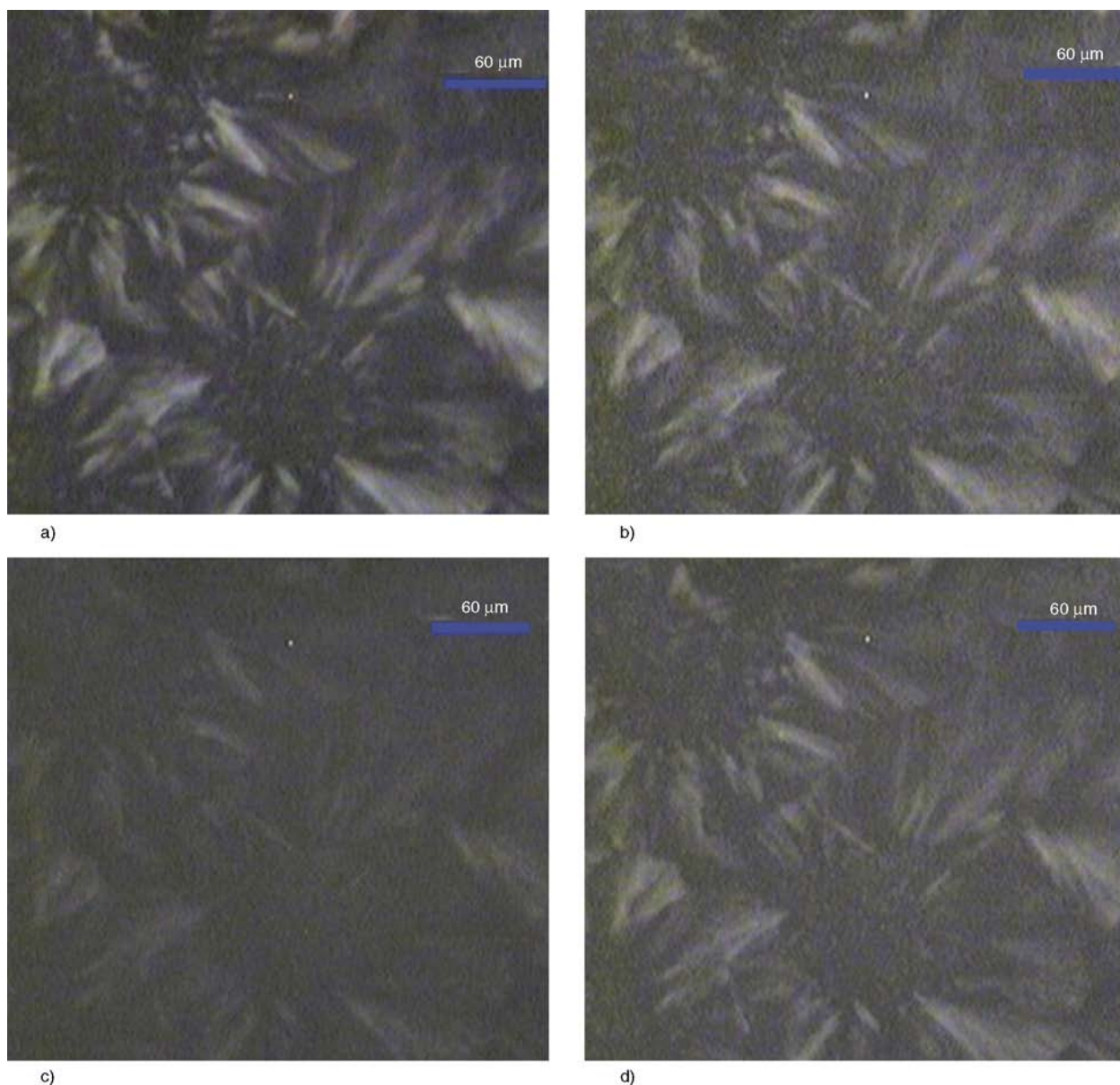


**Figure 4.** Optical micrographs of (a) PPR, (b) nano- $\text{CaCO}_3$  (0.5 wt%)/PPR, (c)  $\beta$  nucleated PPR (content of  $\beta$  nucleating agent: 0.1 wt%) and (d) nano- $\text{CaCO}_3$  (0.5 wt%)/ $\beta$  nucleated PPR (content of  $\beta$  nucleating agent: 0.1 wt%). Crystallization conditions:  $130^\circ\text{C}$ , 16 h.

sition might occur during crystallization of PPR composites. It was reported that  $\beta$ - $\alpha$  growth transition  $T_{(\beta\alpha)}$  occurs in the vicinity of 140°C for iPP [38, 39], above where the growth rate of the  $\alpha$ -phase ( $G_\alpha$ ) is higher than that of  $\beta$ -phase ( $G_\beta$ ). In the case of random copolymers with low-comonomer content, the  $\beta$ - $\alpha$  growth transition occurs in a wide temperature range because where  $G_\alpha$  was always higher than  $G_\beta$  for the given random copolymer and even no crossover temperature  $T_{(\beta\alpha)}$  was found below which  $G_\beta$  would be higher than  $G_\alpha$  [21]. Further studies show that the  $T_{(\beta\alpha)}$  of random copolymer PP shifts to lower temperatures [23]. Considering thermal condition of crystallization in the study, it is possible that  $\beta$ - $\alpha$  growth transition occurs. One the

other hand, polymorphic composition morphology might be connected with the dual nucleating ability of adopted nucleating agent, on the surface of which formation of  $\alpha$ - and  $\beta$ -phase takes place. Since in certain temperature range where  $G_\alpha$  was always higher than  $G_\beta$ , such  $\beta\alpha$  twin structure forms.

To confirm the structure of this peculiar crystalline morphology, the sample was slowly heated under optical microscopic observation to check the variation in the morphology (Figure 5). The photographs show that when temperature approaches to 132°C (Figure 5a), crystal cores begin to melt, and the melting is completed at 137°C (Figure 5b). As temperature continues to rise, the outer crystals start to melt at 142°C (Figure 5c), and the melt is com-



**Figure 5.** Optical micrographs showing melting process of  $\beta$  nucleated PPR (content of  $\beta$  nucleating agent: 0.1 wt%) after crystallization at 130°C for 16 h. Heating rate: 0.1°C/min. (a) 132°C, (b) 137°C, (c) 142°C and (d) 148°C.

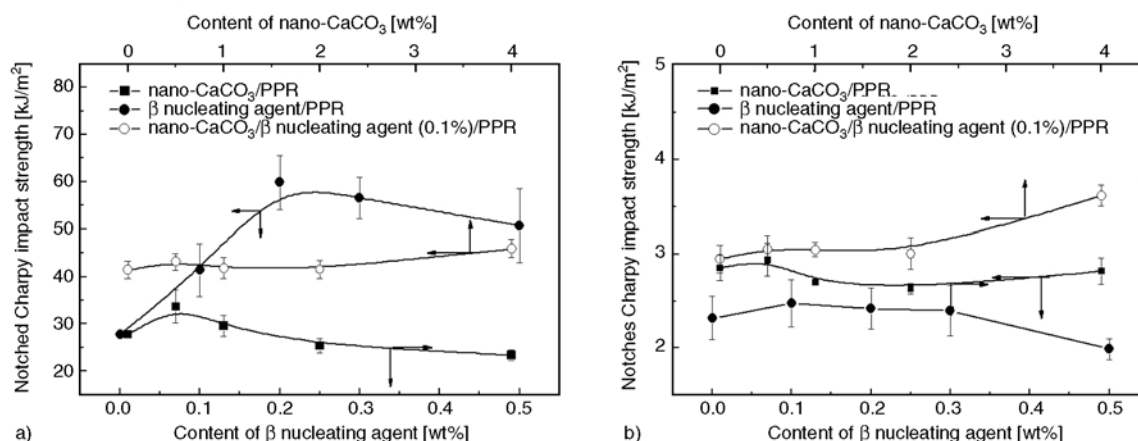
pleted at 148°C (Figure 5d). These four critical temperatures exactly fall between  $\beta$ - and  $\alpha$ -phase melting peak temperatures tested by DSC (Table 1). Accordingly, composition of this polymorphic structure can be determined. Namely, the core is made of  $\beta$ -phase (also including more or less  $\alpha$ -crystal), while  $\alpha$ -spherulites grows externally upon the cores.

### 3.3. Mechanical properties

Tensile properties of PPR and its composites are tested and listed in Table 2. Since the addition of  $\beta$ -nucleating agent to PPR induces the formation of  $\beta$ -crystals, Young's modulus and tensile strength of PPR slightly decrease. However, addition of nano-CaCO<sub>3</sub> to  $\beta$ -nucleated PPR is able to increase modulus and tensile strength of the system. As a result, the two parameters of nano-CaCO<sub>3</sub>/ $\beta$ -nucleated PPR composites are close to those of pristine PPR. With respect to elongation at break and area under tensile stress-strain curve, which is related to static

ductility, appearance of  $\beta$ -crystal in PPR certainly increases these two parameters as expected. The PPR composites with nano-CaCO<sub>3</sub> exhibit improved static ductility either.

Comparatively, the change in impact strength of the systems due to the incorporation of  $\beta$ -nucleating agent and nano-CaCO<sub>3</sub> particles is complicated (Figure 6).  $\beta$ -crystal is always believed to result in improved toughness of PP. As a result, when  $\beta$ -nucleating agent is added, room temperature impact strength of PPR is remarkably increased (Figure 6a). However, the addition of nano-CaCO<sub>3</sub> to PPR or to  $\beta$ -nucleated PPR does not obviously alter room temperature impact strength of the composites. The tendency of toughness variation disagrees with the dependence of  $K_\beta$  on nano-CaCO<sub>3</sub> content (Figure 3). This might be attributed to the fact that nano-CaCO<sub>3</sub> particles in PPR containing ethylene units cannot offer sufficient resistance to rapid crack propagation under high speed deformation circum-



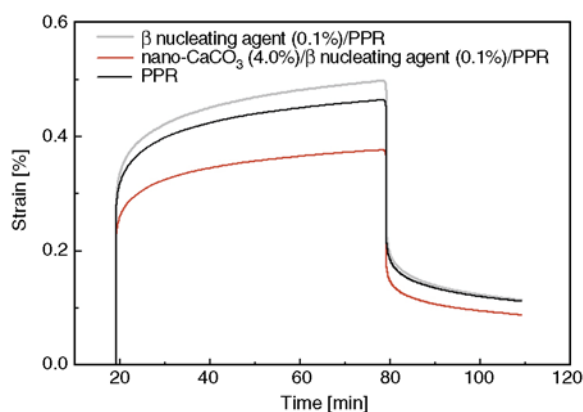
**Figure 6.** Notched Charpy impact strength of PPR as a function of contents of  $\beta$  nucleating agent and nano-CaCO<sub>3</sub>. Test temperature: (a) 23°C and (b) -10°C.

**Table 2.** Tensile properties of PPR and its composites

Samples	Young' modulus [GPa]	Tensile strength [MPa]	Elongation at break [%]	Area under stress-strain curve [GPa]
PPR	1133.0±35.7	52.5±2.4	79.8±26	9.69±1.04
$\beta$ -NA (0.1 wt%)/PPR	1109.0±33.8	48.0±2.6	80.5±16.1	9.71±0.38
$\beta$ -NA (0.2 wt%)/PPR	1101.1±37.7	47.0±1.4	91.3±18.1	9.84±0.37
$\beta$ -NA (0.3 wt%)/PPR	1102.8±30.1	49.0±2.1	91.5±24	10.88±0.78
$\beta$ -NA (0.5 wt%)/PPR	1110.5±31.6	45.7±2.3	175.9±73	11.01±0.73
0.5 wt% CaCO <sub>3</sub> /PPR	1057.4±16.8	48.0±1.1	123.6±26.8	14.15±1.86
1.0 wt% CaCO <sub>3</sub> /PPR	1059.3±18.0	47.7±0.3	120.8±21.4	13.78±1.94
2.0 wt% CaCO <sub>3</sub> /PPR	1094.1±49.9	49.3±1.1	119.9±46.7	13.59±2.37
4.0 wt% CaCO <sub>3</sub> /PPR	1068.9±47.1	48.0±1.0	116.7±20.6	13.19±1.79
Nano-CaCO <sub>3</sub> (0.5 wt%)/ $\beta$ -NA (0.1 wt%)/PPR	1133.4±24.5	48.7±0.9	89.0±9.8	10.96±0.93
Nano-CaCO <sub>3</sub> (1.0 wt%)/ $\beta$ -NA (0.1 wt%)/PPR	1116.2±24.4	50.7±1.7	87.8±15.3	10.77±1.39
Nano-CaCO <sub>3</sub> (2.0 wt%)/ $\beta$ -NA (0.1 wt%)/PPR	1099.1±9.4	50.3±0.9	79.3±27.5	10.65±0.60
Nano-CaCO <sub>3</sub> (4.0 wt%)/ $\beta$ -NA (0.1 wt%)/PPR	1105.8±33.4	51.5±0.4	102.7±11.8	12.09±1.92

stances due to poor interfacial adhesion. The case resembles flexible polyethylene filled with nano-SiO<sub>2</sub> [40], and the deterioration effect counteracts the toughening effect of  $\beta$ -crystal.

It is interesting to see that when the impact tests are conducted at  $-10^{\circ}\text{C}$ , the measured impact strengths of  $\beta$ -nucleated PPR are almost the same as that of pristine PPR (Figure 6b). It means that  $\beta$ -phase fails to take effect at low temperature. However, the addition of nano-CaCO<sub>3</sub> improves the low-temperature notched impact strength of PPR, and nano-CaCO<sub>3</sub>/ $\beta$ -nucleated PPR possesses higher notched impact strength in the case of 4.0 wt% nano-CaCO<sub>3</sub>. In general, higher loading of nanoparticles would lead to poor dispersion in polymer [41], which disfavors enhancement of room temperature mechanical properties of polymer. Here the abnormal increase in impact strength should be correlated to low temperature characteristics of the composites. Although macromolecular mobility is significantly decreased at  $-10^{\circ}\text{C}$  as compared to room temperature, the agglomerated nano-CaCO<sub>3</sub> particles might play the role of sandbags [42]. When impact force is applied, relative slip between the nanoparticles inside the agglomerates would take place, which consumes the certain amount of the input mechanical energy. This in turn explains the composites with low nano-CaCO<sub>3</sub> content do not show higher impact strength. Figure 7 gives the results of short-term creep behaviours of PPR and its composites measured at  $70^{\circ}\text{C}$ . We can see that  $\beta$ -nucleated PPR has higher creep strain than pristine PPR, but nano-CaCO<sub>3</sub>/ $\beta$ -nucleated PPR possesses lower creep strain. The increased creep resistance should result from the hindrance effect of the nanoparticles to polymer chains move-



**Figure 7.** Creep behaviors of PPR and its composites tested at  $70^{\circ}$  under the stress of 1 MPa

ment [43]. From a practical point of view, PPR integrated with high temperature creep resistance would extend its service stability in hot water supply and heating pipe system.

#### 4. Conclusions

For purposes of tuning properties of PPR,  $\beta$ -nucleated PPR and nano-CaCO<sub>3</sub>/ $\beta$ -nucleated PPR were prepared by melt compounding. Non-isothermal crystallization and melting behaviors, crystalline morphology and mechanical properties of the materials were investigated. Both  $\beta$ -nucleating agent and nano-CaCO<sub>3</sub>/ $\beta$ -nucleating agent acted as heterogeneous nucleators in PPR, which was the main reason for the increased total crystallization rate of PPR. In addition,  $\beta$ -nucleating agent and nano-CaCO<sub>3</sub> have synergistic effects on  $\beta$ -phase formation of PPR. Moreover, crystalline morphology of PPR became a peculiar  $\beta\alpha$  twin structure made of  $\beta$ -crystal core and  $\alpha$ -spherulites outgrowths due to the suitable crystallization temperature and dual nucleating ability of nucleating agent. Compared to pristine PPR,  $\beta$ -nucleated PPR exhibited higher elongation to break and area under tensile stress-strain curve, but lower Young's modulus and tensile strength. By adding nano-CaCO<sub>3</sub> particles into  $\beta$ -nucleated PPR, balanced properties can be obtained. Moreover, the composites of nano-CaCO<sub>3</sub>/ $\beta$ -nucleated PPR possessed improved low temperature impact toughness and high temperature creep resistance.

#### Acknowledgements

The authors are grateful for the support of the Natural Science Foundation of China (Grant: 51173207), Sino-Hungarian Scientific and Technological Cooperation Project (Grant: 2009DFA52660), the Natural Science Foundation of Guangdong, China (Grant: 2010B010800020) and Key Laboratory for Nonmetallic Composites and Functional Materials of Sichuan Province (Grant: 2410zxfk24).

#### References

- [1] Harding G. W., van Reenen A. J.: Fractionation and characterisation of propylene-ethylene random copolymers: Effect of the comonomer on crystallisation of poly(propylene) in the  $\gamma$ -phase. *Macromolecular Chemistry and Physics*, **207**, 1680–1690 (2006). DOI: [10.1002/macp.200600242](https://doi.org/10.1002/macp.200600242)
- [2] Stephens C. H., Poon B. C., Ansems P., Chum S. P., Hiltner A., Baer E.: Comparison of propylene/ethylene copolymers prepared with different catalysts. *Journal of Applied Polymer Science*, **100**, 1651–1658 (2006). DOI: [10.1002/app.23788](https://doi.org/10.1002/app.23788)

- [3] Tjong S. C., Shen J. S., Li R. K. Y.: Impact fracture toughness of  $\beta$ -form polypropylene. *Scripta Metallurgica et Materialia*, **33**, 503–508 (1995).  
DOI: [10.1016/0956-716X\(95\)00225-K](https://doi.org/10.1016/0956-716X(95)00225-K)
- [4] Karger-Kocsis J., Varga J., Ehrenstein G. W.: Comparison of the fracture and failure behaviour of injection moulded  $\alpha$ - and  $\beta$ -polypropylene in high-speed three-point bending tests. *Journal of Applied Polymer Science*, **64**, 2059–2066 (1997).  
DOI: [10.1002/\(SICI\)1097-4628\(19970613\)64:11<2057::AID-APP1>3.0.CO;2-I](https://doi.org/10.1002/(SICI)1097-4628(19970613)64:11<2057::AID-APP1>3.0.CO;2-I)
- [5] Karger-Kocsis J., Varga J.: Effects of  $\beta$ - $\alpha$  transformation on the static and dynamic tensile behavior of isotactic polypropylene. *Journal of Applied Polymer Science*, **62**, 291–300 (1996).  
DOI: [10.1002/\(SICI\)1097-4628\(19961010\)62:2<291::AID-APP4>3.0.CO;2-S](https://doi.org/10.1002/(SICI)1097-4628(19961010)62:2<291::AID-APP4>3.0.CO;2-S)
- [6] Varga J., Ehrenstein G. W., Schlarb A. K.: Vibration welding of alpha and beta isotactic polypropylenes: Mechanical properties and structure. *Express Polymer Letters*, **2**, 148–156 (2008).  
DOI: [10.3144/expresspolymlett.2008.20](https://doi.org/10.3144/expresspolymlett.2008.20)
- [7] Grein C.: Toughness of neat, rubber modified and filled  $\beta$ -nucleated polypropylene: From fundamentals to applications. *Advances in Polymer Science*, **188**, 43–104 (2005).  
DOI: [10.1007/b136972](https://doi.org/10.1007/b136972)
- [8] Fujiyama M.: Structures and properties of injection molding of  $\beta$ -crystal nucleator-added polypropylenes. Part 1. Effect of  $\beta$ -crystal nucleator content. *International Polymer Processing*, **10**, 172–178 (1995).
- [9] Fujiyama M.: Structure and properties of injection moldings of  $\beta$ -crystal nucleator-added polypropylene. Part 2, Effect of MFI of base resin. *International Polymer Processing*, **10**, 251–254 (1995).
- [10] Fujiyama M.: Structures and properties of injection moldings of  $\beta$ -crystal nucleator-added polypropylenes. Part 3. Comparison of nucleating effect between  $\gamma$ -quinacridone and quinacridonequinone. *International Polymer Processing*, **11**, 271–274 (1996).
- [11] Lovinger A. J., Chua J. O., Gryte C. C.: Studies on the  $\alpha$  and  $\beta$  forms of isotactic polypropylene by crystallization in a temperature gradient. *Journal of Polymer Science: Polymer Physics Edition*, **15**, 641–656 (1977).  
DOI: [10.1002/pol.1977.180150405](https://doi.org/10.1002/pol.1977.180150405)
- [12] Yamamoto Y., Inoue Y., Onai T., Doshu C., Takahashi H., Uehara H.: Deconvolution analyses of differential scanning calorimetry profiles of  $\beta$ -crystallized polypropylenes with synchronized X-ray measurements. *Macromolecules*, **40**, 2745–2750 (2007).  
DOI: [10.1021/ma062784s](https://doi.org/10.1021/ma062784s)
- [13] Leugering H. J., Kirsch G.: Beeinflussung der Kristallstruktur von isotaktischem Polypropylen durch Kristallisation aus orientierten schmelzen (in German). *Die Angewandte Makromolekulare Chemie*, **33**, 17–23 (1973).  
DOI: [10.1002/apmc.1973.050330102n](https://doi.org/10.1002/apmc.1973.050330102n)
- [14] Varga J., Karger-Kocsis J.: Rules of supermolecular structure formation in sheared isotactic polypropylene melts. *Journal of Polymer Science Part B: Polymer Physics*, **34**, 657–670 (1996).  
DOI: [10.1002/\(SICI\)1099-0488\(199603\)34:4<657::AID-POLB6>3.0.CO;2-N](https://doi.org/10.1002/(SICI)1099-0488(199603)34:4<657::AID-POLB6>3.0.CO;2-N)
- [15] Varga J.:  $\beta$ -modification of isotactic polypropylene: Preparation, structure, processing, properties, and application. *Journal of Macromolecular Science Part B: Physics*, **41**, 1121–1171 (2002).  
DOI: [10.1081/MB-120013089](https://doi.org/10.1081/MB-120013089)
- [16] Lin Y., Chen H., Chan C-M., Wu J.: High impact toughness polypropylene/ $\text{CaCO}_3$  nanocomposites and the toughening mechanism. *Macromolecules*, **41**, 9204–9213 (2008).  
DOI: [10.1021/ma801095d](https://doi.org/10.1021/ma801095d)
- [17] Guo T., Wang L., Zhang A., Cai T.: Effects of nano calcium carbonate modified by a lanthanum compound on the properties of polypropylene. *Journal of Applied Polymer Science*, **97**, 1154–1160 (2005).  
DOI: [10.1002/app.21804](https://doi.org/10.1002/app.21804)
- [18] Zhang X., Shi G.: The effect of a  $\beta$ -nucleator on the crystallization and melting behavior of ethylene/propylene random and block copolymers. *Thermochimica Acta*, **235**, 49–56 (1994).  
DOI: [10.1016/0040-6031\(94\)80082-0](https://doi.org/10.1016/0040-6031(94)80082-0)
- [19] Zhang X., Shi G.: Effect of converting the crystalline form from  $\alpha$  to  $\beta$  on the mechanical properties of ethylene/propylene random and block copolymers. *Polymer*, **35**, 5067–5072 (1994).  
DOI: [10.1016/0032-3861\(94\)90666-1](https://doi.org/10.1016/0032-3861(94)90666-1)
- [20] Sterzynski T., Lambla M., Crozier H., Thomas M.: Structure and properties of nucleated random and block copolymers of propylene. *Advances in Polymer Technology*, **13**, 25–36 (1994).  
DOI: [10.1002/adv.1994.060130102](https://doi.org/10.1002/adv.1994.060130102)
- [21] Varga J., Schulek-Tóth F.: Crystallization, melting and spherulitic structure of  $\beta$ -nucleated random propylene copolymers. *Journal of Thermal Analysis*, **47**, 941–955 (1996).  
DOI: [10.1007/BF01979441](https://doi.org/10.1007/BF01979441)
- [22] Chen H. B., Karger-Kocsis J., Wu J. S., Varga J.: Fracture toughness of  $\alpha$ - and  $\beta$ -phase polypropylene homopolymers and random- and block-copolymers. *Polymer*, **43**, 6505–6514 (2002).  
DOI: [10.1016/S0032-3861\(02\)00590-6](https://doi.org/10.1016/S0032-3861(02)00590-6)
- [23] Juhász P., Varga J., Belina K., Belina G.: Efficiency of  $\beta$ -nucleating agents in propylene/ $\alpha$ -olefin copolymers. *Journal of Macromolecular Science Part B: Physics*, **41**, 1173–1189 (2002).  
DOI: [10.1081/MB-120013090](https://doi.org/10.1081/MB-120013090)
- [24] Xiao W., Feng J.: Comparative investigation on crystallization conditions dependence of polymorphs composition for  $\beta$ -nucleated propylene/ethylene copolymer and propylene homopolymer. *Journal of Applied Polymer Science*, **117**, 3247–3254 (2010).  
DOI: [10.1002/app.32229](https://doi.org/10.1002/app.32229)

- [25] Na B., Lv R., Xu W., Chen R., Zhao Z., Yi Y.: Effect of nucleating duality on the formation of  $\gamma$ -phase in a  $\beta$ -nucleated isotactic polypropylene copolymer. *Polymer International*, **57**, 1128–1133 (2008).  
DOI: [10.1002/pi.2454](https://doi.org/10.1002/pi.2454)
- [26] Varga J.:  $\beta$ -modification of polypropylene and its two-component systems. *Journal of Thermal Analysis and Calorimetry*, **35**, 1891–1912 (1989).  
DOI: [10.1007/BF01911675](https://doi.org/10.1007/BF01911675)
- [27] Varga J., Schulek-Tóth F.: Filled compounds of the  $\beta$ -modification of polypropylene. *Die Angewandte Makromolekulare Chemie*, **188**, 11–25 (1991).  
DOI: [10.1002/apmc.1991.051880102](https://doi.org/10.1002/apmc.1991.051880102)
- [28] Labour T., Vigier G., Séguéla R., Gauthier C., Orange G., Bomal Y.: Influence of the  $\beta$ -crystalline phase on the mechanical properties of unfilled and calcium carbonate-filled polypropylene: Ductile cracking and impact behavior. *Polymer Science Part B: Polymer Physics*, **40**, 31–42 (2002).  
DOI: [10.1002/polb.10068](https://doi.org/10.1002/polb.10068)
- [29] Kotek J., Kelnar I., Baldrian J., Raab M.: Tensile behaviour of isotactic polypropylene modified by specific nucleation and active fillers. *European Polymer Journal*, **40**, 679–684 (2004).  
DOI: [10.1016/j.eurpolymj.2003.12.004](https://doi.org/10.1016/j.eurpolymj.2003.12.004)
- [30] Gahleitner M., Grein C., Bernreitner K.: Synergistic mechanical effects of calcite micro- and nanoparticles and  $\beta$ -nucleation in polypropylene copolymers. *European Polymer Journal*, **48**, 49–59 (2012).  
DOI: [10.1016/j.eurpolymj.2011.10.013](https://doi.org/10.1016/j.eurpolymj.2011.10.013)
- [31] Jeziorny A.: Parameters characterizing the kinetics of the non-isothermal crystallization of poly(ethylene terephthalate) determined by d.s.c. *Polymer*, **19**, 1142–1144 (1978).  
DOI: [10.1016/0032-3861\(78\)90060-5](https://doi.org/10.1016/0032-3861(78)90060-5)
- [32] Turner Jones A., Aizlewood J. M., Beckett D. R.: Crystalline forms of isotactic polypropylene. *Macromolecular Chemistry and Physics*, **75**, 134–158 (1964).  
DOI: [10.1002/macp.1964.020750113](https://doi.org/10.1002/macp.1964.020750113)
- [33] Xiao W., Wu P., Feng J., Yao R.: Influence of a novel  $\beta$ -nucleating agent on the structure, morphology, and nonisothermal crystallization behavior of isotactic polypropylene. *Journal of Applied Polymer Science*, **111**, 1076–1085 (2009).  
DOI: [10.1002/app.29139](https://doi.org/10.1002/app.29139)
- [34] Luo F., Geng C. Z., Wang K., Deng H., Chen F., Fu Q., Na B.: New understanding in tuning toughness of  $\beta$ -polypropylene: The role of  $\beta$ -nucleated crystalline morphology. *Macromolecules*, **42**, 9325–9331 (2009).  
DOI: [10.1021/ma901651f](https://doi.org/10.1021/ma901651f)
- [35] Varga J., Menyhárd A.: Effect of solubility and nucleating duality of *N,N'*-dicyclohexyl-2,6-naphthalenedicarboxamide on the supermolecular structure of isotactic polypropylene. *Macromolecules*, **40**, 2422–2431 (2007).  
DOI: [10.1021/ma062815j](https://doi.org/10.1021/ma062815j)
- [36] Zhang Z., Chen C., Wang C., Zhang J., Mai K.: A novel highly efficient  $\beta$ -nucleating agent for polypropylene using nano-CaCO<sub>3</sub> as a support. *Polymer International*, **59**, 1199–1204 (2010).  
DOI: [10.1002/pi.2847](https://doi.org/10.1002/pi.2847)
- [37] Výchopňová J., Habrová V., Čabla R., Obadal M., Čermák R.: The effect of  $\beta$ -nucleation on crystallization behavior of isotactic polypropylene. *Proceeding of the 8<sup>th</sup> Polymers for Advanced Technologies International Symposium. Budapest, Hungary* p.2 (2005).
- [38] Varga J.: Supermolecular structure of isotactic polypropylene. *Journal of Materials Science*, **27**, 2557–2579 (1992).  
DOI: [10.1007/BF00540671](https://doi.org/10.1007/BF00540671)
- [39] Varga J., Fujiwara Y., Ille A.:  $\beta\alpha$ -bifurcation of growth during the stepwise crystallization of polypropylene. *Periodica Polytechnica Chemical Engineering*, **34**, 255–271 (1990).
- [40] Zhang M. Q., Rong M. Z., Zhang H. B., Friedrich K.: Mechanical properties of low nano-silica filled high density polyethylene composites. *Polymer Engineering and Science*, **43**, 490–500 (2003).  
DOI: [10.1002/pen.10040](https://doi.org/10.1002/pen.10040)
- [41] Rong M. Z., Zhang M. Q., Zheng Y. X., Zeng H. M., Walter R., Friedrich K.: Structure–property relationships of irradiation grafted nano-inorganic particle filled polypropylene composites. *Polymer*, **42**, 167–183 (2001).  
DOI: [10.1016/S0032-3861\(00\)00325-6](https://doi.org/10.1016/S0032-3861(00)00325-6)
- [42] Wang X., Sun J., Huang R.: Influence of the compounding route on the properties of polypropylene/nano-CaCO<sub>3</sub>/ethylene–propylene–diene terpolymer tercomponent composites. *Journal of Applied Polymer Science*, **99**, 2268–2272 (2006).  
DOI: [10.1002/app.22767](https://doi.org/10.1002/app.22767)
- [43] Zhou T. H., Ruan W. H., Yang J. L., Rong M. Z., Zhang M. Q., Zhang Z.: A novel route for improving creep resistance of polymers using nanoparticles. *Composites Science and Technology*, **67**, 2297–2302 (2007).  
DOI: [10.1016/j.compscitech.2007.01.015](https://doi.org/10.1016/j.compscitech.2007.01.015)

# Creep of thermoplastic polyurethane reinforced with ozone functionalized carbon nanotubes

Y. Jia<sup>1,2</sup>, Z. M. Jiang<sup>2</sup>, X. L. Gong<sup>1</sup>, Z. Zhang<sup>2,3\*</sup>

<sup>1</sup>CAS Key Laboratory of Mechanical Behavior and Design of Materials, Department of Modern Mechanics, University of Science and Technology of China, 230027 Hefei, China

<sup>2</sup>National Center for Nanoscience and Technology, China, 100190 Beijing, China

<sup>3</sup>Center for Nano and Micro Mechanics, Tsinghua University, 100084 Beijing, China

Received 23 February 2012; accepted in revised form 13 April 2012

**Abstract.** This work focused on the mechanical behavior, especially creep resistance, of thermoplastic polyurethane (TPU) filled with ozone-treated multi-walled carbon nanotubes (MWCNTs). It was found that the ozone functionalization of MWCNTs could improve their dispersion and interfacial adhesion to the TPU matrix as proved by scanning electron microscope and Raman spectrometer. It finally contributed to the enhancement of Young's modulus and yield strength of TPU/MWCNT composites. Moreover, the creep resistance and recovery of MWCNT/TPU composites revealed a significant improvement by incorporating ozone functionalized MWCNTs. The strong interaction between the modified MWCNTs and TPU matrix would enhance the interfacial bonding and facilitate the load transfer, resulting in low creep strain and unrecovered strain.

**Keywords:** nanocomposites, carbon nanotubes, mechanical properties, creep

## 1. Introduction

Thermoplastic polyurethane (TPU) has been widely used due to its good versatility in material properties. The reinforcement of thermoplastic polyurethane has been investigated in many researches to further improve its performance [1–6]. In general, there are two main approaches: one is changing the molecular structure of polyurethane by modifying its three basic building blocks: polyol, diisocyanate and the chain extender. The other is introducing an inorganic filler into the polyurethane matrix. Carbon nanotubes (CNTs) can be considered as a promising filler which has attracted great attention and generated intense research on their properties as well as their composites with polymers [7]. Interests in this extraordinary carbon form are mainly focusing on exceptional mechanical, electrical and ther-

mal properties [8–13]. These properties, in addition to their very high aspect ratio, make nanotubes excellent candidate for novel composite materials. However, there are still several issues in need to be investigated relating to their exceptional properties. Because of their large aspect ratio and high van der Waals interactions, CNTs form easily large agglomerates, which will reduce their positive effect. Meanwhile, the chemical inertness of CNTs is another barrier which will cause poor interfacial interactions between the CNTs and polymer matrix. Recent research has shown that, modifying the surface properties of CNTs can drastically increase the solubility, processability and dispersibility in solvents and materials. The surface modification of CNTs also has a remarkable effect on polymer-CNTs interfacial load transfer and overall bulk rein-

\*Corresponding author, e-mail: [zhong.zhang@nanoctr.cn](mailto:zhong.zhang@nanoctr.cn)  
© BME-PT



forcement. The wet chemical modification is the most common surface modified method to introduce oxygen-containing moieties onto the CNTs surface. However, these oxidation techniques involve a process which would generate certain organic vapors from the solution-phase oxidation methodologies along with the purification procedures. The vapors are harmful to environment and people's health. Thus, these waste vapors require ultimate disposal. In contrast, the environmentally friendly surface modification of CNTs by ozonation is a relatively new method which is not only powerful and convenient with characteristic of high efficiency, but also has easy operation and potentially low cost [14–17]. Byl *et al.* [18] utilized ozone as the oxidative agent to modify the nanotube adsorption properties. Electron microscopy studies indicated that CNT bundles were morphologically modified by the ozone agent. Mawhinney *et al.* [19] studied the gas phase oxidation of CNTs by ozone at room temperature and characterized the change of surface functional groups using Fourier transform infrared spectroscopic (FTIR) method. Simmons *et al.* [20] exposed CNTs to room temperature UV-generated ozone and found it could lead to an irreversible increase in their electrical resistance, which was due to the oxygen-containing functional groups successfully introduced on the sidewalls of the nanotubes. According to our previous study [21], the ozone-treated MWCNTs were prepared at room temperature and epoxy [22] or polycarbonate [23] based composites filled with ozone treated MWCNTs were studied in terms of mechanical properties. In this work, we prepared thermoplastic polyurethane based composites filled with pristine or ozone treated MWCNTs by melt mixing and compared the mechanical properties as well as creep and recovery behavior.

## 2. Experimental methodology

### 2.1. Materials

The pristine MWCNTs (denoted as p-MWCNTs in this paper) were prepared by a chemical vapor deposition method. Their purity is higher than 95 wt%, average diameter is between 10 and 20 nm, and length is between 1 and 10  $\mu\text{m}$ . The MWCNTs were supplied by Bayer MaterialScience AG (Leverkusen, Germany). The TPU's brand name is Elastollan 1185A10 (BASF Corporation, Germany) and its

density is 1.12  $\text{g}/\text{cm}^3$ . Before further functionalization or melt-mixing process, the MWCNTs and TPU were dried at 373 K for 12 hours in a vacuum oven.

### 2.2. Functionalization of MWCNTs

The MWCNTs were functionalized with ozone at room temperature (25°C), which has been discussed in our recent work [21]. Generally, 3 grams of p-MWCNTs were placed into our in-house vertical reactor each time. During the oxidation process, the ozone continuously passed through the reactor chamber and reacted with the MWCNTs for 2 hours. The functionalized MWCNTs are denoted as f-MWCNTs in this paper.

### 2.3. Preparation of nanocomposites

TPU/MWCNT composites were prepared by a two-step melt-mixing strategy to improve the dispersion of fillers. A twin screw extruder (HAAKE-Polylab OS, Haake being part of Thermo Scientific) is employed during the mixing. A masterbatch included 15 wt% of MWCNTs in TPU was prepared firstly. Then the TPU/MWCNT masterbatch was diluted to obtain the target proportion of 3wt%. The screw speed was set to 80 rpm. Several heating temperatures of all barrels of the extruder were applied, and the one gave the best mechanical properties of materials was chosen. After extrusion, the TPU/MWCNT composites were cooled down in a water bath and then were finally granulated with a pelletizer. The pure TPU was extruded under the same conditions for quantitative comparisons with the composites.

### 2.4. Morphological characterization

The dispersion state of MWCNTs in the TPU nanocomposites was studied under a scanning electron microscope (SEM, HITACHI S-4800, Japan). The cryo-fractured surfaces of the tensile loaded specimens were subjected to SEM inspection after gold coated at 6 kV acceleration voltage.

### 2.5. Raman spectroscopy

In order to observe the interface between the TPU matrix and nanotubes, the Raman spectra were obtained by a Renishaw 2000 MicroRaman spectrometer (Renishaw, Wotton-under-Edge, UK) with an excitation length of 633 nm. The TPU/MWCNT samples were put into an obturator in which the

testing temperature can be continuously cooled down from 60 to  $-60^{\circ}\text{C}$  by liquid nitrogen, for the sake of checking the change of compressive stress generated in MWCNTs caused by different temperature-dependent expansion coefficients of nanotubes and TPU matrix. Thermal equilibrium was ensured in all the cases by maintaining the specimen under constant corresponding temperature for 10 min. At least five positions were scanned at each temperature for each sample.

## 2.6. Mechanical measurements

Tensile tests were carried out according to the standard methodology of ASTM D638. The injection molded dog-bone-shaped tensile specimens were applied. The tests were performed using a SANS CMT2000 Tester at a crosshead speed of 50 mm/min at ambient temperature. The Young's modulus, tensile strength and elongation at break were measured and ensemble-averaged values are obtained with at least five specimens of each composition.

## 2.7. Creep and creep-recovery measurements

Creep and creep-recovery tests were conducted in tensile mode under different temperatures and stresses using dynamic mechanical analysis (DMA, Q800, TA Instruments, USA). The creep and recoverable strains were determined as a function of the time. Effects of stress level, recovery period and temperature were investigated as run-time parameters, while creep time is set to constant 300 s. The applied creep stress was 2 MPa and 5 MPa. The recovery time was 300 and 600 s. Three creep-recovery profiles were obtained at temperatures of 35, 80 and  $110^{\circ}\text{C}$ . The specimen size was 13 mm  $\times$  4.3 mm  $\times$  0.4 mm (width  $\times$  length  $\times$  thickness). For each experiment, a new sample was used.

The typical creep-recovery curve of creep tests performed in a tensile configuration was illustrated in Figure 1 [24]. Creep strain  $\varepsilon(t)$  in the viscoelastic range can be described by Equation (1):

$$\varepsilon(t) = \varepsilon_E + \varepsilon_V + \varepsilon_{\infty} \quad (1)$$

where  $\varepsilon_E$  is the elastic creep strain,  $\varepsilon_V$  is the viscoelastic portion of the strain and  $\varepsilon_{\infty}$  is the permanent creep strain. The shear stress  $\tau_0$  is set to zero at  $t_0$  and the unrecovered strain  $\varepsilon_r(t_0, t)$  is measured in this study. In order to further analyze the influence of the stress cycles and carbon nanotubes on the

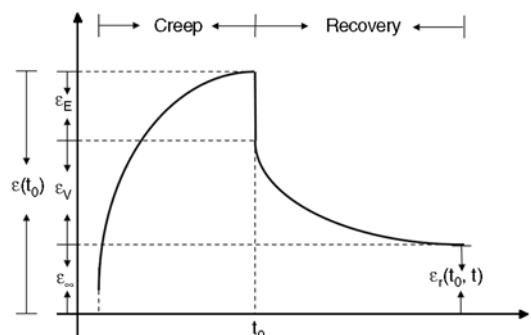


Figure 1. Schematic diagram of a creep-recovery test

recovery performance, the recovery ratio  $X_R$  of a system at time  $t$  is defined as shown in Equation (2):

$$X_R = \frac{\varepsilon(t) - \varepsilon(t_0, t)}{\varepsilon(t_0)} \cdot 100\% \quad (2)$$

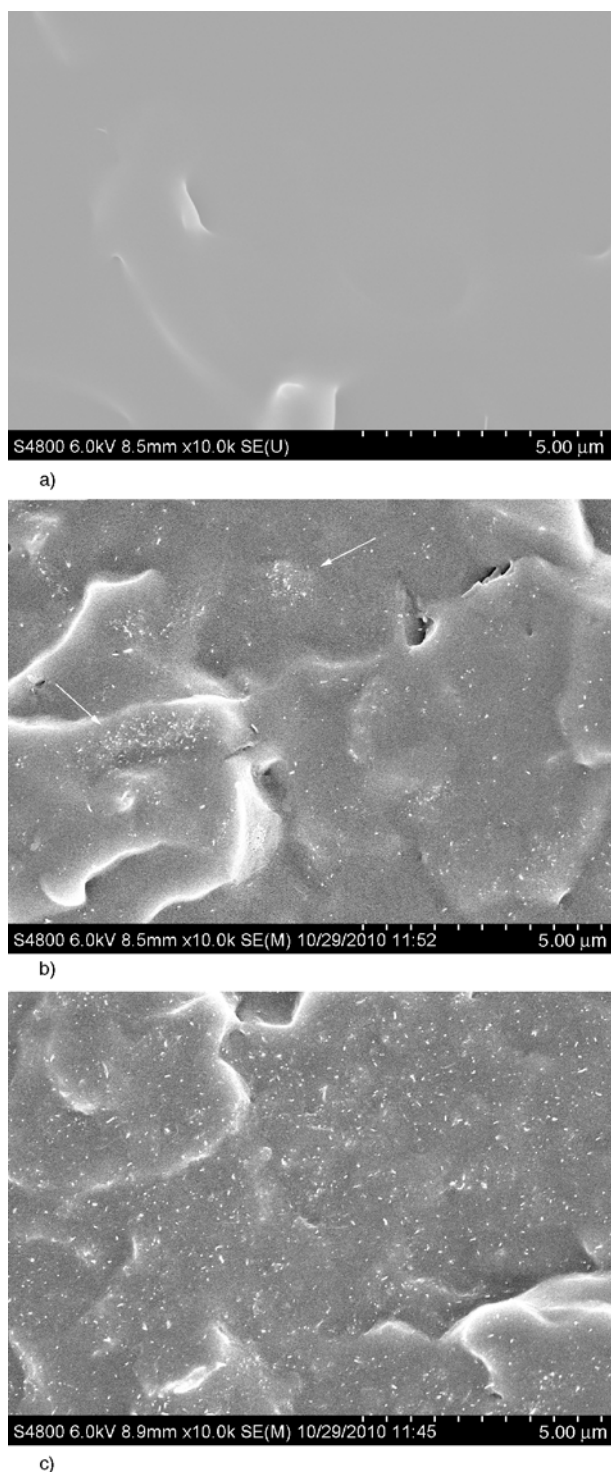
## 3. Results and discussion

### 3.1. Morphology characterization

The homogeneous dispersion of nanotubes in polymer matrices is necessary for making high performance composites. The dispersion state of the materials used in this study is investigated by SEM. Figure 2a is the SEM image of the cryo-fractured surfaces of neat TPU. Figure 2b and 2c are the images of composites containing p-MWCNTs and f-MWCNTs respectively with the content of 3 wt%. In order to characterize the state of distribution, a low magnification was selected to observe the fracture surface, which was perpendicular to the injection direction, of TPU/MWCNTs composites. Comparing with the images of pure matrix, one can clearly observe the presence of carbon nanotubes. Generally speaking, the dispersion is pretty good due to careful mixing. As shown in Figure 2b, however, a few agglomerates labeled by white arrow can be observed, which indicates the dispersion state of TPU/p-MWCNT composite is not perfect. After ozone treatment, there exist some polar groups such  $-\text{OH}$ ,  $-\text{COOH}$  on the surface of MWCNTs, which can improve the dispersion level of MWCNTs as comparing Figure 2c with 2b.

### 3.2. Interface quality between MWCNTs and matrix

Raman spectroscopy can represent the interface quality between CNTs and polymer matrix when the composites are subjected to stress [25–26]. The interaction between CNTs and matrix can be esti-



**Figure 2.** SEM micrographs TPU and TPU/MWCNT nanocomposites: (a) TPU (b) TPU/3.0 wt% p-MWCNT and (c) TPU/3.0 wt% f-MWCNT

mated by the Raman shifts of the characteristic peaks. As well established by former research, the  $G'$ -band was found to be exact and convenient for monitoring the temperature-induced strain of CNTs embedded in the polymer matrix. The spectrum shifts to lower wavenumber when nanotubes are

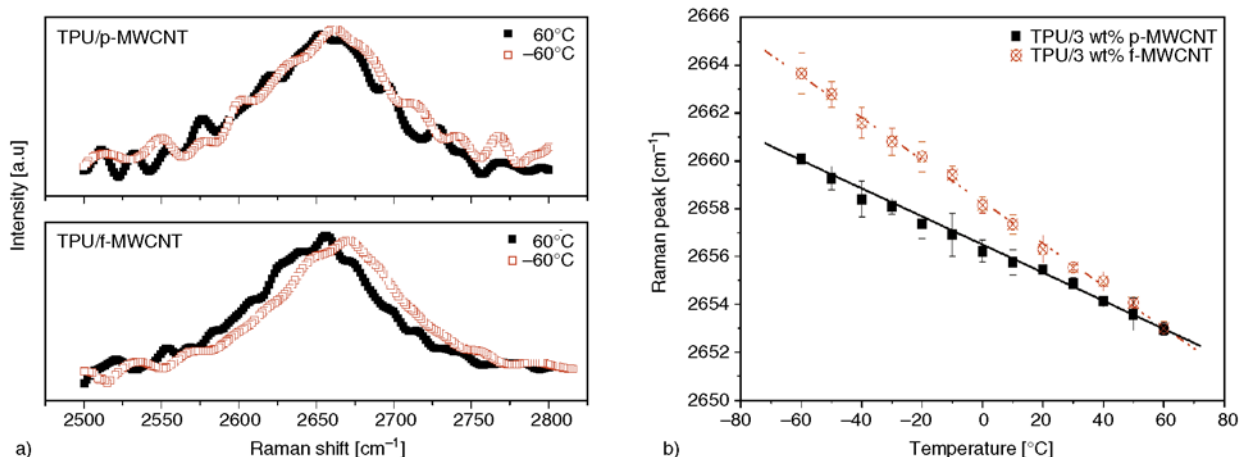
subjected to tension and to higher wavenumber in compressed state. In the present study, we induced a compressive deformation of MWCNTs embedded in the TPU matrix by cooling the specimens from 60 to  $-60^{\circ}\text{C}$  as showed in Figure 3a. Obvious upward shifts of Raman  $G'$ -band peak for the embedded MWCNTs could be seen as the result of compressive stresses from the matrix. Arising from the further shortening of C=C bond also appeared, which is due to the mismatch of thermal expansion coefficients of the MWCNTs and the TPU matrix.

Furthermore, it can be observed that the upward shift of TPU/f-MWCNT composite is more obvious than that of the TPU/p-MWCNT composite (Figure 3a). As shown in Figure 3b, the cooling of the embedded materials from  $60^{\circ}\text{C}$  down to  $-60^{\circ}\text{C}$  caused 7 and  $10\text{ cm}^{-1}$  shift for p-MWCNTs and f-MWCNTs, respectively. Compared with p-MWCNT filled composite, the f-MWCNTs embedded in TPU matrix shows larger  $G'$ -band shift over the temperature range, indicating more efficient load transfer between the f-MWCNTs and the TPU matrix. Thus, we can come to the conclusion that ozone modification can improve the stress transfer from the matrix to the MWCNTs. In other words, the f-MWCNTs have stronger interfacial bonding with TPU matrix in comparison with the p-MWCNTs.

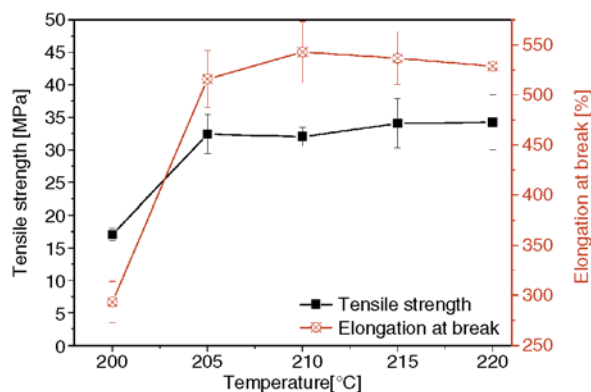
### 3.3. Mechanical properties

As the fundamental properties of material are of primary importance, the tensile properties of the materials at room temperature have been determined. In order to obtain the best mechanical properties of materials, several heating temperatures of the barrels of the extruder were applied. As shown in Figure 4, the temperatures of 200, 205, 210, 215 and  $220^{\circ}\text{C}$  were investigated. The elongation of samples when they are break down raised firstly ( $200\text{--}210^{\circ}\text{C}$ ) and then descended ( $210\text{--}220^{\circ}\text{C}$ ) with the increasing temperature. The tensile strength of TPU matrix was very low at  $200^{\circ}\text{C}$  and remained constant from 205 to  $220^{\circ}\text{C}$  at about 33 MPa. Therefore we chose  $210^{\circ}\text{C}$  as the processing temperature which can ensure the best mechanical properties of the materials.

Table 1 shows the key mechanical properties of TPU and TPU/MWCNTs nanocomposites. The Young's modulus, tensile strength and elongation at break down for the neat TPU are about 18.1 GPa, 32.0 MPa



**Figure 3.** Typical *G'*-band Raman spectra. a) Comparison of the Raman spectra for TPU/p-MWCNT and TPU/f-MWCNT composites with the MWCNT content of 3 wt%; b) the Raman shift of *G'*-band with the testing temperature changed from -60 to 60°C.



**Figure 4.** Mechanical properties of TPU with different process temperatures of barrels in a twin screw extruder

**Table 1.** Tensile mechanical characteristics of the TPU and TPU/MWCNT nanocomposites

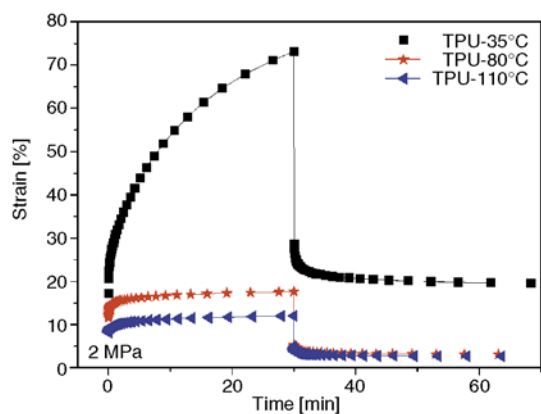
Sample	Young's Modulus [GPa]	Tensile strength [MPa]	Elongation at break [%]
TPU	18.1±3.9	32.0±1.4	542.8±30.6
TPU/3 wt% p-MWCNT	21.0±3.7	35.1±1.4	621.8±16.5
TPU/3wt% f-MWCNT	22.4±0.8	35.5±0.6	622.1±12.2

and 542.8%, respectively. The Young's modulus of the samples rises with increasing MWCNT contents. Addition of 3 wt% p-MWCNTs causes 16% increase in the modulus while the addition of 3 wt% f-MWCNTs increases the value of Young's modulus by 24%. Similar tendency is also observed in the tensile strength as presented in Table 1. The reinforcement efficiency of carbon nanotubes depends on the effect of the intrinsic mechanical properties as well as on the uniform distribution of MWCNTs and matrix-nanofiller interfacial adhesion [27]. The

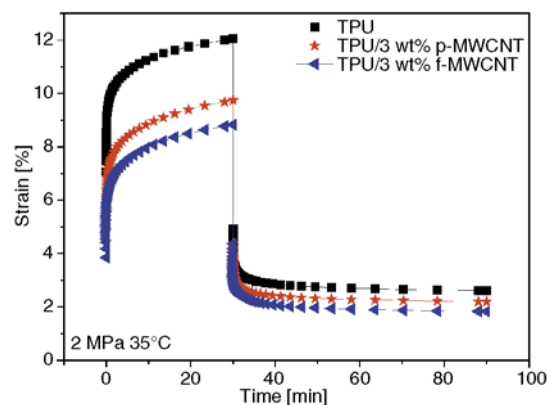
enhancement effect can be recognized in the nanocomposite systems after addition of either p-MWCNTs or f-MWCNTs in terms of the elongation at break. Even though some minor factors such as nanotube type, aspect ratio, weight fraction, dispersion state and testing conditions may affect the properties as well, the significant improvement found in this study strongly supports that ozone functionalization is an effective method to modify the surface of CNTs and to improve the related mechanical properties of TPU matrix.

### 3.4. Creep and recovery behavior

The creep and recovery behavior is studied in different aspects. First, Figure 5 shows the evolution of the creep and recovered strains as a function of time for the neat TPU under three temperature conditions of 35, 80 and 110°C. In this test, 2 MPa was selected as the applied stress within the elastic range. As it is expected, creep strain increased with temperature. While the temperature increased from 35 to 80°C, it is apparent that the creep strain increased from 0.12 to 0.18 (by 45% approximately) at *t* = 30 min. In our recent work [28], we reported the temperature dependence of creep behavior of polypropylene (PP). It was found that the creep strain of PP could increase by almost 900% with the increasing temperature from 50 to 80°C at *t* = 30 min. Comparing experimental result of PP with that of TPU, indicates that the creep property is closely related with intrinsic viscoelastic properties of the materials. In the temperature range from 35 to 80°C, TPU is in the rubber state at all times,



**Figure 5.** Creep-recovery curves of TPU as a function of time at 2 MPa under three different temperature conditions

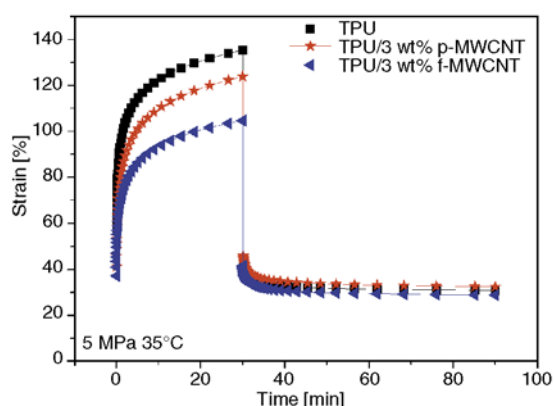


**Figure 6.** Creep-recovery curves of TPU, TPU/p-MWCNT and TPU/f-MWCNT composites at 5 MPa in the temperature condition of 35°C

while PP starts to enter into the glass-rubber transition state around 80°C. Thus, the creep strain of PP changes remarkably in this particular temperature range, whereas TPU responds moderately. When the testing temperature rises to 110°C, the creep strain of TPU exhibits a large increase as shown in Figure 5. It is considered to relate with the softening process of TPU.

Secondly, it is found that temperature has an effect on the elastic property and viscous characteristic of TPU. The evolution of recovered strain as a function of time is also presented in Figure 5. While the elastic creep strain  $\varepsilon_E$  recovers immediately, a small deformation of the viscoelastic and viscous response are observed at 35 and 80°C. The unrecovered strains of TPU are 0.027 and 0.031 ( $t = 3600$  s) at 35 and 80°C respectively, which indicates that the change of recovery property is not sensitive within the testing temperature range of 35 to 80°C. However, a large unrecovered strain could be observed at 110°C, illustrating that the viscous characteristic of TPU would gradually appear under high temperature condition.

Besides different temperatures, various loads were also employed to investigate the creep and recovery behaviors of TPU. The resulting TPU creep profiles under stresses of 2 and 5 MPa at the temperature of 35°C are presented in Figures 6 and 7. It can be seen that the materials showed different responses to varying stress levels. Comparing Figures 6 and 7, one can recognize that the creep strain and unrecovered creep strain increased distinctly with the increasing stress. The averaged creep strain of pure TPU increased from 0.12 to 1.35 when stress increased



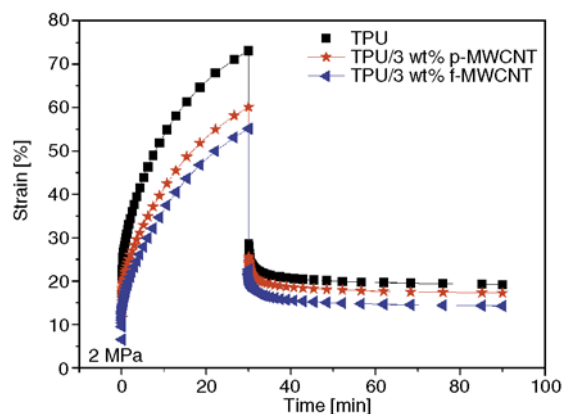
**Figure 7.** Creep-recovery curves of TPU, TPU/p-MWCNT and TPU/f-MWCNT composites at 5 MPa in the temperature condition of 35°C

from 2 to 5 MPa. The ratio of increasing is about 1:11. Similar tendency is also observed for the unrecovered strain  $\varepsilon_r$ , as presented in Figures 6 and 7. The unrecovered strain  $\varepsilon_r$  of TPU increased from 0.03 to 0.31 when stress increased from 2 to 5 MPa. Moreover, the recovery ratio  $X_R$  is also calculated to analyze the recovery property of the materials. However, there are no substantial changes in the recovery ratio of TPU at 2 and 5 MPa (from 21.7% to 21.3%) at  $t = 90$  min.

After characterizing the features of the pure TPU, our attention turned to the effect of the nanotube fillers. The content of nanocomposites is more important than the internal or basic features of the material. The results shown in Figures 6 and 7 also indicated that creep strains of nanocomposites at filler content of 3 wt% were lower than those of the neat matrix under both two test stresses. This implies that the creep behavior is improved by the presence of nanotubes. Under the stress of 5 MPa, for instance,

the strain values of TPU/p-MWCNT and TPU/f-MWCNT composites were reduced by 8.6 and 22.7% compared with it of the neat TPU. It proves that by adding either p-MWCNTs or f-MWCNTs to the TPU matrix, the creep resistance could be improved. The difference between the two nanocomposites, meanwhile, indicates that the properties of PS/f-MWCNT composites are better than PS/p-MWCNT ones under different loading conditions. The recovery properties of composites could also be obtained to investigate the enhancement effect of the two different types of nanotubes. As shown in Figure 7 under high stress condition, there are no substantial changes in the unrecovered strain after addition of either p-MWCNTs or f-MWCNTs, comparing with the pure TPU. On the other hand, the recovery properties shown in Figure 6 under low stress level can be improved by adding nanotubes as unrecovered strain of nanocomposites reduced. The unrecovered strain values of TPU/p-MWCNT and TPU/f-MWCNT composites at 2 MPa were reduced by 16 and 30% compared with neat matrix, respectively. Thus the TPU/f-MWCNT composites have better recovery properties at filler content of 3 wt% than unozonized TPU/p-MWCNT. As the analysis about stress effect mentioned above, it is worth noting that there are different responses of the recovery property of composites under different stress conditions, which is mainly due to the network-like structure formed by the MWCNTs and entangled molecular chain segments. In the two TPU/MWCNTs composites, the network-like structure mixing with nanotubes have good elasticity and recovery feature especially under smaller stress. Moreover, due to the strong interaction between f-MWCNTs and TPU molecular chains, the ozone functionalized nanotubes could further reinforced the composite because the external stresses applied to the composite as a whole can be efficiently transferred to the MWCNTs, allowing the minor content of filler to take a large share of the load in the network-like structure.

For sake of exploring the temperature effect for nanocomposites, the creep and recovery properties of TPU/p-MWCNT and TPU/f-MWCNT composites at 2 MPa in the temperature condition of 110°C were investigated. Compared Figure 8 to Figure 6, it can be seen that the creep strains and unrecovered strains of nanocomposite were much higher at



**Figure 8.** Creep-recovery curves of TPU, TPU/p-MWCNT and TPU/f-MWCNT composites at 2 MPa in the temperature condition of 110°C.

110°C than those at 35°C. However, on the contrary with the strong temperature dependence of pure TPU, the roles of nanotubes acting under both temperatures conditions are similar and the enhancement of nanotubes of creep and recovery properties in TPU matrix is not sensitive with temperature change.

#### 4. Conclusions

Ozone treated MWCNTs filled TPU composites are prepared by diluting a masterbatch containing 15 wt% MWCNTs using melt mixing. The findings highlighted in this paper contribute to our understanding on the efficiency of ozonization of TPU/MWCNT nanocomposites. Some conclusions can be obtained so far:

- 1 The MWCNTs functionalized by ozone showed better dispersion with the TPU matrix as compared to the unmodified ones.
- 2 Significant improvements in Young's modulus and tensile strength of the f-MWCNTs/TPU composites were obtained in comparison with that of p-MWCNTs/TPU composites. Ozone functionalization was an effective method to surface-modify the CNTs and improve the related mechanical properties of TPU matrix.
- 3 The surface modification of MWCNTs obtained by ozone treatment can influence in the creep and recovery property of the nanocomposites in different temperature conditions. The strong interaction between f-MWCNTs and TPU matrix would facilitate the load transfer, resulting in low creep strain and unrecovered strain.

## Acknowledgements

This project was jointly supported by the National Nature Science Foundation of China (Grant No. 51073044), a key international collaboration project (Grant No. 2011DFR50200) of the Ministry of Science and Technology of China, and a key item of the Knowledge Innovation Project of the Chinese Academy of Science (Grant No. KJCX2-YW-M20).

## References

- [1] Nguyen D. A., Lee Y. R., Raghu A. V., Jeong H. M., Shin C. M., Kim B. K.: Morphological and physical properties of a thermoplastic polyurethane reinforced with functionalized graphene sheet. *Polymer International*, **58**, 412–417 (2009).  
DOI: [10.1002/pi.2549](https://doi.org/10.1002/pi.2549)
- [2] Mishra A. K., Mushtaq S., Nando G. B., Chattopadhyay S.: Effect of Cloisite and modified Laponite clays on the rheological behavior of TPU–clay nanocomposites. *Rheologica Acta*, **49**, 865–878 (2010).  
DOI: [10.1007/s00397-010-0458-5](https://doi.org/10.1007/s00397-010-0458-5)
- [3] Lai S-M., Wang C-K., Shen H-F.: Properties and preparation of thermoplastic polyurethane/silica hybrid using sol–gel process. *Journal of Applied Polymer Science*, **97**, 1316–1325 (2005).  
DOI: [10.1002/app.21833](https://doi.org/10.1002/app.21833)
- [4] Koerner H., Liu W., Alexander M., Mirau P., Dowty H., Vaia R. A.: Deformation–morphology correlations in electrically conductive carbon nanotube–thermoplastic polyurethane nanocomposites. *Polymer*, **46**, 4405–4420 (2005).  
DOI: [10.1016/j.polymer.2005.02.025](https://doi.org/10.1016/j.polymer.2005.02.025)
- [5] Jimenez G. A., Jana S. C.: Oxidized carbon nanofiber/polymer composites prepared by chaotic mixing. *Carbon*, **45**, 2079–2091 (2007).  
DOI: [10.1016/j.carbon.2007.05.015](https://doi.org/10.1016/j.carbon.2007.05.015)
- [6] Dan C. H., Lee M. H., Kim Y. D., Min B. H., Kim J. H.: Effect of clay modifiers on the morphology and physical properties of thermoplastic polyurethane/clay nanocomposites. *Polymer*, **47**, 6718–6730 (2006).  
DOI: [10.1016/j.polymer.2006.07.052](https://doi.org/10.1016/j.polymer.2006.07.052)
- [7] Ajayan P. M., Iijima S.: Smallest carbon nanotube. *Nature*, **358**, 23 (1991).  
DOI: [10.1038/358023a0](https://doi.org/10.1038/358023a0)
- [8] Kashiwagi T., Grulke E., Hilding J., Groth K., Harris R., Butler K., Shields J., Kharchenko S., Douglas J.: Thermal and flammability properties of polypropylene/carbon nanotube nanocomposites. *Polymer*, **45**, 4227–4239 (2004).  
DOI: [10.1016/j.polymer.2004.03.088](https://doi.org/10.1016/j.polymer.2004.03.088)
- [9] Koval'chuk A. A., Shchegolikhin A. N., Shevchenko V. G., Nedorezova P. M., Klyamkina A. N., Aladyshev A. M.: Synthesis and properties of polypropylene/multiwall carbon nanotube composites. *Macromolecules*, **41**, 3149–3156 (2008).  
DOI: [10.1021/ma800297e](https://doi.org/10.1021/ma800297e)
- [10] Kim M., Mun S. C., Lee C. S., Lee M. H., Son Y., Park O. O.: Electrical and rheological properties of polyamide 6,6/ $\gamma$ -ray irradiated multi-walled carbon nanotube composites. *Carbon*, **49**, 4024–4030 (2011).  
DOI: [10.1016/j.carbon.2011.05.044](https://doi.org/10.1016/j.carbon.2011.05.044)
- [11] Yuan J-M., Fan Z-F., Chen X-H., Chen X-H., Wu Z-J., He L-P.: Preparation of polystyrene–multiwalled carbon nanotube composites with individual-dispersed nanotubes and strong interfacial adhesion. *Polymer*, **50**, 3285–3291 (2009).  
DOI: [10.1016/j.polymer.2009.04.065](https://doi.org/10.1016/j.polymer.2009.04.065)
- [12] Sarno M., Gorrasi G., Sannino D., Sorrentino A., Ciambelli P., Vittoria V.: Polymorphism and thermal behaviour of syndiotactic poly(propylene)/carbon nanotube composites. *Macromolecular Rapid Communications*, **25**, 1963–1967 (2004).  
DOI: [10.1002/marc.200400344](https://doi.org/10.1002/marc.200400344)
- [13] Tjong S. C., Liang G. D., Bao S. P.: Electrical behavior of polypropylene/multiwalled carbon nanotube nanocomposites with low percolation threshold. *Scripta Materialia*, **57**, 461–464 (2007).  
DOI: [10.1016/j.scriptamat.2007.05.035](https://doi.org/10.1016/j.scriptamat.2007.05.035)
- [14] Li M., Boggs M., Beebe T. P., Huang C.: Oxidation of single-walled carbon nanotubes in dilute aqueous solutions by ozone as affected by ultrasound. *Carbon*, **46**, 466–475 (2008).  
DOI: [10.1016/j.carbon.2007.12.012](https://doi.org/10.1016/j.carbon.2007.12.012)
- [15] Banerjee S., Wong S. S.: Rational sidewall functionalization and purification of single-walled carbon nanotubes by solution-phase ozonolysis. *Journal of Physical Chemistry B*, **106**, 12144–12151 (2002).  
DOI: [10.1021/jp026304k](https://doi.org/10.1021/jp026304k)
- [16] Cai L., Bahr J. L., Yao Y., Tour J. M.: Ozonation of single-walled carbon nanotubes and their assemblies on rigid self-assembled monolayers. *Chemistry of Materials*, **14**, 4235–4241 (2002).  
DOI: [10.1021/cm020273o](https://doi.org/10.1021/cm020273o)
- [17] Sham M-L., Kim J-K.: Surface functionalities of multi-wall carbon nanotubes after UV/ozone and TETA treatments. *Carbon*, **44**, 768–777 (2006).  
DOI: [10.1016/j.carbon.2005.09.013](https://doi.org/10.1016/j.carbon.2005.09.013)
- [18] Byl O., Liu J., Yates Jr. J. T.: Etching of carbon nanotubes by ozone – A surface area study. *Langmuir*, **21**, 4200–4204 (2005).  
DOI: [10.1021/la040132w](https://doi.org/10.1021/la040132w)
- [19] Mawhinney D. B., Naumenko V., Kuznetsova A., Yates Jr. J. T., Liu J., Smalley R.: Infrared spectral evidence for the etching of carbon nanotubes: Ozone oxidation at 298 K. *Journal of the American Chemical Society*, **122**, 2383–2384 (2000).  
DOI: [10.1021/ja994094s](https://doi.org/10.1021/ja994094s)
- [20] Simmons J. M., Nichols B. M., Baker S. E., Marcus M. S., Castellini O. M., Lee C-S., Hamers R. J., Eriksson M. A.: Effect of ozone oxidation on single-walled carbon nanotubes. *Journal of Physical Chemistry B*, **110**, 7113–7118 (2006).  
DOI: [10.1021/jp0548422](https://doi.org/10.1021/jp0548422)

- [21] Peng K., Liu L-Q., Li H., Meyer H., Zhang Z.: Room temperature functionalization of carbon nanotubes using an ozone/water vapor mixture. *Carbon*, **49**, 70–76 (2011).  
DOI: [10.1016/j.carbon.2010.08.043](https://doi.org/10.1016/j.carbon.2010.08.043)
- [22] Tang L-C., Zhang H., Han J-H., Wu X-P., Zhang Z.: Fracture mechanisms of epoxy filled with ozone functionalized multi-wall carbon nanotubes. *Composites Science and Technology*, **72**, 7–13 (2011).  
DOI: [10.1016/j.compscitech.2011.07.016](https://doi.org/10.1016/j.compscitech.2011.07.016)
- [23] Zhang Z., Peng K., Chen Y.: Mechanical performance of ozone functionalized MWCNTs/PC nanocomposites. *Express Polymer Letters*, **5**, 516–525 (2011).  
DOI: [10.3144/expresspolymlett.2011.50](https://doi.org/10.3144/expresspolymlett.2011.50)
- [24] Ward I. M.: *Mechanical properties of solid polymers*. Wiley, Weinheim (1983).
- [25] Kao C. C., Young R. J.: A Raman spectroscopic investigation of heating effects and the deformation behaviour of epoxy/SWNT composites. *Composites Science and Technology*, **64**, 2291–2295 (2004).  
DOI: [10.1016/j.compscitech.2004.01.019](https://doi.org/10.1016/j.compscitech.2004.01.019)
- [26] Cooper C. A., Young R. J., Halsall M.: Investigation into the deformation of carbon nanotubes and their composites through the use of Raman spectroscopy. *Composites Part A: Applied Science and Manufacturing*, **32**, 401–411 (2001).  
DOI: [10.1016/S1359-835X\(00\)00107-X](https://doi.org/10.1016/S1359-835X(00)00107-X)
- [27] Ma H., Zeng J., Realff M. L., Kumar S., Schiraldi D. A.: Processing, structure, and properties of fibers from polyester/carbon nanofiber composites. *Composites Science and Technology*, **63**, 1617–1628 (2003).  
DOI: [10.1016/S0266-3538\(03\)00071-X](https://doi.org/10.1016/S0266-3538(03)00071-X)
- [28] Jia Y., Peng K., Gong X-L., Zhang Z.: Creep and recovery of polypropylene/carbon nanotube composites. *International Journal of Plasticity*, **27**, 1239–1251 (2011).  
DOI: [10.1016/j.ijplas.2011.02.004](https://doi.org/10.1016/j.ijplas.2011.02.004)



# New crosslinked hydrogels derivatives of 2-hydroxyethyl methacrylate: Synthesis, modifications and properties

B. Podkościelna\*, A. Bartnicki, B. Gawdzik

Department of Polymer Chemistry, Faculty of Chemistry, Maria Curie-Skłodowska University, pl. M. Curie-Skłodowskiej 5, 20-031 Lublin, Poland

Received 8 February 2012; accepted in revised form 16 April 2012

**Abstract.** This paper presents the synthesis, physicochemical properties and modifications of 2-hydroxyethyl methacrylate copolymers. It describes the new 2-hydroxyethyl methacrylate hydrogels in the form of microbeads of different degrees of crosslinking (2, 5, 8, 10, 15 and 20% mol). As crosslinking monomers bis[4(2-hydroxy-3-methacryloyloxypropoxy) phenyl]-sulfide and ethylene glycol dimethacrylate were used. The new hydrogels were obtained by two alternative methods in a suspension copolymerisation procedure. The copolymers were modified with diethylenetriamine in an epoxide opening reaction. Thermal properties (differential scanning calorimetry, thermogravimetric analysis) and swelling characteristic in typical solvents of the obtained functional hydrogels were examined. The chemical structure of the copolymers before and after modification was confirmed by Fourier transform infrared spectroscopy and elemental analyses. Moreover, their sorptive properties in removal of Cu(II), Zn(II), Cd(II), and Pb(II) ions from aqueous solutions were also presented. The Langmuir and Freundlich isotherm models are used to describe the adsorption characteristics of the selected modified hydrogels.

**Keywords:** polymer gels, microbeads, material testing, thermal properties, 2-hydroxyethyl methacrylate

## 1. Introduction

The first mention of hydrogels appeared in 1960 when Wichterle and Lim proposed the use of poly(2-hydroxyethyl methacrylate) in contact lenses [1]. Since then, the use of hydrogels has extended to various applications. Due to their excellent hydrophilic properties, high swelling ratio and biocompatibility, hydrogels have been widely used in agriculture, in biomedicine as antibacterial materials, biosensors and in tissue engineering, in sorbents for the removal of heavy metals, and many other applications [2, 3]. These materials have been also used in the development of the smart drug delivery systems. Hydrogels can control drug release by changing the gel structure in response to environmental stimuli and also can protect the drug from hostile environments [4–6].

Hydrogels based on 2-hydroxyethyl methacrylate (HEMA) copolymers are of a widespread interest in biomedical applications. Because of their high water content, hydrogels have a degree of flexibility similar to naturally occurring tissues, which minimises potential irritation to surrounding membranes and tissues [7].

For this reason, pH- and temperature-sensitive hydrogels, based on HEMA and itaconic acid copolymers, were prepared and characterised in order to examine their potential use in biomedical applications [8]. To improve their mechanical properties numerous modifications of p(HEMA) were introduced [9]. The results of these modifications were materials with new physico-chemical properties. Macroporous hydrogels based on HEMA are artificial biomaterials commonly used in tissue engineer-

\*Corresponding author, e-mail: [beatapod@poczta.umcs.lublin.pl](mailto:beatapod@poczta.umcs.lublin.pl)

ing, including central nervous system repair [10]. Novel hydrogels consisting of different molar ratios of 2-hydroxyethyl methacrylate and acrylamide were prepared for specialty applications as sorbents for some common metal ions [11]. Additionally, 2-hydroxyethyl methacrylate and its derivatives are also used in the treatment of eye diseases, and among others for the synthesis of artificial corneas [12–13]. Copolymerisation of sulfur-containing monomers with HEMA lead to the formation of new polymers with high biocompatibility and very good physical and chemical properties [14].

In order to obtain mechanically and thermally resistant hydrogels, their crosslinking is necessary. In our research we used as a crosslinking monomer bis[4(2-hydroxy-3-methacryloyloxypropoxy)phenyl]sulfide (BES.DM) [15] or ethylene glycol dimethacrylate (EGDMA). BES.DM is a very interesting crosslinking monomer having in its construction methacrylic groups, aromatic rings and sulfide group. Our current studies are aimed at obtaining sorbents with reactive functional groups on the surface capable of extensive modifications.

Specific commercially available sorbents are very expensive and have rather selective applications. Our newly obtained sorbent – hydrogel is thermally and chemically resistant, can be stored in surrounding temperature and moreover is low-toxic.

This article includes synthesis new hydrogels based on 2-hydroxyethyl methacrylate as a heavy metal sorbent. The obtained hydrogels were in the form of microbeads of the following degrees of crosslinking: 2, 5, 8, 10, 15 and 20% mol, BES.DM or EGDMA. Additionally, these hydrogels were obtained in two alternative procedures. The selected hydrogels were modified with diethylenetriamine in the epoxide opening reaction. Studies of thermal stability, swelling characteristics and sorption were carried out. The structures of the hydrogels before and after modification were confirmed by FTIR and elemental analysis.

Their sorptive properties in removal of Cu(II), Zn(II), Cd(II) and Pb(II) ions from aqueous solutions were also presented. The adsorption characteristics (by used the Langmuir and Freundlich isotherm models) and kinetics test results of selected modified hydrogels were studied.

## 2. Experimental

### 2.1. Chemicals and eluents

2-Hydroxyethyl methacrylate (HEMA) and ethylene glycol dimethacrylate (EGDMA) decan-1-ol were from Fluka AG (Buchs, Switzerland);  $\alpha,\alpha'$ -Azoiso-bis-butyronitrile (AIBN) and poly(vinyl pyrrolidone) (PVP; K90) were obtained from Merck (Darmstadt, Germany). Reagent grade acetone, methanol, propan-2-ol, chlorobenzene, chloroform, hexane, toluene, tetrahydrofurane (THF), methyl methylene, 1,4-dioxane, 2-(chloromethyl)oxirane (EP) and sodium hydroxide (NaOH) were from POCh (Gliwice, Poland). Bis[4(2-hydroxy-3-methacryloyloxypropoxy)phenyl]sulfide (BES.DM) was obtained by the procedure described in our previous work [15].

Aqueous solution of  $\text{CuCl}_2 \cdot 2\text{H}_2\text{O}$ ,  $\text{ZnCl}_2$ ,  $\text{Cd}(\text{NO}_3)_2 \cdot 4\text{H}_2\text{O}$  and  $\text{Pb}(\text{NO}_3)_2$  were used as sources of Cu(II), Zn(II), Cd(II) and Pb(II) respectively. The stock solution was further diluted to the required experimental concentration. Other chemicals used were of analytical grade.

### 2.2. Synthesis of hydrogels

#### 2.2.1. Synthesis of BES.DM-HEMA and EGDMA-HEMA and their modifications

The experimental parameters of the syntheses of the copolymers are presented in Table 1.

The dispersion medium was prepared through the dissolution of 1 wt% poly(vinyl pyrrolidone) in deionised water ( $150 \text{ cm}^3$ ). The synthesis was carried out in a three-necked flask equipped with a stirrer, a water condenser and a thermometer. The initiator AIBN (1.5 wt%) was dissolved in the monomers, and then the mixture of BES.DM and HEMA or EGDMA and HEMA was diluted with a mixed solvent ( $8 \text{ cm}^3$  toluene/ $8 \text{ cm}^3$  decan-1-ol). The reaction mixture was stirred at 350 rpm for 12 h at  $80^\circ\text{C}$ . The obtained copolymers were washed with distilled water, filtered off, dried and extracted (ace-

**Table 1.** Experimental parameters of the synthesis

AIBN	PVP	HEMA	EHEMA	Crosslinker (20% mol)	
				BES.DM	EGDMA
[g]					
0.249	1.50	–	10	6.66	–
0.265	1.50	10	–	7.72	–
0.206	1.50	10	–	–	3.76

tone and methanol) in a Soxhlet apparatus. After drying in air, copolymers were fractionated with sieves. The applied polymerisation conditions yielded about 80% beads in the range of 40–80  $\mu\text{m}$ .

#### *Modification with 2-(chloromethyl)oxirane*

The selected BES.DM-HEMA and EGDMA-HEMA copolymers were modified with 2-(chloromethyl)oxirane. In a 250  $\text{cm}^3$  round bottomed three-necked flask equipped with a mechanical stirrer, a thermometer and a dropper of 10 g of selected beads was placed together with 80 mL 2-(chloromethyl)oxirane and 60 mL of propan-2-ol and the whole content was heated over a water bath at 70°C. Then, at the same temperature 10 mL of 13.5% solution of NaOH were added during 5 minutes. After 15 minutes another portion (50 mL) of 13.5% solution of NaOH was added and the stirring was continued for 60 minutes. The obtained modified beads were filtered off, washed with aqueous methanol, next filtered off and dried.

#### *Modification with DETA*

In a 250  $\text{cm}^3$  round-bottomed two-necked flask equipped with a mechanical stirrer and a thermometer, 10 g of selected microspheres (BES.DM-HEMA-EP or EGDMA-HEMA-EP) was placed together with 10 mL diethylenetriamine (DETA) and 150 mL of toluene and the whole content was mixed at room temperature for 2 h. Next, it was heated over a water bath at 80°C for 3 h and finally at room temperature for 24 h. The obtained modified microbeads were washed with distilled water, filtered off, dried and extracted in a Soxhlet apparatus with boiling acetone for 5 h. Finally, the product was dried under reduced pressure at 30°C [16].

### **2.2.2. Synthesis of EHEMA and BES.DM-EHEMA**

In a 250  $\text{cm}^3$  round-bottomed three-necked flask equipped with a mechanical stirrer, thermometer and dropper: 0.3 mole HEMA, 1.5 mole 2-(chloromethyl)oxirane, and 85 mL of propan-2-ol were placed and the whole content was heated over a water bath at 70°C. Then, at the same temperature, 20 mL of 13.5% solution of NaOH were added during 10 minutes. After 30 minutes another portion of 13.5% solution of NaOH was added and the stirring was continued for 60 minutes. When the reaction was over, the

content of the flask was placed into the dropper, the water layer was separated, and the organic layer was distilled at low pressure (1.6 kPa) in order to separate 2-propanol and the excess of 2-(chloromethyl)oxirane. The remaining 2-(chloromethyl)oxirane and water were distilled at low pressure after 50 mL of toluene was added into it. The obtained epoxide compound was filtered off. The main reaction product was a methacrylate (2,3-epichlorohydrin)ethyl.

#### *Copolymerisation*

The dispersion medium was prepared through the dissolution of 1 wt% poly(vinyl pyrrolidone) in deionised water (150  $\text{cm}^3$ ). In a 250  $\text{cm}^3$  round-bottomed three-necked flask equipped with a mechanical stirrer, thermometer and water condenser, EHEMA was placed together with BES.DM and AIBN (polymerization initiator), then the mixture was diluted with a mixed solvent (8  $\text{cm}^3$  toluene/ 8  $\text{cm}^3$  decan-1-ol) (Table 1). The reaction was stirred at 350 rpm for 12 h at 80°C. The obtained hydrogels were washed and filtered off according to the procedure presented previously. Next, the obtained microbeads with the pending epoxide groups were modified with diethylenetriamine according to the instructions given in Section 2.2.1.

### **3. Characterisation**

Elemental analysis of the parent and modified copolymers was carried out using the Perkin-Elmer CHN 2400 apparatus.

Photos of the hydrogels were obtained using the scanning electron microscope Quanta 3D FEG SEM (FEI Company) with the use of ETD detector in high vacuum.

Fourier transform infrared spectroscopy (FTIR) spectra were recorded using a Perkin-Elmer 1725 X spectrophotometer in the 400–4000  $\text{cm}^{-1}$  wave number range using KBr pallets.

Differential scanning calorimetry (DSC) thermograms were obtained with the use of a DSC Netzsch 204 calorimeter (Netzsch, Günzburg, Germany) operating in a dynamic mode. The dynamic scans were performed at a heating rate of 10  $\text{K}\cdot\text{min}^{-1}$  at two temperature scans. The first scan was performed between 20°C and a maximum of 110°C to remove any adsorb moisture. The second one was conducted in 20–500°C under nitrogen atmosphere (30  $\text{mL}\cdot\text{min}^{-1}$ ). The mass of the sample was ~10 mg.

As a reference, an empty aluminum crucible was used. The glass transition temperature ( $T_g$ ), decomposition temperature ( $T_d$ ), and enthalpy of decomposition ( $\Delta H_d$ ) were evaluated.

Thermogravimetric analysis (TG) was carried out on a Paulik and Erdey derivatograph (Budapest, Hungary) at a heating rate of  $10^\circ\text{C}\cdot\text{min}^{-1}$  in air, in the temperature range of 20 to  $1000^\circ\text{C}$  with the sample weight of 100 mg. As a reference  $\alpha\text{-Al}_2\text{O}_3$  was used. The initial decomposition temperature ( $IDT$ ),  $T_{20\%}$ ,  $T_{50\%}$  of weight loss, final decomposition temperature ( $T_{\text{end}}$ ), and temperature of the maximum rate of weight loss ( $T_1$ ,  $T_2$  and  $T_3$ ) were determined.

The HCl/dioxane method [17] was used to determine the number of epoxy groups ( $L_{\text{EP}}$ ). The epoxide content was calculated from the difference between the blank and that found for the titration of the sample reaction mixture.

The swellability coefficient,  $B$ , was determined by equilibrium swelling in methanol, acetone, toluene, 1,4-dioxane, THF, water, chlorobenzene and hexane. The samples were swollen in a few solvents for 0.5 h. The excess solvents were removed by centrifugal methods [18, 19]. Three specimens were tested for each hydrogels and a mean value was taken.  $B$  is expressed as given by Equation (1):

$$B = \frac{V_s - V_d}{V_d} \cdot 100\% \quad (1)$$

where  $V_s$  is the volume of the copolymer after swelling and  $V_d$  – the volume of the dry copolymer.

### 3.1. Adsorption tests

The adsorption equilibrium measurements in the single component system were carried out at room temperature. 0.2 g of a polymer sample was placed in a 100 mL conical flask containing 20 mL of heavy metal ion solution with the initial concentration ranging from  $1 \cdot 10^{-3}$  to  $25 \cdot 10^{-3}$  M. The pH of the solution was maintained at 5.0 by using nitric(V) acid to avoid metal precipitation using Elmetron CPI-505 pH/ionometer (Poland). The samples were shaken mechanically using the laboratory shaker (ELPHINE, type 357, Poland) for 24 h at 180 rpm. The preliminary experiments showed that equilibrium was reached under this condition. At equilibrium, the concentrations of Cu(II), Zn(II), Cd(II) and Pb(II) in the residual solutions were analysed

by the AAS (Atomic Absorption Spectrometry) measurements using SpectrAA 240FZ (Varian, Australia) at appropriate wavelengths, i.e. 324.7, 213.9, 228.8, and 217.0 nm for copper, zinc, cadmium and lead, respectively.

The adsorption data of the metal ions using the BES.DM-HEMA-EP-DETA sample was analysed according to the Langmuir and Freundlich models [20, 21].

The Langmuir equation has the following form given by Equation (2):

$$q_e = \frac{q_0 K_L c_e}{1 + K_L c_e} \quad (2)$$

where  $c_e$  is the equilibrium concentration of the metal ion [mg/L] and  $q_e$  is the adsorption capacity at equilibrium [mg/g].

Constant  $q_0$  [mg/g] and  $K_L$  [L/mg] are the characteristics of the Langmuir equation and can be determined from its linearised form (plots of  $c_e/q_e$  vs.  $c_e$ ). The Freundlich equation is expressed by Equation (3):

$$q_e = K_F c_e^{1/n} \quad (3)$$

where  $K_F$  is the Freundlich adsorption capacity [mg/g] and  $1/n$  is the Freundlich constant related to the surface heterogeneity. The above equation can be linearised by taking logarithms to find the parameters  $K_F$  and  $n$ .

### 3.2. Kinetic tests

For evaluation the kinetic parameters the most commonly known kinetic expressions that is the pseudo first order kinetic and the pseudo second order kinetic models were used according to the Equations (4) and (5) [22]:

$$\log(q_1 - q_t) = \log(q_1) - \frac{k_1}{2.303} t \quad (4)$$

$$\frac{1}{q_t} = \frac{1}{k_2 q_2^2} + \frac{1}{q_2} t \quad (5)$$

where  $q_t$  is the amount of metal adsorbed at time  $t$  [mg/g],  $q_1$ ,  $q_2$  are the amounts of metal complexes sorbed at equilibrium for the pseudo first order kinetic and the pseudo second order kinetic models [mg/g], respectively,  $k_1$  is the pseudo first order rate constant [1/min] and  $k_2$  is the rate constant of the pseudo second order adsorption [g/(mg·min)].

Based on the plots of  $\log(q_e - q_t)$  vs.  $t$  and  $t/q_t$  vs.  $t$  the kinetic parameters ( $q_1$ ,  $k_1$ ,  $q_2$ ,  $k_2$ ,  $h$ ) were calculated.

#### 4. Results and discussion

Suspension polymerisation of prepared methacrylate monomers with HEMA in the presence of diluents (toluene + decan-1-ol) leads to polymeric hydrogels in form of microbeads. Experimental parameters of representative syntheses are summarised in Table 1.

Copolymerisation process was performed at a variable molar ratio of crosslinking monomers to HEMA (2, 5, 8, 10, 15 and 20% mol.) and constant volume ratio of diluents to monomers (1:1).

The scheme presenting theoretical chemical structures of the obtained new crosslinked hydrogels and

products of their modification with DETA are presented in Figures 1 and 2. Elemental analysis of amine derivatives are presented in Table 2. From these data one can see that the highest percentage of nitrogen was achieved for BES.DM-EDETA (3.59%  $N_{\text{prac}}$ ). The percentage of nitrogen calculated from the number of epoxy group ( $N_{\text{theo}}$ ) is higher than that obtained during the synthesis ( $N_{\text{prac}}$ ). The difference probably results from a connection DETA mainly to the epoxy groups present on the surface of hydrogels.

Unfortunately, the epoxy derivative of EGDMA-HEMA was characterised by a very low number of epoxy groups (0.15 mmol/g, Table 2). As this reaction occurs with a low yield, studies of this derivative were not pursued. For further study copolymers BES.DM-HEMA and BES.DM-EHEMA were

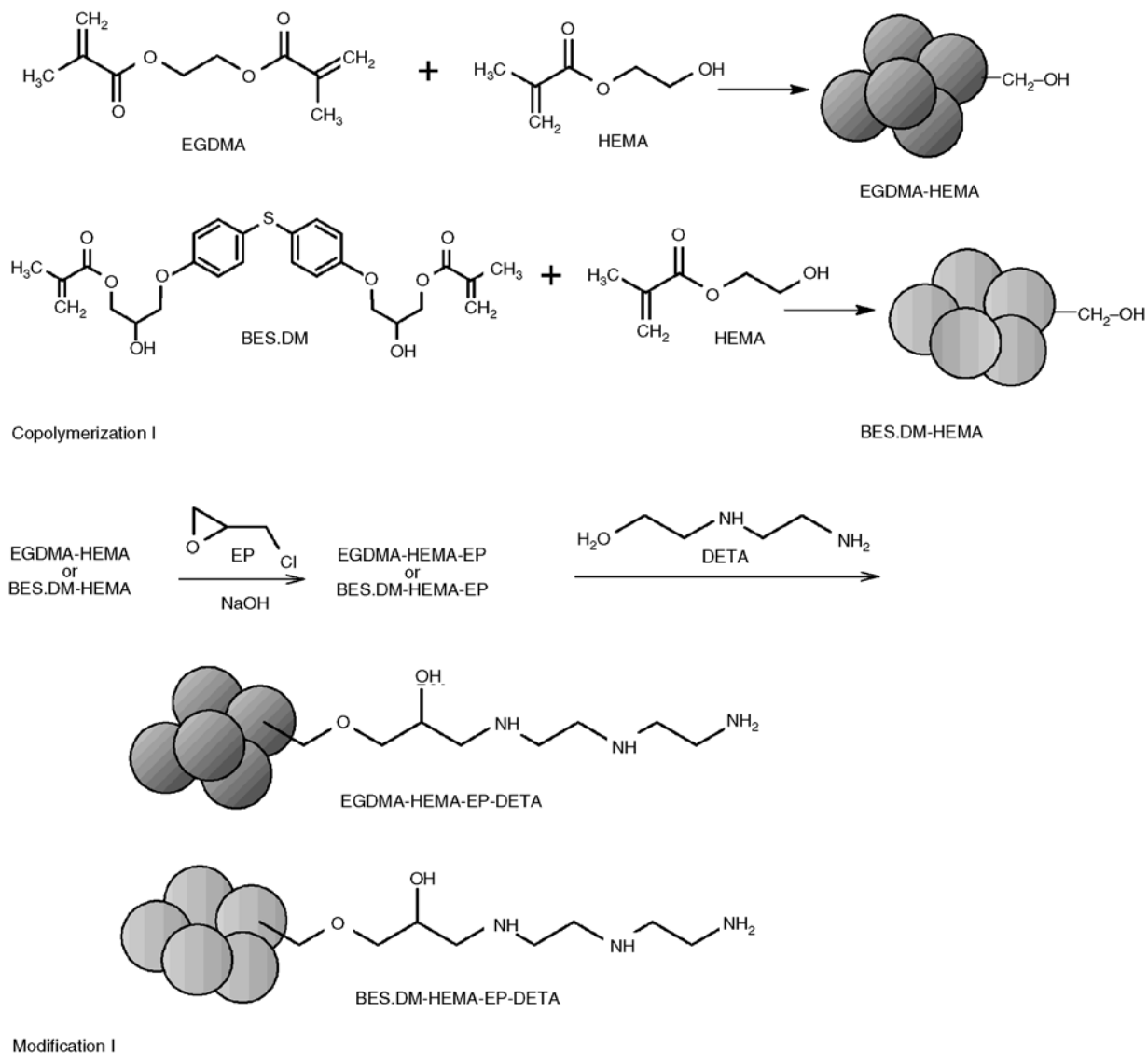


Figure 1. Preparation scheme of HEMA hydrogels

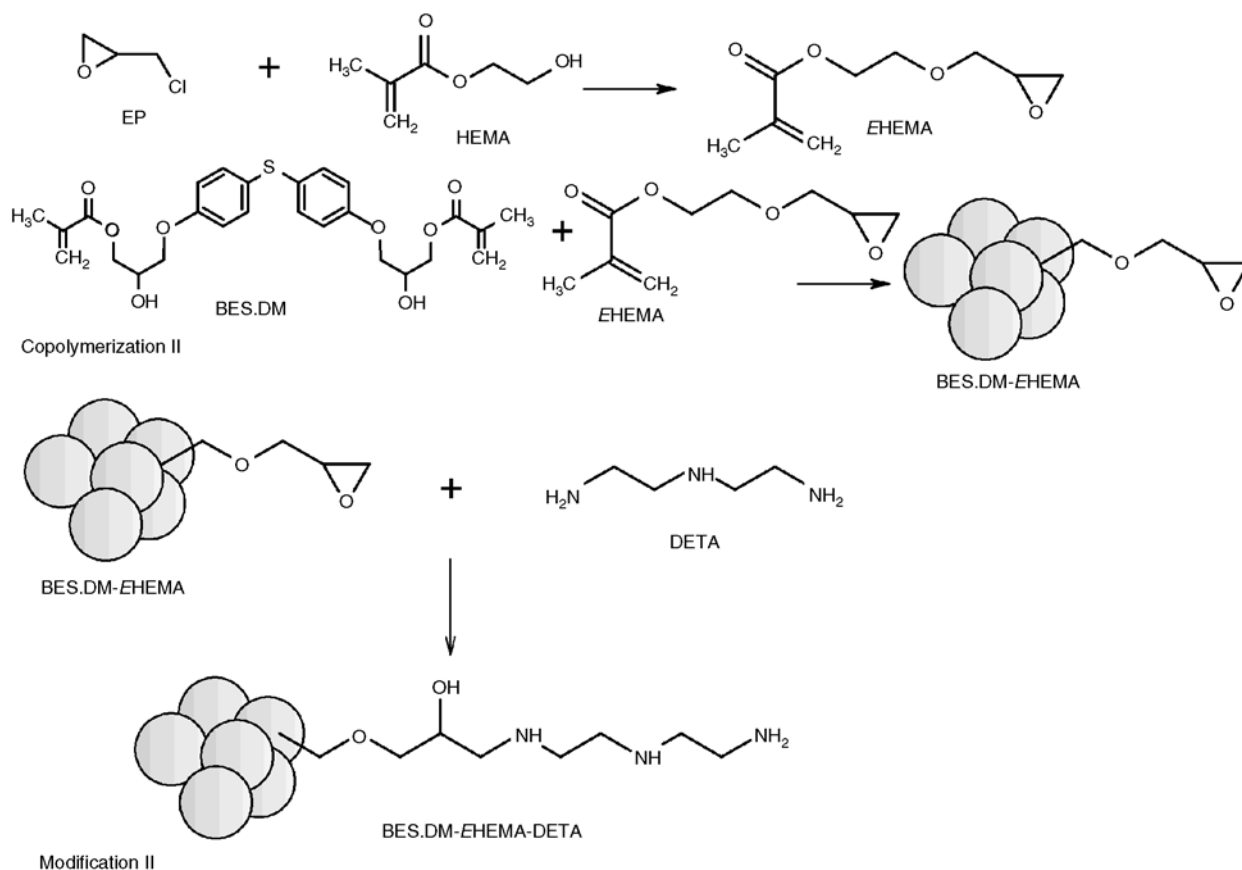


Figure 2. Preparation scheme of EHEMA hydrogel

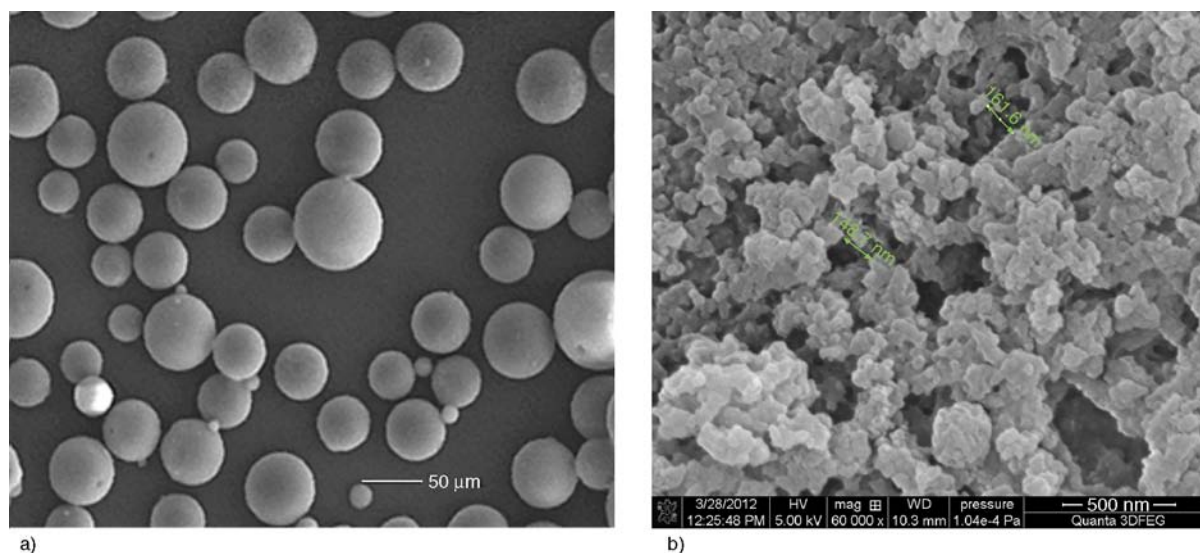


Figure 3. SEM photos, a) BES.DM-EHEMA, b) fragment of surface

Table 2. Elemental analysis of amine derivatives

Copolymer	C <sub>prac</sub>	H <sub>prac</sub>	N [%]		L <sub>EP</sub> of epoxy derivatives [mmol/g]
			N <sub>prac</sub>	N <sub>theo</sub>	
EGDMA-HEMA-EP-DETA	58.52	7.31	0.81	1.86	0.15
BES.DM-HEMA-EP-DETA	57.92	7.63	3.09	6.21	0.60
BES.DM-EHEMA-DETA	57.52	7.17	3.59	7.50	0.74

N<sub>prac</sub> – the percentage of nitrogen obtained in the synthesis

N<sub>theo</sub> – the theoretical percentage of nitrogen

selected which were obtained with a molar ratio of 20% crosslinking monomer. The tests confirmed that the obtained microspheres were characterised by the greatest mechanical stability, which is necessary for further multi-step reactions (after several hours stirring the microbeads keep their spherical shape). The greater the degree of crosslinking, the greater the mechanical stability of hydrogels.

In order to confirm the spherical shape of the obtained hydrogels, two photos were taken by using the scanning electron microscope (SEM). In Figure 3a, hydrogels are presented in a dry state, in Figure 3b the fragment of the surface in higher magnification is visible.

#### 4.1. FTIR

The chemical structures for new HEMA hydrogels and their derivatives were confirmed by FTIR analysis (Table 3 and Figure 4). The results shown in Figure 4 confirmed that modifications of BES.DM-HEMA with 2-(chloromethyl)oxirane and respectively with DETA took place (the presence of epoxy group peak at  $906\text{ cm}^{-1}$ , and then its disappearance).

In the spectrum of the BES.DM-HEMA, C–H stretching vibrations of aromatic ring backbone methyl groups is observed at  $2946\text{ cm}^{-1}$ . The aromatic skeletal absorption is observed at  $1591\text{ cm}^{-1}$ . In the spectrum the vibrations of –OH group are visible at  $3400\text{ cm}^{-1}$ . The signal of C=O group occurs at  $1720\text{ cm}^{-1}$ . In the spectrum BES.DM-HEMA-EP, the epoxide group gives a shape signal at  $906\text{ cm}^{-1}$ . Moreover, in the spectrum BES.DM-HEMA-EP-DETA, C–H stretching vibrations of aromatic ring backbone methyl groups is observed at  $2943\text{ cm}^{-1}$ , the aromatic skeletal at  $159\text{ cm}^{-1}$  and C=O group at  $1721\text{ cm}^{-1}$ .

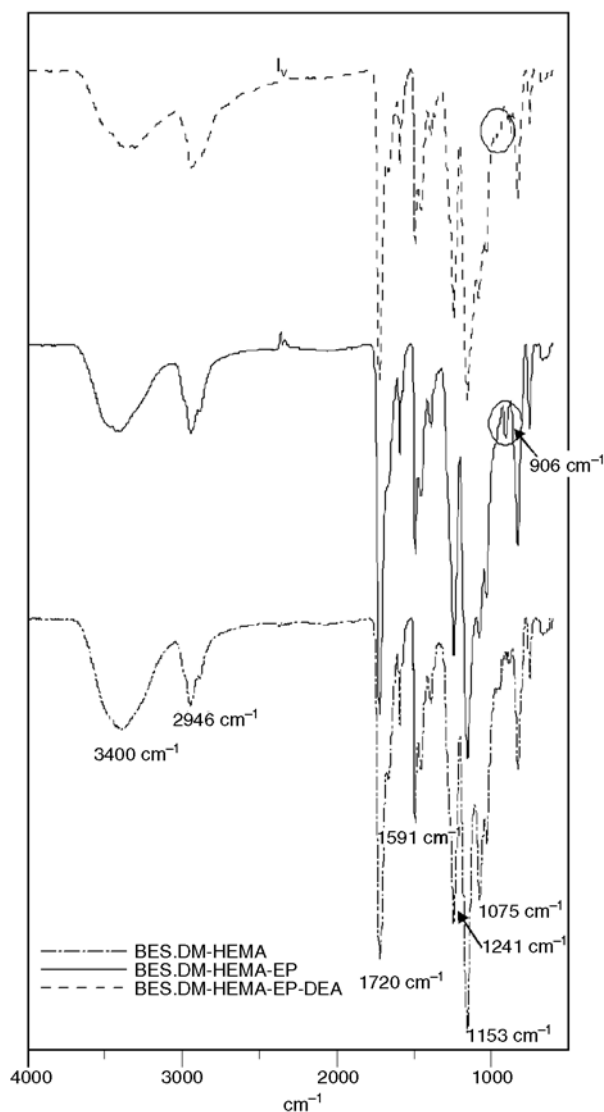

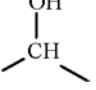

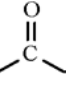


Figure 4. FTIR spectra of the BES.DM-HEMA derivatives

#### 4.2. Swelling properties

The swelling properties of the studied microbeads are presented in Table 4. In all polar solvents the swellability coefficients ( $B$ ) varied from 33.1 to 214%. Significantly higher values of  $B$  in polar solvents compared to those values in non-polar hexane or

Table 3. FTIR analysis

Copolymer	[cm <sup>-1</sup> ]				
					–CH <sub>3</sub>
EGDMA-HEMA	–	3399	–	1719	2945
BES.DM-HEMA	1591	3400	–	1720	2946
BES.DM-HEMA-EP	1591	3400	906	1728	2945
BES.DM-HEMA-EP-DETA	1591	3368	–	1721	2942
BES.DM-EHEMA	1592	3435	906	1722	2946
BES.DM-EHEMA-DETA	1592	3467	–	1721	2943

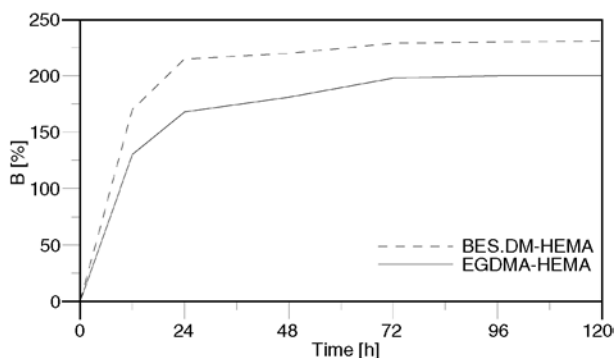
**Table 4.** Swelling studies of obtained copolymers; swellability coefficient – *B*

	Methanol	Acetone	Toluene	THF	Hexane	Chlorobenzene	Water	1,4-Dioxane
BES.DM:HEMA	B [%]							
2%	214.0	67.4	42.3	79.6	43.2	84.4	126.9	80.6
5%	192.4	60.7	37.8	64.9	38.8	76.4	106.6	70.1
8%	173.2	53.4	36.1	49.5	37.8	45.6	102.1	59.6
10%	122.4	38.6	29.8	46.1	33.5	32.2	90.0	54.9
20%	87.3	33.1	25.0	47.5	31.2	24.8	89.2	48.4
EGDMA:HEMA								
2%	97.7	36.3	48.0	66.0	15.0	59.3	75.3	69.3
5%	90.4	35.3	36.4	64.6	15.4	44.7	63.7	63.9
8%	84.5	32.8	39.8	71.9	14.8	44.5	60.4	53.3
10%	82.6	28.3	31.4	50.7	14.6	36.7	50.9	59.0
20%	81.5	23.7	21.8	35.9	11.3	32.5	49.5	40.4
MOD-1	36.7	31.3	11.2	13.3	3.1	6.7	25.0	13.1
MOD-2	32.2	31.1	5.9	6.3	3.0	6.5	18.8	9.4

MOD-1 = BES.DM-HEMA-EP-DETA (20% mol)

MOD-2 = BES.DM-EHEMA-DETA (20% mol)

toluene were observed. Such behaviour is probably due to the presence of polar pendant functional groups (hydroxyl groups) in the chemical structure of copolymers. The highest swellability coefficient is observed for the least crosslinked copolymer. With the increase of crosslinking the swelling of copolymers decreases, ranging in the polar methanol from 214 to 87.3%, respectively. Moreover, BES.DM-HEMA copolymers are characterised by a higher tendency to swell than EGDMA-HEMA copolymers. This is associated with the differences of the chemical structures of BES.DM and EGDMA monomers. BES.DM is a monomer containing aromatic rings, ester groups as well as a sulfur heteroatom in its structure. EGDMA possesses only ester groups in its chemical structure. Due to the spatial structure of the forming nets in the polymerisation process, copolymer BES.DM-HEMA allows better penetration of porogen diluents which are responsible for the formation of a more developed porous structure. Modified microspheres have much less tendency to swell. Probably due to that,

**Figure 5.** The swelling behaviour of hydrogels in water

the hanging amino groups can block easy access of solvent into the hydrogel network.

The swelling behaviour of the studied microspheres in water is presented in Figure 5. From these data one can see that a maximum swelling is received after 24 h and that it does not increase any further. For the studied samples it changes from 160 to 220%.

### 4.3. Thermal properties

The thermal properties of BES.DM-HEMA and EGDMA-HEMA copolymers as well as their amine derivatives were studied by means of DSC and TG analyses. The DSC was performed in a nitrogen atmosphere from 20 to 200°C. The thermogravimetric analysis was conducted in air from 20–1000°C. The weight loss of 20% of copolymer ( $T_{20\%}$ ) for the studied samples changes from 180 to 325°C. The final decomposition temperatures ( $T_{\text{end}}$ ) are similar and are in the range 595–660°C, Figure 6. The DTG curves contain three separate degradation steps. The first decomposition peak is observed in the range of 75–140°C with a maximum of weight loss ( $T_1$ ) at 90–130°C. The second decomposition stage takes place between 180–400°C with  $T_2$  at 200–575°C, and the third is between 490 and 590°C with  $T_3$  at 510–565°C, Table 5. The first decomposition peak could be associated with the loss of moisture, the second with the ester bonds breakdown in the structure of copolymers, while the third one could be attributed to the total degradation of copolymers. The obtained results are similar to our previous studies [23, 24]. Copolymers modified by amines are characterised by insignificantly higher



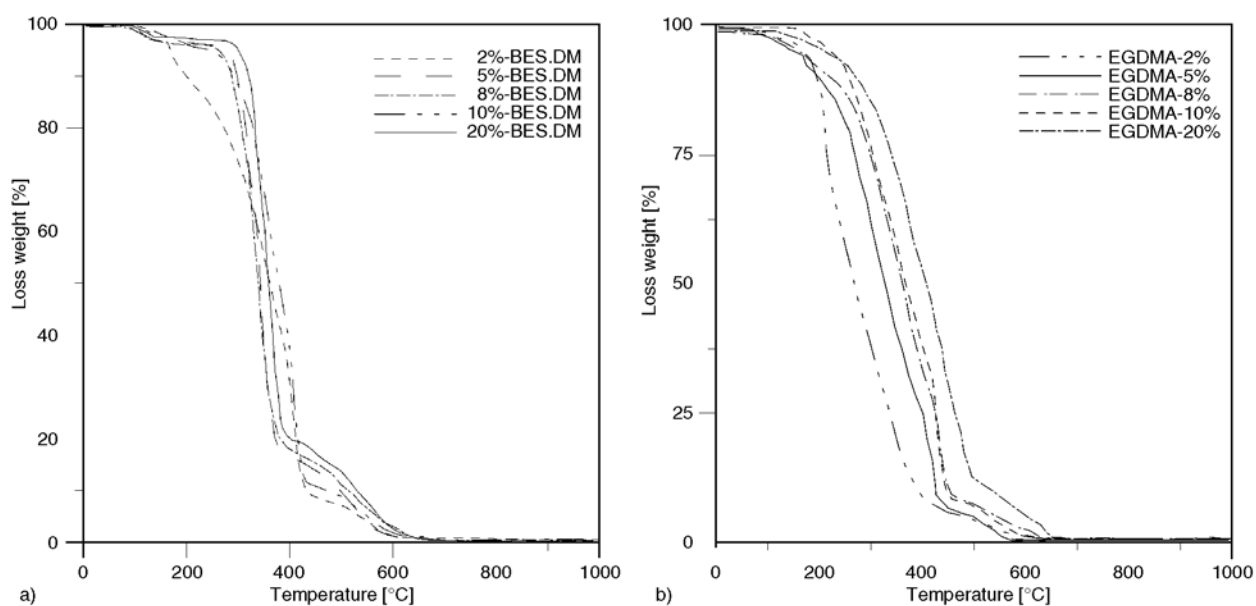


Figure 6. TG curves of the BES.DM-HEMA (a) and EGDMA-HEMA (b)

Table 5. Thermogravimetric analysis BES.DM-HEMA and EGDMA-HEMA

BES.DM:HEMA [% mol]	T <sub>20%</sub>	T <sub>50%</sub>	T <sub>end</sub>	T <sub>1</sub>	T <sub>2</sub>	T <sub>3</sub>
20:80	325	360	650	95	360	545
10:90	325	390	645	105	380	565
8:92	310	360	660	90	335	560
5:95	320	365	640	95	350	560
2:98	265	370	650	92	320	550
EGDMA:HEMA [% mol]						
20:80	260	340	600	130	320	540
10:90	240	350	595	120	290	530
8:92	240	340	600	120	310	535
5:95	220	280	620	90	230	520
2:98	180	250	605	95	200	510
MOD-1	285	360	715	80	340	565
MOD-2	280	370	720	80	350	560

MOD-1 = BES.DM-HEMA-EP-DETA (20% mol)

MOD-2 = BES.DM-HEMA-DETA (20% mol)

temperatures of decomposition. In these cases additional bonds must be broken.

The DSC analysis confirmed these observations. The DSC curves of parent and modified copolymers are presented in Figure 7. Generally, DSC analysis shows similarity in thermal behaviour of all prepared copolymers. However, some differences for modified copolymers can be observed. As shown in Figure 7, copolymers BES.DM-HEMA (2 and 20 % mol) are characterised by one endothermic peak at about 120°C, whereas for EGDMA with HEMA copolymers its maximum is at about 85°C. These endothermic peaks at 83.3–125.4°C are connected with the loss of water present in the struc-

ture of the polymer network. The analysis of the DTA and DSC of modified microbeads show the presence of adsorbed water on the amine groups.

#### 4.4. Adsorption test results

Among sorption materials, the most popular are those containing nitrogen donor atoms which have high adsorption capacity and adsorption selectivity towards transition metal ions. 2-Hydroxyethyl methacrylate hydrogels modified by the compounds containing amino groups such as diethylenetriamine (DETA) can be widely used for the adsorption and separation of metal ions via coordination bond formation or ion exchange at appropriate pH. It is known that the adsorption of the chelating resin towards metal ions must be considered as a liquid–solid phase reaction which includes the diffusion of the ions from the solution to the resin surface, the diffusion of the ions within the solid resin beads, and the coordination reaction between the ions and the amine groups of the resin. The above mentioned factors affect the adsorption process.

In the presented paper the sorption parameters of BES.DM-HEMA-EP-DETA hydrogel were evaluated based on the Langmuir and Freundlich isotherm models. They are the most commonly used to describe the adsorption characteristics of the sorbents. The Langmuir constants  $q_0$  and  $K_L$  are related to the adsorption capacity and the energy of adsorption, respectively. The Freundlich model is applied to non-ideal sorption on heterogeneous surfaces as

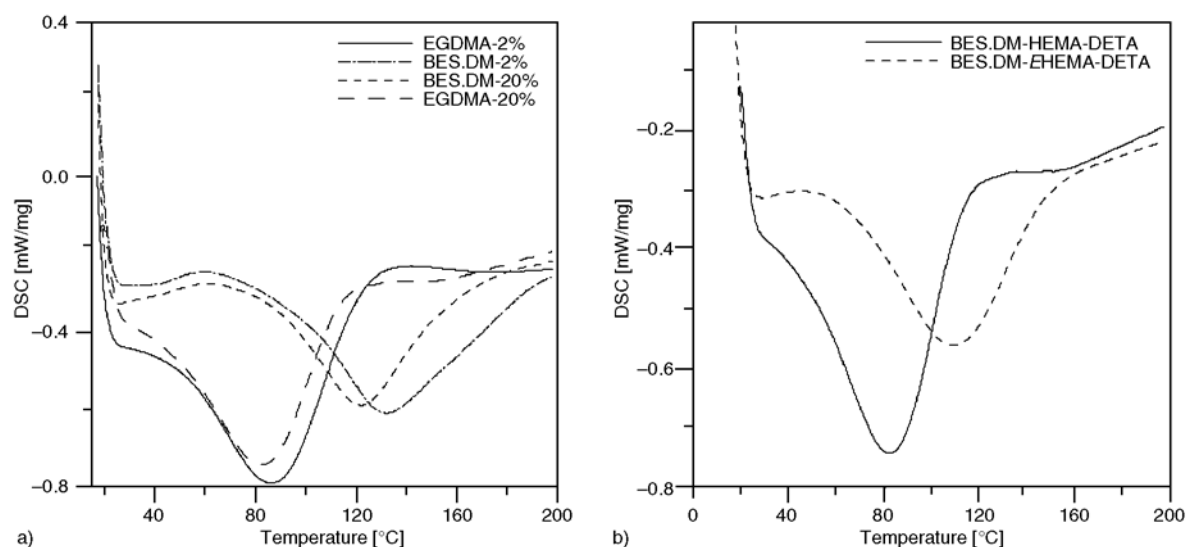


Figure 7. DSC curves, a) parent and b) modified hydrogels

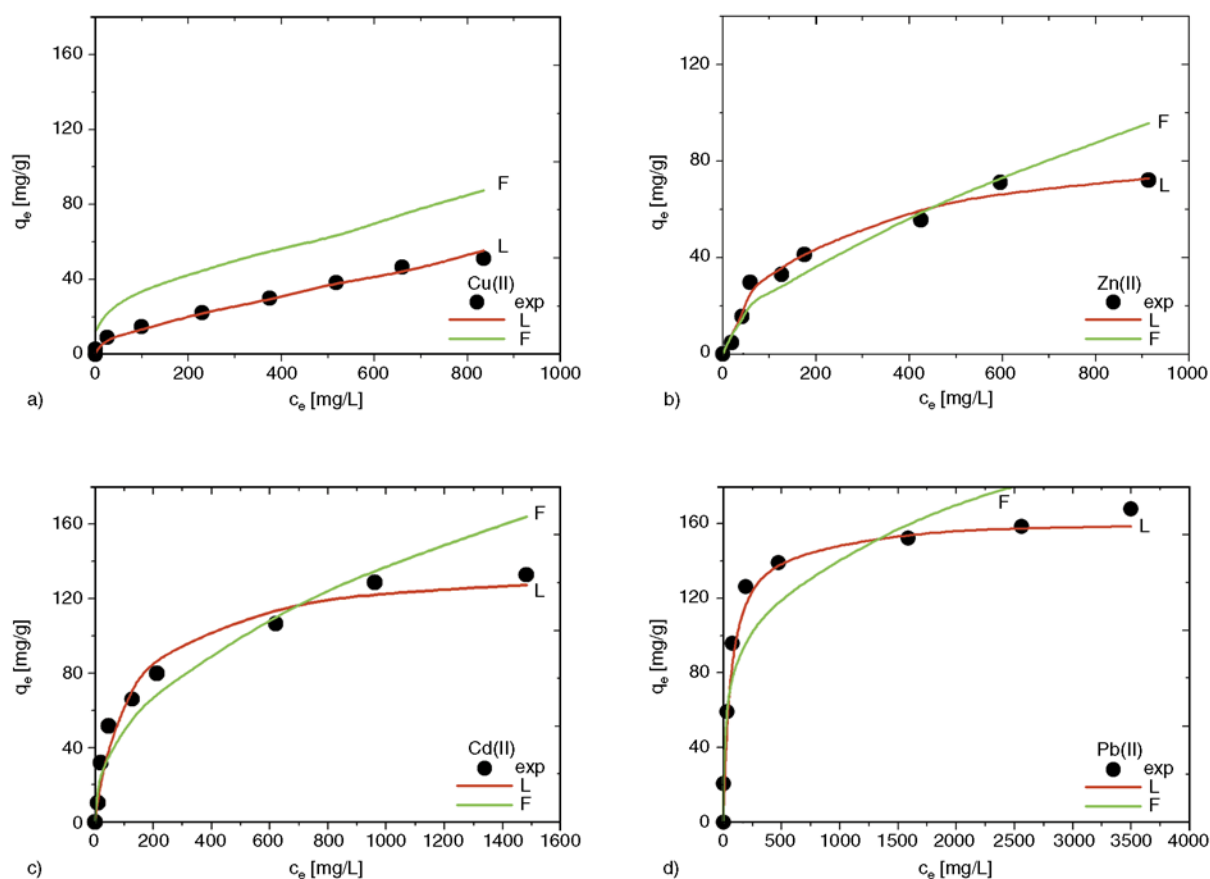


Figure 8. Correlation between the experimental adsorption curve and the calculated data by the Langmuir and Freundlich isotherm models in BES.DM-HEMA-EP-DETA (a) Cu(II), (b) Zn(II), (c) Cd(II) and (d) Pb(II)

well as multilayer adsorption. In this case the higher values of the  $K_F$  indicate a higher affinity for the metal ions in the sorbents used. The values of  $n$  between 1 and 10 indicate favourable adsorption [25]. The Langmuir equation corresponds to a dominant ion exchange mechanism, while the Freund-

lich isotherm shows the adsorption-complexation reactions taking place in the adsorption process [26]. The obtained sorption parameters based on the above-mentioned models are presented in Table 6. Figure 8a–d shows the correlation between the experimental adsorption curve and the calculated

**Table 6.** The Langmuir and Freundlich isotherm constants for Cu(II), Zn(II), Cd(II) and Pb(II) adsorption on BES.DM-HEMA-EP-DETA

System		Cu(II)	Zn(II)	Cd(II)	Pb(II)
	$q_{e,exp}$	<b>45.13</b>	<b>73.08</b>	<b>132.82</b>	<b>168.01</b>
Langmuir	$q_0$	47.01	72.88	136.99	161.29
	$K_L$	0.012	0.05	0.009	0.016
	$R^2$	0.9587	0.9641	0.9826	0.9997
Freundlich	$K_F$	0.89	1.32	6.70	27.98
	$n$	1.22	1.59	2.28	4.19
	$R^2$	0.9231	0.8813	0.8772	0.9467

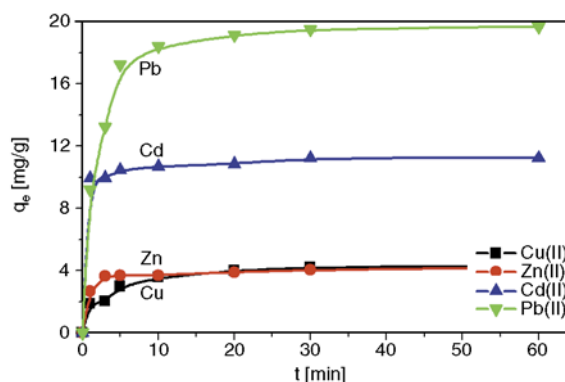
data by the Langmuir and Freundlich isotherm models on BES.DM-HEMA-EP-DETA. The better fitting of the experimental data by the Langmuir model was established based on the  $R^2$  values (Table 6). It was found that for the Langmuir model these values were in the range 0.9587–0.9997, whereas for the Freundlich one they were 0.8772–0.9467.

Based on the Langmuir isotherm model the maximum adsorption capacities ( $q_0$ ) of BES.DM-HEMA-EP-DETA are 0.74 mmol/g for Cu(II), 1.11 mmol/g for Zn(II), 1.23 mmol/g for Cd(II) and 0.78 mmol/g for Pb(II) (Table 6). It should be also mentioned that the calculated values of sorption capacities ( $q_{0,cal}$ ) are comparable with those obtained experimentally ( $q_{e,exp}$ ) and can generally be put in the order: Cd(II) > Zn(II) > Pb(II) > Cu(II). Over the last decades numerous studies regarding metal sorption on hydrogels with different functionalities were published. Among different modifying factors ammonia, ethylenediamine, diethyltriamine have should be mentioned. However, there are few data regarding chelating properties of such obtained materials. In papers by Atia *et al.* [27] as well as Senkal and Bicak [28] the poly(GMA-co-EGDMA) polymers modified among over by diethylenetriamine were used. They found that the sorption capacity for Ca(II) and Mg(II) depends on the type of the ligand and was the highest for DETA. In the case of DETA the concentration of amino groups is higher by 1.15 times compared to those with ethylenediamine (EDA). In

the paper by Maksin *et al.* [29] the porous and non-porous crosslinked poly(glycidyl methacrylate-co-ethylene glycol dimethacrylate) were prepared by suspension copolymerization and functionalized with diethylenetriamine. They found that the maximum adsorption capacity at pH 1.8 was 143 mg/g for PGME2-DETA. The amine derivatives have also been developed by incorporating the mono-amino-, diamino- and triamino- ligands into various families of mesoporous ordered silicas [30].

#### 4.5. Kinetics test results

The effects of the phase contact time on the sorption capacities of BES.DM-EHEMA-DETA towards Cu(II), Zn(II), Cd(II) and Pb(II) ions ( $1.0 \cdot 10^{-3}$  M, shaking speed 180 rpm, temperature 298 K) are presented in Figure 9. Taking into account that the characteristics of adsorption behaviour are generally inferred in terms of both adsorption kinetics and equilibrium isotherms in the next stage the kinetic test were carried out. Predicting the adsorption rate as well as the adsorbate residence time and the reactor dimensions controlled by the kinetic, are probably the most important factors in the adsorption system design. The preliminary results for the BES.DM-HEMA-EP-DETA hydrogel samples were presented to evaluate the sorption kinetics. The calculated kinetic parameters for Cu(II), Zn(II), Cd(II) and Pb(II) in BES.DM-EHEMA-DETA are pre-

**Figure 9.** Effect of the phase contact time on the sorption capacities of BES.DM-EHEMA-DETA towards Cu(II), Zn(II), Cd(II) and Pb(II) ions**Table 7.** The kinetic parameters for Cu(II), Zn(II), Cd(II) and Pb(II) on BES.DM-EHEMA-DETA

M(II)	PF-order model				PS-order model			
	$q_{e,exp}$	$q_1$	$k_1$	$R^2$	$q_2$	$k_2$	$h$	$R^2$
Cu(II)	4.31	1.234	0.023	0.9553	2.34	0.127	2.231	0.9992
Zn(II)	4.20	1.426	0.045	0.9619	4.25	0.200	3.625	0.9993
Cd(II)	10.54	2.488	0.187	0.9582	10.582	0.417	46.729	0.9998
Pb(II)	19.69	7.667	0.171	0.9852	20.450	0.023	9.506	0.9999

sented in Table 7. From these data one can see that the experimental values of sorption capacities ( $q_{e,exp}$ ) are comparable with those obtained by the pseudo second-order model ( $q_2$ ).

## 5. Conclusions

This work includes new, alternative methods of synthesising polymeric microbeads with active groups on the surface that may be useful in ion exchanging process.

New hydrogels were synthesised obtained by suspension polymerisation of 2-hydroxyethyl methacrylate with bis[4(2-hydroxy-3-methacryloyloxypropoxy)phenyl]sulfide or ethylene glycol dimethacrylate. Their hydroxyl functional groups were exploited for introduction of amine groups on the surface using epoxy compounds as intermediates. In preparation of epoxy compounds two procedures were applied.

The swelling and thermal properties of the new hydrogels were studied. Their swelling in water achieved maximum 220%. Similar swelling is observed in methanol whereas in other organic solvents its values were significantly lower. Thermal studies suggest that modification led to an increase of their thermal resistances.

Application of the obtained new hydrogels in sorption of metal ions from water indicate that they are effective sorbents, especially for lead ions.

## References

- [1] Wichterle O., Lim D.: Hydrophilic gels for biological use. *Nature*, **185**, 117–118 (1960).  
DOI: [10.1038/185117a0](https://doi.org/10.1038/185117a0)
- [2] Inoue T., Chen G., Nakamae K., Hoffman A. S.: A hydrophobically-modified bioadhesive polyelectrolyte hydrogel for drug delivery. *Journal of Controlled Release*, **49**, 167–176 (1997).  
DOI: [10.1016/S0168-3659\(97\)00072-2](https://doi.org/10.1016/S0168-3659(97)00072-2)
- [3] Wang J., Wu W.: Swelling behaviors, tensile properties and thermodynamic studies of water sorption of 2-hydroxyethyl methacrylate/epoxy methacrylate copolymeric hydrogels. *European Polymer Journal*, **41**, 1143–1151 (2005).  
DOI: [10.1016/j.eurpolymj.2004.11.034](https://doi.org/10.1016/j.eurpolymj.2004.11.034)
- [4] Qiu Y., Park K.: Environment-sensitive hydrogels for drug delivery. *Advanced Drug Delivery Reviews*, **53**, 321–339 (2001).  
DOI: [10.1016/S0169-409X\(01\)00203-4](https://doi.org/10.1016/S0169-409X(01)00203-4)
- [5] Lin G., Chang S., Kuo C-H., Magda J., Solzbacher F.: Free swelling and confined smart hydrogels for applications in chemomechanical sensors for physiological monitoring. *Sensors and Actuators B: Chemical*, **136**, 186–195 (2009).  
DOI: [10.1016/j.snb.2008.11.001](https://doi.org/10.1016/j.snb.2008.11.001)
- [6] Liu F., Urban M. W.: Recent advances and challenges in designing stimuli-responsive polymers. *Progress in Polymer Science*, **35**, 3–23 (2010).  
DOI: [10.1016/j.progpolymsci.2009.10.002](https://doi.org/10.1016/j.progpolymsci.2009.10.002)
- [7] Gupta P., Vermani K., Garg S.: Hydrogels: From controlled release to pH-responsive drug delivery. *Drug Discovery Today*, **7**, 569–579 (2002).  
DOI: [10.1016/S1359-6446\(02\)02255-9](https://doi.org/10.1016/S1359-6446(02)02255-9)
- [8] Tomić S. L., Mičić M. M., Dobić S. N., Filipović J. M., Suljovrujić E. H.: Smart poly(2-hydroxyethyl methacrylate/itaconic acid) hydrogels for biomedical application. *Radiation Physics and Chemistry*, **79**, 643–649 (2010).  
DOI: [10.1016/j.radphyschem.2009.11.015](https://doi.org/10.1016/j.radphyschem.2009.11.015)
- [9] Chang C., Duan B., Cai J., Zhang L.: Superabsorbent hydrogels based on cellulose for smart swelling and controllable delivery. *European Polymer Journal*, **46**, 92–100 (2010).  
DOI: [10.1016/j.eurpolymj.2009.04.033](https://doi.org/10.1016/j.eurpolymj.2009.04.033)
- [10] Hejčl A., Lesný P., Přádný M., Šedý J., Zámečník J., Jendelová P., Michálek J., Syková E.: Macroporous hydrogels based on 2-hydroxyethyl methacrylate. Part 6: 3D hydrogels with positive and negative surface charges and polyelectrolyte complexes in spinal cord injury repair. *Journal of Materials Science: Materials in Medicine*, **20**, 1571–1577 (2009).  
DOI: [10.1007/s10856-009-3714-4](https://doi.org/10.1007/s10856-009-3714-4)
- [11] Chauhan G. S., Chauhan S., Sen U., Garg D.: Synthesis and characterization of acrylamide and 2-hydroxyethyl methacrylate hydrogels for use in metal ion uptake studies. *Desalination*, **243**, 95–108 (2009).  
DOI: [10.1016/j.desal.2008.04.017](https://doi.org/10.1016/j.desal.2008.04.017)
- [12] Chirila T. V.: An overview of the development of artificial corneas with porous skirts and the use of PHEMA for such an application. *Biomaterials*, **22**, 3311–3317 (2001).  
DOI: [10.1016/S0142-9612\(01\)00168-5](https://doi.org/10.1016/S0142-9612(01)00168-5)
- [13] Chirila T. V., Hicks C. R., Dalton P. D., Vijayasekaran S., Lou X., Hong Y., Clayton A. B., Ziegelaar B. W., Fitton J. H., Platten S., Crawford G. J., Constable I. J.: Artificial cornea. *Progress in Polymer Science*, **23**, 447–473 (1998).
- [14] Kultys A.: Sulfur-containing polymers. in ‘Encyclopedia of polymer science and technology’ (eds.: Mark H. F.) Wiley, New York (2010).  
DOI: [10.1002/0471440264.pst355.pub2](https://doi.org/10.1002/0471440264.pst355.pub2)

- [15] Podkościelna B., Bartnicki A., Gawdzik B.: Porous microspheres, copolymers of bis[4-(2-hydroxy-3-methacryloyloxypropoxy)phenyl]sulfide, and divinylbenzene as stationary phase for HPLC. *Journal of Applied Polymer Science*, **111**, 1257–1267 (2009). DOI: [10.1002/app.29154](https://doi.org/10.1002/app.29154)
- [16] Podkościelna B.: Synthesis, modification, and porous properties of new glycidyl methacrylate copolymers. *Journal of Applied Polymer Science*, **120**, 3020–3026 (2011). DOI: [10.1002/app.33420](https://doi.org/10.1002/app.33420)
- [17] PN-C-89085:1974: Uncured epoxy resins. Methods of testing (in Polish) (1974).
- [18] Tuncel A., Pişkin A.: Nonswellable and swellable poly(EGDMA) microspheres. *Journal of Applied Polymer Science*, **62**, 789–798 (1996). DOI: [10.1002/\(SICI\)1097-4628\(19961031\)62:5<789::AID-APP11>3.0.CO;2-O](https://doi.org/10.1002/(SICI)1097-4628(19961031)62:5<789::AID-APP11>3.0.CO;2-O)
- [19] Kesenci K., Tuncel A., Pişkin E.: Swellable ethylene glycol dimethacrylate-hydroxyethylmethacrylate copolymer beads. *Reactive and Functional Polymers*, **31**, 137–147 (1996). DOI: [10.1016/1381-5148\(96\)00052-1](https://doi.org/10.1016/1381-5148(96)00052-1)
- [20] Langmuir I.: The constitution and fundamental properties of solids and liquids. Part I. Solids. *Journal of the American Chemical Society*, **38**, 2221–2295 (1916). DOI: [10.1021/ja02268a002](https://doi.org/10.1021/ja02268a002)
- [21] Freundlich H. F. M.: Über die Adsorption in Lösungen. *Zeitschrift für Physikalische Chemie*, **57**, 385–470 (1906).
- [22] Ketcha Mbadcam J., Anagho S. G., Ndi Nsami J., Kammege A. M.: Kinetic and equilibrium studies of the adsorption of lead (II) ions from aqueous solution onto two Cameroon clays: Kaolinite and smectite. *Journal of Environmental Chemistry and Ecotoxicology*, **3**, 290–297 (2011).
- [23] Podkościelna B., Worzakowska M.: Synthesis, characterization, and thermal properties of diacrylic/divinylbenzene copolymers. *Journal of Thermal Analysis and Calorimetry* **101**, 235–241 (2010). DOI: [10.1007/s10973-009-0574-6](https://doi.org/10.1007/s10973-009-0574-6)
- [24] Podkościelna B.: The highly crosslinked dimethacrylic/divinylbenzene copolymers. Characterization and thermal studies. *Journal of Thermal Analysis and Calorimetry*, **104**, 725–730 (2011). DOI: [10.1007/s10973-010-1184-z](https://doi.org/10.1007/s10973-010-1184-z)
- [25] Podkościelna B.: The use of bis[4(2-hydroxy-3-methacryloyloxypropoxy)phenyl]sulfide in preparation of microspheres with pendant amine groups as a heavy metal sorbent. *Separation Science and Technology*, in press (2012).
- [26] Yang C-H.: Statistical mechanical study on the Freundlich isotherm equation. *Journal of Colloid and Interface Science*, **208**, 379–387 (1998). DOI: [10.1006/jcis.1998.5843](https://doi.org/10.1006/jcis.1998.5843)
- [27] Atia A. A., Donia A. M., Abou-El-Enein S. A., Yousif A. M.: Studies on uptake behaviour of copper(II) and lead(II) by amine chelating resins with different textural properties. *Separation and Purification Technology*, **33**, 295–301 (2003). DOI: [10.1016/S1383-5866\(03\)00089-3](https://doi.org/10.1016/S1383-5866(03)00089-3)
- [28] Şenkal B. F., Biçak N.: Glycidyl methacrylate based polymer resins with diethylene triamine tetra acetic acid functions for efficient removal of Ca(II) and Mg(II). *Reactive and Functional Polymers*, **49**, 151–157 (2001). DOI: [10.1016/S1381-5148\(01\)00075-X](https://doi.org/10.1016/S1381-5148(01)00075-X)
- [29] Maksin D. D., Nastasović A. B., Milutinović-Nikolić A. D., Suručić L. T., Sandić Z. P., Hercigonja R. V., Onjia A. E.: Equilibrium and kinetics study on hexavalent chromium adsorption onto diethylene triamine grafted glycidyl methacrylate based copolymers. *Journal of Hazardous Materials*, **209–210**, 99–110 (2012). DOI: [10.1016/j.jhazmat.2011.12.079](https://doi.org/10.1016/j.jhazmat.2011.12.079)
- [30] Aguado J., Arsuaga J. M., Arencibia A., Lindo M., Gascón V.: Aqueous heavy metals removal by adsorption on amine-functionalized mesoporous silica. *Journal of Hazardous Materials*, **163**, 213–221 (2011). DOI: [10.1016/j.jhazmat.2008.06.080](https://doi.org/10.1016/j.jhazmat.2008.06.080)